Ultrafast dynamics at aqueous-air interfaces

JORDAN, CALEB,JAMES,CHARLES

Ultrafast Dynamics at Aqueous-Air Interfaces

Caleb J. C. Jordan

2023

Department of Chemistry

University of Durham

Submitted for the Qualification of Doctor of Philosophy

Declaration

The research described within this thesis was conducted by the author unless indicated otherwise. The material presented herein has not been previously submitted for a degree at the University of Durham or another institution.

Copyright Notice

Contents

Ultrafast Dynamics at Aqueous-Air Interfaces

Caleb J. C. Jordan

Abstract

A femtosecond time-resolved surface electronic sum-frequency generation spectroscopy setup has been constructed in conjunction with a femtosecond transient absorption setup. The layouts are described, along with the principles of their use. In the case of the surface experiment, a novel combination of existing techniques has enabled nonlinear spectroscopic measurements to be performed on fluorescent samples by optical Kerr gating of the surface nonlinear response. The sum-frequency generation and transient absorption setups were used together to investigate the hydrated electron formed by photo-oxidation of the phenolate anion at the aqueous/air interface and in solution. The hydrated electron is important across a breadth of chemistry, and is relevant to areas such as atmospheric, nuclear, and biological chemistry, where it is considered an important species in reductive DNA damage. The surface electron was observed to exhibit similar dynamics to the same bulk system, albeit at an accelerated rate. The study was improved by observing dynamics across a range of wavelengths, which showed a variation in dynamics across the spectral regions probed. The variations in dynamics were attributed to a second species at the interface: the phenoxyl radical. Kinetics and associated spectra of both species were retrieved from the data, exhibiting the first optical spectrum of the hydrated electron at the aqueous/air interface. Finally, potential chemical systems and experimental developments of interest are presented.

Acknowledgements

This thesis is the culmination of several years of undergraduate and postgraduate study at Durham University, and has been supported directly and indirectly by far too many people to name individually. Please know that I am grateful to all of you, however big or small your contributions.

Thank you, Jan. Your enthusiasm for science is infectious, and I hope there are more supervisors that share your perspective. I hope you never took my debatably pessimistic approach to lab work too seriously (though I say more like realistic). It has been an absolute pleasure working with you, and I look forward to seeing the science you produce in the future. I truly couldn't have asked for a better supervisor.

Thank you to the whole Verlet Group, both past and present, during my time working with you all. I will miss the office and pub conversations greatly, whether they were academic in nature or not. You were always there to share in the triumphs and the grievances, and never made the years feel like hard work.

Thank you also to those who supported this work more directly. Undergraduate students, summer internship students, academics, technical staff and funding bodies, from Durham and beyond. You all provided significant contributions which I appreciate immensely. Without them, this work would be that much lesser, or not at all.

More personally, thank you to all the friends and my family who supported me and this work, even if you didn't realise. To all those who asked why I care about lasers and electrons, or were just there to talk, to play or to laugh with: you all helped. Thank you to my parents, for supporting me unconditionally.

Abbreviations

BBO	β-barium borate
CTTS	Charge-transfer-to-solvent
DAS	Difference absorption spectrum
DCM	2-methyl-6-(4-dimethylaminostyryl)-4H-pyran
EM	Electromagnetic
ESFG	Electronic sum-frequency generation
FWHM	Full width at half maximum
GGG	Gadolinium gallium garnet
IRF	Instrument response function
KM	Kerr medium
LO	Local oscillator
MG	Malachite green
OD	Optical density
OKG	Optical Kerr gating
OPA	Optical parametric amplifier
PC	Pockels cell
PMT	Photomultiplier tube
POI	Plane of incidence
PSU	Phase-shifting unit
SFG	Sum-frequency generation
SHG	Second-harmonic generation
TA	Transient absorption
TDM	Transition dipole moment
TR-OKG-ESFG	Time-resolved, optically Kerr gated electronic sum-frequency generation
TR-SFG	Time-resolved sum-frequency generation
VSFG	Vibrational sum-frequency generation
WL	White light

Publications

1. Jordan, C. J. C. & Verlet, J. R. R. Time-resolved electronic sum-frequency generation spectroscopy with fluorescence suppression using optical Kerr gating. *J. Chem. Phys.* **155**, 164202 (2021).

2. Lietard, A., Screen, M. A., Flindt, D. L., Jordan, C. J. C., Robson, J. M. & Verlet, J. R. R. A Combined Spectrophotometer and Fluorometer to Demonstrate the Principles of Absorption Spectroscopy. *J. Chem. Educ.* **98**, 3871–3877 (2021).

3. Guillén-García, A., Gibson, S. E. R., Jordan, C. J. C., Ramaswamy, V. K., Linthwaite, V. L., Bromley, E. H. C., Brown, A. P., Hodgson, D. R. W., Blower, T. R., Verlet, J. R. R., Degiacomi, M. T., Pålsson, L. O. & Cann, M. J. Allophycocyanin A is a carbon dioxide receptor in the cyanobacterial phycobilisome. *Nat. Commun.* **13**, 1–10 (2022).

4. Jordan, C. J. C., Lowe, E. A. & Verlet J. R. R., Photooxidation of the Phenolate Anion is Accelerated at the Water/Air Interface. *J. Am. Chem. Soc.* **144**, 14012–14015 (2022).

Introduction and Thesis Outline

Interfaces are all around us and are a defining feature of condensed phases. Wherever a condensed phase is in physical contact with any other phase, interfacial processes are at play. Most photochemistry has been studied in bulk solution or gas phases, whereas ultrafast interfacial processes are much less studied on account of the difficulty in studying such environments selectively. Hence, the work presented here aims to better understand ultrafast interfacial processes from a chemical perspective. Interfacial science is a broad area however, with several distinct characters of interfacial environment: solid/solid, solid/gas, solid/liquid, liquid/liquid, and liquid/gas. Here, the focus is on the liquid/air, or specifically the aqueous/air, interface (i.e. the upper surface of an aqueous solution in contact with the atmosphere). This area is of particular importance for atmospheric chemistry, where a broad range of processes in our natural environment take place on aerosols or open water, which covers the majority of our planet. Understanding processes at the aqueous/air interface is of practical significance for climate modelling and the chemistry of synthetic and organic materials that permeate our environment. In particular, light-driven processes at aqueous interfaces are an underexplored area that this thesis aims to contribute to by asking basic questions such as: how do photodynamics or the kinetics of photoproducts change at the aqueous/air interface?

This thesis discusses theory and experiments on ultrafast dynamics at aqueous/air interfaces via optical spectroscopic methods. Chapter 1 discusses spectroscopic principles with a view to their use in ultrafast time-resolved techniques, in particular focussing on transient absorption spectroscopy. Such techniques can provide detailed descriptions of photodynamics in bulk aqueous environments, forming an important basis for describing interfacial dynamics, which may be more difficult to interpret. Similarly, Chapter 2 follows by discussing the theory surrounding surface sum-frequency generation spectroscopy and current progress of its various techniques. The field of surface sum-frequency generation spectroscopy has become dominated by vibrationally-resonant techniques, however the focus here is instead on electronically-resonant techniques.

Chapter 3 presents the experimental setups built or adapted over the course of this PhD programme, including both transient absorption and surface sum-frequency generation spectroscopy setups.

Chapter 4 presents results of time-resolved surface sum-frequency generation spectroscopy experiments conducted on the chemical malachite green, which served to test the incorporation of optical Kerr gating into the experimental setup. Also presented are some experiments designed to probe the application of surface electronic sum-frequency generation and what information can be obtained via its use.

Chapter 5 presents experimental work using the optically-Kerr-gated surface sum-frequency generation setup that was developed to study photooxidation of the phenolate anion at the air/water interface. In particular, dynamics of the interfacial hydrated electron are monitored. This is expanded on in Chapter 6, which probes the same system over a wide spectral range to build a more complete picture of the interfacial photochemistry.

Finally, Chapter 7 concludes by discussing potential chemical systems for future studies and potential future modifications for the experimental setup developed here.

1. Time-Resolved Spectroscopy

Light-driven chemical processes are fundamental to our world. Photosynthesis and the early events in vision are important examples of photophysics that drives research of these ultrafast mechanisms. As well as natural systems, synthetic chemistry has made use of light-activated reactions to improve synthetic efficiencies or access products that were unobtainable through conventional procedures. Understanding these processes requires interrogating the photochemistry on an ultrafast timescale when critical steps take place, which is especially true for interfacial photochemistry where rates can be accelerated by orders of magnitude.[1–3] Ultrafast studies are much better developed for the bulk phases, especially in solution, which are crucial in understanding the more complex interfacial environments. Transient absorption (TA) spectroscopy has become a cornerstone technique to study ultrafast processes in solution on account of its time resolution and spectral range, and has been used extensively to monitor the effect of solvent environments on chemical dynamics. Consequently, it has become a key technique to support surface studies where the partial solvation at an interface can strongly affect the ultrafast photodynamics that take place.

1.1. Optical Spectroscopy

At its core, spectroscopy concerns the interaction of electromagnetic radiation and matter, though the frequency, or energy, of the radiation can be wide-ranging. For example, ultraviolet light and microwave light each access vastly different information about a chemical system. The electronic transitions of chemical species typically occur in the UV-visible region of the electromagnetic (EM) spectrum, at frequencies of around ~10^{15} Hz (~100-1000 nm), at the approximate timescale on which electron densities oscillate in chemical processes.[4] Accessing information about the electronic structure of a system is of foremost importance to the fundamental processes that underpin much of chemistry, especially in charge transfer reactions.

1.1.1. Light-Matter Interactions

When light and matter interact, a number of processes can occur depending on the properties of the material and the radiation. While a travelling EM wave consists of perpendicular electric and magnetic components, it is the electric field component of the wave, $\vec{E}(\vec{r},t)$, which primarily causes a response within an atom or molecule:

$$\vec{E}(\vec{r},t) = \vec{\mathcal{E}}\cos\left(\vec{k}\cdot\vec{r} - \omega t\right) = \frac{1}{2}\vec{\mathcal{E}}\left[\exp(i\vec{k}\cdot\vec{r} - i\omega t) + \exp(-i\vec{k}\cdot\vec{r} + i\omega t)\right], \tag{1.1}$$

where $\vec{\mathcal{E}}$ is the magnitude of the electric field, ω is the frequency of the wave and $\vec{k}$ is its wavevector, at some position, $\vec{r}$, and time, t. The electric field oscillates in time, and so will induce oscillations in the molecular charge distributions in the material it propagates through.[5] The molecules' charge distribution will oscillate, resulting in oscillating dipoles within the medium. In the case where the energy of an EM photon, $\hbar\omega$, is far detuned from any resonance in the material, or selection rules prevent a transition, the photon will interact non-resonantly. In this case, a photon is absorbed and instantaneously re-emitted without an overall change in the molecule's quantum states. The system remains unchanged except for the direction of the photon propagation, which is scattered based on the polarisation of the incoming light. The direction of scattering and the interaction of the scattered photons with the incident field gives rise to transmission, reflection, refraction and diffraction within materials.

Alternatively, when $\hbar\omega$ is close to the energy difference between a lower and a higher energy state of an atom or molecule, the oscillations in electron density may couple the two states, inducing a transition. The photon is absorbed, and its energy is imparted to the absorbing molecule where it may be distributed amongst its rotational, vibrational and electronic energies.

1.1.1.1. Transition Probabilities

Not all situations where a photon's energy matches an energy gap between two states will cause a transition. The probability of a particular transition is governed by its transition dipole moment (TDM), which is a measure of the rearrangement of electron density associated with that transition, and is affected by factors such as the spatial overlap of the orbitals of the states involved.[6] The probability of a transition from state $f \leftarrow i$ is proportional to the square of the TDM integral, $\vec{M}_{fi}$:

$$\vec{M}_{fi} = \langle \psi' | \hat{\mu} | \psi'' \rangle \,, \tag{1.2}$$

where $\hat{\mu}$ is the electric dipole moment operator in the direction of the electric field of the incoming wave, and ψ' and ψ'' are the full wavefunctions of the final and initial states, respectively. The probability of a measured transition is proportional to $\left|\vec{M}_{\mathrm{fi}}\right|^2$.[7]

The vibronic wavefunction, ψ_{ev}, of a state describes both the electronic and vibrational wavefunctions, which are inherently coupled. The Born-Oppenheimer approximation postulates that the motions of electrons are much faster than those of nuclei, which are comparatively much more massive. Thus, the nuclei under this approximation are treated as stationary with respect to the electrons.[6] As a result, a vibronic wavefunction becomes separable, and can be expressed in the form

$$\psi_{\mathrm{ev}} = \psi_{\mathrm{e}} \psi_{\mathrm{v}} \,, \tag{1.3}$$

where ψ_{e} and ψ_{v} are the electronic and vibrational wavefunctions, respectively. Thus, (1.2) can be expanded as

$$\vec{M}_{fi} = \left\langle \psi'_{\mathrm{e}} \middle| \hat{\mu}_{\mathrm{e}} \middle| \psi''_{\mathrm{e}} \right\rangle \left\langle \psi'_{\mathrm{v}} \middle| \psi''_{\mathrm{v}} \right\rangle + \left\langle \psi'_{\mathrm{e}} \middle| \psi''_{\mathrm{e}} \right\rangle \left\langle \psi'_{\mathrm{v}} \middle| \hat{\mu}_{\mathrm{v}} \middle| \psi''_{\mathrm{v}} \right\rangle \,, \tag{1.4}$$

where $\hat{\mu}$ has been separated into its electronic and nuclear terms, $\hat{\mu}_{\mathrm{e}}$ and $\hat{\mu}_{\mathrm{v}}$, respectively. In (1.4), the second term on the right-hand side vanishes on account of the fact electronic states are orthogonal to one another. Hence (1.4) is simplified:

$$\vec{M}_{fi} = \vec{R}_{fi} \langle v' | v'' \rangle \,, \tag{1.5}$$

where $\vec{R}_{fi} = \left\langle \psi'_{\mathrm{e}} \middle| \hat{\mu}_{\mathrm{e}} \middle| \psi''_{\mathrm{e}} \right\rangle$ and $\langle v' | v'' \rangle = \left\langle \psi'_{\mathrm{v}} \middle| \psi''_{\mathrm{v}} \right\rangle$. $\vec{R}_{fi}$ is the electronic transition moment between the final and initial electronic states of *f* and *i*, whereas $\langle v' | v'' \rangle$ is the vibrational overlap between the initial vibrational state on *i*, *v*'', and the final vibrational state on *f*, *v*'. Since the probability of a transition is dependent on $\left|\vec{M}_{fi}\right|^2$, it is also proportional to $\left|\vec{R}_{fi}\right|^2$, which is a measure of the intrinsic strength of the transition and whether it is allowed by selection rules. The probability also depends on $|\langle v' | v'' \rangle|^2$, termed the Franck-Condon factor, which is greatest for transitions between vibrationally-similar states.[6] This refers to states that have the greatest orbital overlap over a fixed nuclear coordinate, since the electronic excitation will occur much faster than the time needed for the nuclei to adjust to the changing electron distribution.

1.1.1.2. Oscillator Strength

The intensity or strength of a transition can be measured through its oscillator strength, f_{fi},[6,8]

$$f_{fi} = \frac{8\pi^2 m_e \nu}{3he^2} \left| M_{fi} \right|^2 , \tag{1.6}$$

where ν is the frequency of the transition $f \leftarrow i$. The oscillator strength of a transition can be determined experimentally from an absorption spectrum, using

$$f_{fi} = \frac{4m_e c\varepsilon_0}{N_A e^2} \mathcal{A} , \tag{1.7}$$

where $\mathcal{A}$ is the integrated absorption coefficient for the transition,[8]

$$\mathcal{A} = \int \varepsilon(\nu) \mathrm{d}\nu , \tag{1.8}$$

where $\varepsilon(\nu)$ is the molar extinction coefficient. In practice, the oscillator strength is a ratio of the transition intensity to that of an electron oscillating harmonically in three dimensions.

1.1.2. Excited States

After undergoing a transition, a molecule may find itself in an excited state higher in energy than its ground state. Excited states are unstable and will decay after a characteristic time. Transitions between states are termed radiative or nonradiative processes, depending on whether they are mediated by absorption or emission of photons or not, respectively. Such processes are concisely depicted using a Jabłoński diagram, which represents different transition pathways between various states of a molecular system (Figure 1.1). Absorption involves incident photons transferring their energy to a molecule to promote it to a higher state. Emission involves a molecule losing energy in the form of a photon to return to a lower-lying state, which is also radiative. Emission is either spontaneous or stimulated, the former of which refers to probabilistic emission of a photon after some natural lifetime, and the latter of which refers to emission as a result of interaction with an external electric field, such as another photon.

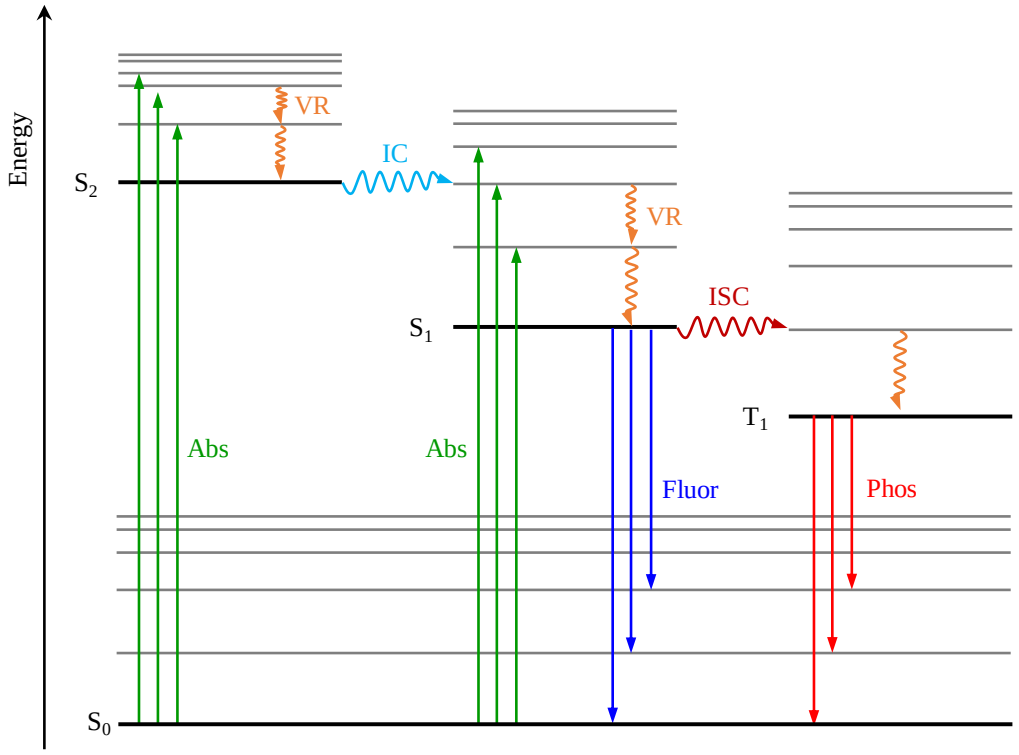

Figure 1.1: Simple Jabłoński diagram showing spectroscopic transitions in a molecule between electronic singlet states (S_0-S_2) and a triplet state (T_1). Radiative transitions are represented as straight arrows and nonradiative transitions as curved arrows. Abs = absorption, Fluor = fluorescence, Phos = phosphorescence, VR = vibrational relaxation, IC = internal conversion, ISC = intersystem crossing. Black energy levels represent electronic states, and grey represent vibrational states.

The rate of spontaneous emission from an excited state, *f* to a lower state, *i* is given by the Einstein coefficient A_{if}:[9]

$$A_{if} = \frac{8\pi^2 \nu^3}{3\varepsilon_0 \hbar c^3} \left| M_{fi} \right|^2 , \tag{1.9}$$

where ν is the frequency of the emitted photon whose energy corresponds to the difference between *f* and *i*. Like absorption, the rate of spontaneous emission is proportional to the square of the TDM between the states, but also to ν^3, so that transitions between states with a large energy difference are generally fast compared to those of similar energies. The natural lifetime of a state, τ, is intrinsically related to the rate by $\tau = A_{if}^{-1}$.

Stimulated emission may be exhibited by a molecule in an excited state interacting with a photon whose energy corresponds to the energy gap between that state and a lower state. The induced oscillations in electron density cause emission of a coherent photon at the same frequency and phase as the incident light.

The rate of stimulated emission from a state *f* to a state *i*, B_{if}, is

$$B_{if} = \frac{\pi}{3\varepsilon_0 \hbar^2} \left| M_{fi} \right|^2 , \tag{1.10}$$

which is independent of frequency.

Emission from excited states takes the form of either fluorescence or phosphorescence, which is governed by the spin multiplicity of the initial and final states. Between states of the same spin multiplicity, the emission is termed fluorescence and is spin-allowed. Alternatively, if the spin multiplicities of the states differ the emission is termed phosphorescence, which is spin-forbidden. As a result, phosphorescent emission typically has lower probabilities and longer lifetimes than fluorescent emission.[7]

Excited species also relax via nonradiative processes such as vibrational relaxation, internal conversion, or intersystem crossing. Vibrational relaxation reduces the vibrational energy of a molecule whilst remaining in the same electronic state. In the gas phase the vibrational energy is redistributed internally amongst other vibrational modes as the excited molecule thermalises to a Boltzmann distribution of its vibrational modes. In the condensed phase, this can additionally take the form of a vibrationally excited species transferring energy to surrounding molecules via collisions and frictional forces. After an electronic transition a molecule may be highly vibrationally excited according to the Franck-Condon principle,[6] and vibrational relaxation is a key process in thermalising the energy of the final state.

Internal conversion and intersystem crossing are nonradiative transitions between different electronic states with the same or different spin multiplicities, respectively. As with phosphorescence, intersystem crossing is spin-forbidden, but is possible when spin selection rules are relaxed by spin-orbit coupling.[7] Either process typically involves a low vibrational state of an excited electronic state decaying to an excited vibrational state of a lower electronic energy state, which is followed by vibrational relaxation. This is a breakdown of the Born-Oppenheimer approximation, where it appears that nuclear and electronic energies are exchanged.[10] Mechanisms of internal conversion and intersystem crossing usually take the form of motion around nuclear coordinates to reach conical intersections of potential energy surfaces - molecular geometries where electronic states become degenerate – or points where the electronic and nuclear wavefunctions can become strongly coupled to facilitate a transition. An excited molecule may thus have many routes to return to its ground state, where the above radiative and nonradiative processes compete simultaneously.

1.1.3. Absorbance Spectroscopy

At its most basic level, spectroscopy measures a substance's characteristic ability to absorb wavelengths of light. Experimentally this is simple, requiring only a light source, sample and detector. The absorbance of a molecule is a result of those mechanisms described above, where the number of absorbing molecules in the path of the light source must also be considered. The transmitted intensity of the light through an absorbing sample is famously given in the limit of low concentration by the Beer-Lambert law:[6,11]

$$I(\lambda) = I_0(\lambda)10^{-\varepsilon(\lambda)cl} , \tag{1.11}$$

where $I(\lambda)$ is the transmitted intensity, $I_0(\lambda)$ is the initial intensity before interacting with the sample, $\varepsilon(\lambda)$ is the molar extinction coefficient, c is the sample concentration and l is the path length through the sample. Although only quantitatively valid for dilute solutions ($<10^{-2}$ M), the excitation pulses used to generate species of interest in transient absorption spectroscopy usually excite only a small population of the sample. The absorbance of a sample, $A(\lambda)$ is

$$A(\lambda) = -\log\left(\frac{I(\lambda)}{I_0(\lambda)}\right) = \varepsilon(\lambda)cl . \tag{1.12}$$

The product $\varepsilon(\lambda)cl$ is referred to as the optical density (OD) of a sample.

1.2. Transient Absorption Spectroscopy

Steady-state techniques are limited in their utility when excited states and short-lived intermediate species are concerned. In order to properly characterise these transients, there must exist a time resolution in spectroscopic methods that probe them. TA spectroscopy builds upon absorption spectroscopy by additionally measuring the absorbance of a system as a function of time, $A(\lambda,t)$. This way, transient species generated by some perturbation event, such as a pulsed laser excitation, can be observed as the system decays back to an equilibrium. Modern TA techniques almost exclusively utilise laser systems in order to provide sufficiently short excitation pulses, down to femtosecond or attosecond resolution.[12–15]

1.2.1. Pump-Probe Spectroscopy

Pump-probe spectroscopy encompasses a broad array of experimental techniques that operate on the same core principles. Such transient techniques involve perturbing a system away from equilibrium at a well-defined time, then observing either the return to its original equilibrium or a new pathway along some reactive coordinate. Modern pump-probe spectroscopy regularly employs two spatially-overlapping laser pulses when conducting measurements: a 'pump' pulse, a temporally narrow high-intensity pulse to excite the sample of interest, and a 'probe' pulse, a second narrow-time pulse to extract information from the excited sample.[16] Absorption measurements follow the same premises as above, though now the absorbing species is an excited state or photoproduct of the initial sample.

As the species generated by the pump will usually have some finite lifetime, the time at which the probe arrives is pivotal to extracting insightful information on the photochemistry of a sample. This relative time frame is labelled with respect to the point at which the two pulses coincide in time, referred to as t_0. If the probe arrives at the sample some time, t, after t_0, the absorbance measurements include those of the excited sample that has been allowed to evolve for some time t. Alternatively, at negative time, $t < t_0$, the probe arrives before the pump, effectively performing absorbance measurements on the unexcited sample. For measurements that aim to visualise dynamics on a sub-picosecond timescale, t is often varied through a delay stage, which uses a variable path length as an equivalent time delay by causing one pulse to arrive before or after the other based on its distance travelled.

1.2.2. Difference Absorption Spectra

A pump excitation may only excite a small population of a sample, so a standard absorption spectrum would still be dominated by the features of the unpumped species. To better view the small changes induced, a difference absorption spectrum (DAS) is commonly employed, whereby the change in OD, $\Delta OD(\lambda, t)$, is the direct subtraction of the unpumped signal from the excited sample at t:

$$\Delta OD(\lambda, t) = -\log\left(\frac{I_{\text{pump-probe}}(\lambda, t)}{I_{\text{pump-off}}(\lambda, t)}\right), \tag{1.13}$$

where $I_{\text{pump-probe}}(\lambda, t)$ is the pump-probe signal and $I_{\text{pump-off}}(\lambda, t)$ is the unpumped signal. The time-dependent nature of the $\Delta OD(\lambda, t)$ therefore provides information on the dynamics of any processes occurring within a sample that will be identifiable in an absorption spectrum.

Unlike a traditional absorbance spectrum, a DAS may have both positive and negative ΔOD features which may overlap to make interpretation difficult (Figure 1.2). The absorption of photoproducts appears as a positive peak due to their increased density in the pumped sample, which may arise from excited states of the system or from new chemical species generated from photodissociation or reaction between excited species (Figure 1.3(a)). Negative peaks indicate the presence of a ground state bleach, whereby the probe shows reduced lower state population after pumping compared to the unpumped sample (Figure 1.3(b)). As the lower state population has been excited, the probe will encounter reduced ground state population density when transmitting though the sample, so that more probe light will reach the detector, and the peak will appear negative. If the excited state undergoes stimulated emission in response to the probe pulse, a negative peak will be present on the DAS, where more light reaches the detector than before pumping (Figure 1.3(c)). A stimulated emission peak often exhibits a Stokes shift with respect to the ground state bleach on account of vibrational relaxation of the excited state between the pump and probe pulses. A true DAS spectrum is the superposition of all these signals, and features close together may overlap, as is common when the Stokes shift between the ground state bleach and stimulated emission is small.[17,18]

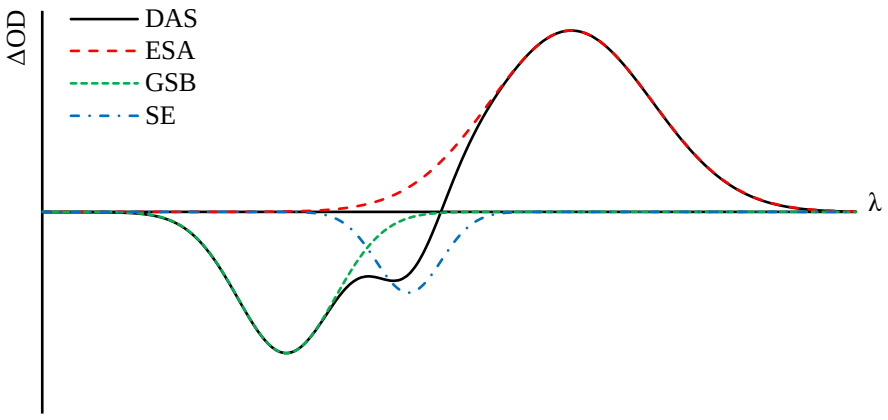

Figure 1.2: Example of contributions to a difference absorption spectrum (DAS). ESA = excited state absorption, GSB = ground state bleach, SE = stimulated emission.

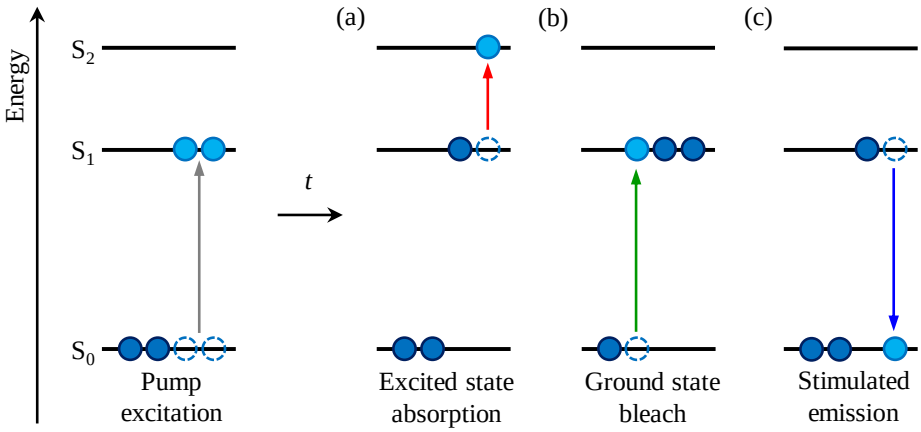

Figure 1.3: Energy level schematic of DAS signal contributions. Solid circles represent relative molecular populations in singlet states S_0-S_2. Some time, *t*, after pump excitation, the sample may show signal contributions as a result of (a) excited state absorption, (b) ground state bleaching or (c) stimulated emission.

1.2.3. Ultrafast Spectroscopy

A number of chemical processes occur on an ultrafast timescale, including photoisomerization,[19–21] solvation dynamics[22–24] and electron transfer,[24,25] which are all accessible by TA spectroscopy. In order to monitor processes on such short timescales, the time resolution of the measurement must be shorter than the processes observed, analogous to the shutter speed on a camera: if the shutter speed is too slow, moving subjects appear blurred. The same is true for ultrafast spectroscopy, where the 'shutter speed' is the temporal width of the pump/probe pulses. Short pulses are required to simultaneously excite wavepackets from the lower state of a molecule to allow them to evolve coherently across the excited state. Concerning the typical distances that molecules or atoms interact on, and the speeds at which they move, time resolutions on the sub-picosecond regime are necessary to probe molecular dynamics. Thus, there is a requirement for ultrashort light pulses for such experiments.

Most commonly, ultrafast pulses for TA experiments are derived from Ti:sapphire lasers or Yb-doped fibre or crystal lasers.[26,27] The former emit close to 800 nm, with pulse durations as low as 5 fs, whereas the latter generate light around 1030 nm pulses at widths down to approximately 200 fs. Yb-doped lasers tend to operate at higher repetition rates, which is often advantageous for shot-to-shot background subtraction or noise suppression, but typically yield lower maximum pulse energies, which are desirable for nonlinear optical process. The stability of both systems is a major benfit, as it allows reliable use of secondary emission sources such as optical parametric amplifiers or supercontinuum generation sources to facilitate precise experimental control by reaching a broad range of the electromagnetic spectrum.

In Chapter 3, the experimental implementation of TA used throughout this thesis is outlined, building on the concepts developed above.

2. Surface Sum-Frequency Generation

Chemistry at surfaces is of fundamental importance across a vast range of chemistry. Solid and liquid interfaces can have distinctly different chemical environments at their surface compared to their bulk, where an interface is primarily what governs the interaction of the substance with its surrounding environment. As such, in any instance a condensed-phase substance is in physical contact with another material, surface chemistry takes effect. In order to properly understand surfaces, their characterisation is essential, which itself requires suitable techniques for examining them. Surface sum-frequency generation (SFG) spectroscopy has become an increasingly popular technique as a result, offering a surface-sensitive method able to probe the structure and ultrafast dynamics of a variety of interfacial systems.

Second-harmonic generation (SHG), the experimental precursor to surface SFG spectroscopy, has been used as surface-sensitive technique since the 1970s, but in that time both methods have evolved significantly in their practical and theoretical understanding. Science has access to an arsenal of surface-sensitive techniques, each with their own advantages and disadvantages, where surface SFG has become a valuable tool owing its use under atmosphere and without damage to the surface under inspection. Furthermore, its capacity to incorporate time resolution to measurements has been instrumental in the study of molecular dynamics at surfaces.

2.1. Linear Optics

In most circumstances, the optical response of a dielectric medium can be approximated as linear with respect to an oscillating electromagnetic field propagating through it so long as the field is weak (as is the case in much of nature). In such conditions, the charge distributions of atoms or molecules within a medium are displaced by the propagating field, inducing time-dependent dipole moments within the material, $\vec{p}(\vec{r},t)$. The net dipole moment per unit volume is the polarisation, $\vec{P}(\vec{r},t)$:[5]

$$\vec{P}(\vec{r},t) = \varepsilon_0 \chi^{(1)} \vec{E}(\vec{r},t) \,, \tag{2.1}$$

where ε_0 is the vacuum permittivity, $\chi^{(1)}$ is the first order (linear) electric susceptibility, and $\vec{E}(\vec{r},t)$ is the oscillating electric field of the propagating wave at time t and position $\vec{r}$, of the form in equation (1.1). In this regime, the polarisation response is linear to the applied field and waves passing through a medium can be considered non-interacting with respect to one another. Equation (2.1) assumes the medium response to be instantaneous with respect to the electric field.[28,29]

2.1.1. Polarisability and Linear Susceptibility

The linear susceptibility of a molecule is linked to its polarisability, which indicates how easily a molecule acquires a dipole in an applied electric field. For a molecule in a static, uniform electric field, a dipole moment $\vec{p}$ is induced. To a linear approximation, the magnitude of the induced dipole is related to the field by the molecule's polarisability, α:[5]

$$\vec{p} = \alpha \vec{E} \,. \tag{2.2}$$

As a result, the molecule's energy U is perturbed by $-\vec{p} \cdot \vec{E}$. For a field in the z-direction, this field may take the form $\vec{E} = \mathcal{E}\hat{k}$ for example, where $\hat{k}$ is the unit vector in the z-direction. According to the Hellman-Feynman theorem,[8]

$$\frac{\mathrm{d}U}{\mathrm{d}E} = -\langle p_z \rangle \,, \tag{2.3}$$

where $\langle p_z \rangle$ is the expectation value of the dipole moment, or the orientationally averaged value. Under the influence of the electric field, the energy of the molecule can be expressed as a Taylor expansion of the form:

$$U = U(0) + \left(\frac{\mathrm{d}U}{\mathrm{d}\mathcal{E}}\right)\mathcal{E} + \frac{1}{2!}\left(\frac{\mathrm{d}^2U}{\mathrm{d}\mathcal{E}^2}\right)\mathcal{E}^2 + \frac{1}{3!}\left(\frac{\mathrm{d}^3U}{\mathrm{d}\mathcal{E}^3}\right)\mathcal{E}^3 + \cdots \,. \tag{2.4}$$

By expanding around $\mathcal{E} = 0$, and using (2.3), the total dipole moment of the molecule in the electric field is expressed as:

$$\langle p_z \rangle = p_{0z} + \alpha_{zz}\mathcal{E} + \frac{1}{2}\beta_{zzz}\mathcal{E}^2 + \cdots \ . \tag{2.5}$$

The first term, p_{0z} is any permanent dipole the molecule possesses outside of an applied field. The second term corresponds to the linear polarisability of the molecule in the *z*-direction, as seen in (2.2). The third term corresponds to its first (nonlinear) hyperpolarisability in the *z*-direction, β_{zzz}. Higher order hyperpolarisability terms are apparent at higher order expansions.

Polarisability is a second rank tensor to account for dipole moments induced along all three Cartesian axes by a field component along any one axis. To denote this, the subscripts are ordered such that the foremost label is the direction of the induced dipole component and the lattermost label is the applied field component that causes this. For example, the tensor component α_{xz} would relate to the magnitude of a dipole induced along the *x*-direction from the field in the *z*-direction. More comprehensively, a component of the dipole induced in a molecule along the *i*-axis, as in (2.2), may be rewritten as[30]

$$p_i = \sum_j \alpha_{ij} E_j \ , \tag{2.6}$$

where *i* and *j* each refer to an index of a Cartesian axis.

It can be seen from higher order terms in (2.5) that polarisation caused by the hyperpolarisability, β, scales nonlinearly with the applied field, and the hyperpolarisability itself can be represented as a third rank tensor. The first subscript refers to the direction in which a dipole moment is induced from field components acting in the directions of the latter two subscripts. For example, β_{zxy} would relate to the magnitude of a dipole induced along the *z*-direction from the *x*- and *y*-components of an applied field.

Since the linear polarisation of a material is its net dipole moment per unit volume, $\chi^{(1)}$ can be expressed in terms of the material's polarisability by considering the approximate local field, E_{local}, of each dipole:[8,31]

$$E_{\text{local}} = E + \frac{P}{3\varepsilon_0} \ . \tag{2.7}$$

The definition of polarisability states that:

$$P = \alpha N E_{\text{local}} \ , \tag{2.8}$$

where N is the number density of dipoles or polarisable species per unit volume. With additional comparison to (2.1), $\chi^{(1)}$ can be expressed as:

$$\chi^{(1)} = \frac{3\alpha N}{3\varepsilon_0 - \alpha N} \ , \tag{2.9}$$

or, where $E_{\text{local}} = E$, in relation to the orientationally averaged polarisability of a material, $\langle\alpha\rangle$:[32]

$$\chi^{(1)} = \frac{N}{\varepsilon_0}\langle\alpha\rangle \ . \tag{2.10}$$

In general, unlike for idealised materials that are lossless and dispersionless, the polarisation and susceptibility for real materials are complex:[28]

$$\chi^{(1)} = \text{Re}\left(\chi^{(1)}\right) + \text{Im}\left(\chi^{(1)}\right)i \ . \tag{2.11}$$

The real and imaginary parts of an electric susceptibility characterise the transmissive and absorptive behaviour of a medium,[33] respectively, and are thus often strongly frequency dependent (Figure 2.1). Hence, $\chi^{(1)}$ may be more generally expressed as $\chi^{(1)}(\omega)$. The relative permittivity of the medium, $\varepsilon(\omega)$, is

$$\varepsilon(\omega) = \varepsilon_0(\chi^{(1)}(\omega) \ + \ 1) \ , \tag{2.12}$$

which is the square of the material's refractive index: $\sqrt{\varepsilon(\omega)} = n(\omega)$.

2.2. Nonlinear Optics

The invention of the maser, and subsequently the laser,[34] paved the way for breakthroughs into the world of nonlinear optical phenomena. Their previously unseen high intensity outputs led to the first demonstration of bulk SHG by Franken *et al* in 1961,[35] and then bulk SFG only a few months later.[36]

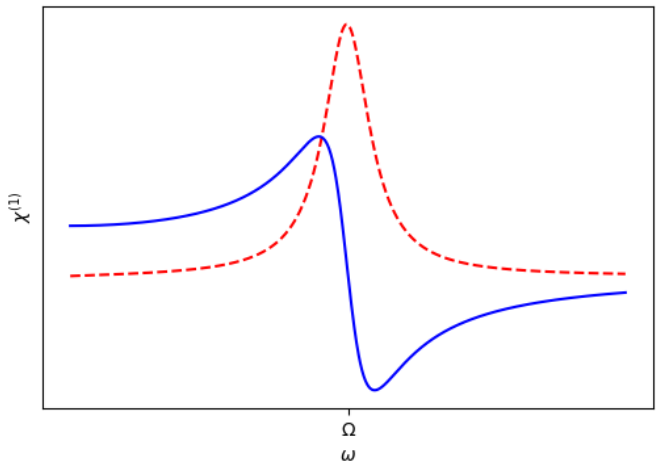

Figure 2.1: General form of the linear electric susceptibility as a function of frequency, ω, from the anharmonic solution to (2.13). The real component is shown as a solid blue line, the imaginary component as a dashed red line.

2.2.1. Origins of Optical Nonlinearity

In the same way that anharmonic oscillator potentials can be approximated to those of harmonic ones, provided displacement from equilibrium is small, nonlinear optical responses may appear linear at low field intensities. In dielectric media, where nuclei and their electrons are bound together, applied electric fields displace the positive and negative charges of its constituent particles in opposite directions, inducing dipoles. A sinusoidally oscillating electric field will therefore induce sinusoidally oscillating dipoles in the particles' charge distributions.

In a classical picture, an electron of mass m and a parent ion form an anharmonic oscillator, assumed here to have displacement parallel to the applied field along the x axis. The nuclei, given their large mass compared to the electron, are considered stationary. For a collection of non-interacting dipoles, the equation of motion of an oscillator can be expressed as[37]

$$-eE(x,t) = m\left[\frac{\mathrm{d}^2x}{\mathrm{d}t^2} + 2\Gamma\frac{\mathrm{d}x}{\mathrm{d}t} + \Omega^2 x - (\xi^{(2)}x^2 + \xi^{(3)}x^3 + \ldots)\right], \tag{2.13}$$

where e is the charge magnitude of an electron, $E(x,t)$ is the oscillating electric field of the form in (2.14), x is the displacement for equilibrium, Γ is the damping coefficient, Ω is the resonance frequency and $\xi^{(n)}$ are anharmonicity coefficients. (2.13) equates the net electrostatic force on the electron $F = eE$, to that of the potential. The radiation has a frequency ω and amplitude $\vec{\mathcal{E}}$, where, in a more general sense, $E(x,t)$ is not necessarily parallel to the x-axis:

$$\vec{E}(\vec{r},t) = \vec{\mathcal{E}}\cos\left(\vec{k}\cdot\vec{r} - \omega t\right) = \tfrac{1}{2}\vec{\mathcal{E}}\left[\exp(i\vec{k}\cdot\vec{r} - i\omega t) + \exp(-i\vec{k}\cdot\vec{r} + i\omega t)\right] . \qquad (2.14)$$

When the anharmonic terms in (2.13) are neglected, the solution to the induced polarisation in the material is given as in (2.1), and the polarisation response is linear with respect to the electric field. Realisation of the anharmonic terms gives rise to a non-exact solution to the equation of motion, however when the anharmonic terms are small, $\vec{P}(\vec{r},t)$ can be approximated by a power series in $\vec{E}(\vec{r},t)$:

$$\vec{P}(\vec{r},t) = \varepsilon_0 \left(\chi^{(1)}\vec{E}(\vec{r},t) + \chi^{(2)}\vec{E}^2(\vec{r},t) + \chi^{(3)}\vec{E}^3(\vec{r},t) + \cdots\right) . \qquad (2.15)$$

Here $\chi^{(2)}$, $\chi^{(3)}$ etc. are the nonlinear susceptibilities of the material, which, as with the linear susceptibility, may have both real and imaginary components. It is common for the polarisation to be expressed as a sum of *n*th order polarisation components:

$$\vec{P}(\vec{r},t) = \vec{P}^{(1)}(\vec{r},t) + \vec{P}^{(2)}(\vec{r},t) + \vec{P}^{(3)}(\vec{r},t) + \cdots , \qquad (2.16)$$

where the first nonlinear polarisation term, $\vec{P}^{(2)}(\vec{r},t)$, will be the most prevalent here:

$$\vec{P}^{(2)}(\vec{r},t) = \varepsilon_0 \chi^{(2)}\vec{E}^2(\vec{r},t) \ . \qquad (2.17)$$

It should become apparent from the expression for the polarisation in (2.15), using a wave in the form of (2.14), that for example, the $\varepsilon_0\chi^{(2)}\vec{E}^2(\vec{r},t)$ term will result in a sinusoidally oscillating component with frequency 2ω, and the $\varepsilon_0\chi^{(3)}\vec{E}^3(\vec{r},t)$ term with a component at 3ω. Furthermore, it is well known that oscillating dipoles have the capacity to emit radiation at their frequency of oscillation.[5] Hence a dielectric, illuminated with sufficiently intense radiation of frequency ω, can radiate a field at frequencies 2ω, 3ω etc.; the basis for harmonic generation. This is equivalent to simultaneously destroying *n* photons of energy $h\omega$ and creating one photon of energy $nh\omega$ within the medium. As well as forming components of $\vec{P}(\vec{r},t)$ oscillating at higher frequencies, a component can also be formed that does not oscillate in time. This serves to place a static electric field across the material, termed optical rectification.[38,39] Analysis of $\chi^{(2)}$ shows two resonance frequencies, one at Ω, and a second at $\Omega/2$ (Figure 2.2). These correspond to conditions when the fundamental frequency matches Ω, or the second harmonic matches Ω.

As can be seen in Figure 2.2, the real and imaginary components of $\chi^{(n)}$ vary strongly around resonances, and in the case of the nonlinear susceptibility $\chi^{(2)}$, in order to be completely real, the medium must be perfectly transmissive at both the fundamental and second-harmonic frequencies.[40]

If the high-intensity electric field has more than one distinct frequency component, additional phenomena manifest under similar conditions. For example, consider a wave that is instead a superposition of two frequencies, ω_1 and ω_2:

$$\vec{E}(\vec{r},t) = \frac{1}{2}\left[\vec{\mathcal{E}}_1 \exp(i\vec{k}_1\cdot\vec{r} - i\omega_1 t) + \vec{\mathcal{E}}_2 \exp(i\vec{k}_2\cdot\vec{r} - i\omega_2 t) + \text{c.c.}\right], \qquad (2.18)$$

where $\vec{\mathcal{E}}_n$ is the amplitude for each component with frequency ω_n and c.c. denotes the complex conjugate of all preceding terms within the same set of square brackets. In these conditions, analysis of all five second order terms from (2.15) still yields a term dependent on $2\omega_1$ and another on $2\omega_2$, corresponding to SHG of each fundamental frequency. A third term is frequency independent, relating to optical rectification. Two additional frequency-dependent terms arise that depend on $(\omega_1 + \omega_2)$ and $(\omega_1 - \omega_2)$, corresponding to sum-frequency generation (SFG) and difference-frequency generation, respectively. Each of these processes have specific phase-matching conditions, and usually only one process will ever generate a dominant output signal, which can be selected by the input wave polarisation and medium orientation.

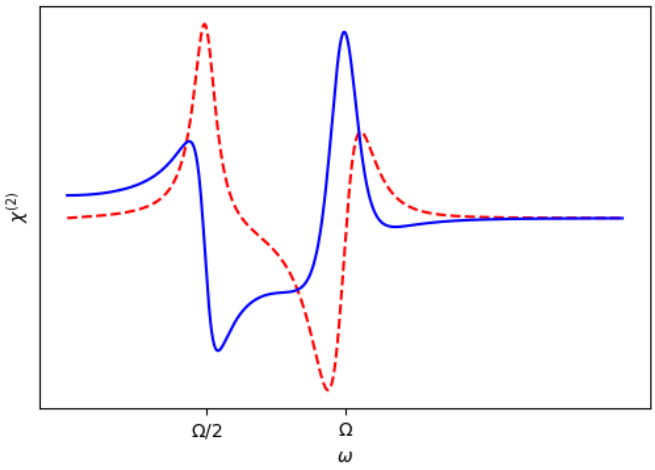

Figure 2.2: General form of the first order nonlinear electric susceptibility as a function of frequency, ω, from the anharmonic solution to (2.13). The real component is shown as a solid blue line, the imaginary component as a dashed red line.

2.2.2. Nonlinear Susceptibility

The following analysis closely follows that of Boyd.[28] For an optical wave of many frequency components, the electric field vector of the wave can be expressed similarly to (2.18), but summed over all (positive) frequency components ω_n. At position $\vec{r}$ within the material:

$$\vec{E}(\vec{r},t)= \sum_n \frac{1}{2}\vec{\mathcal{E}}_n\left[\exp\left(i\vec{k}_n\cdot\vec{r} - i\omega_n t\right) + \text{c.c.}\right] , \tag{2.19}$$

where $\vec{k}_n$ is the wave vector for the component of frequency ω_n. Alternatively,

$$\vec{E}(\vec{r},t)= \sum_n \vec{\mathcal{E}}_n \cos\left(\vec{k}_n\cdot\vec{r} - \omega_n t\right) , \tag{2.20}$$

where, for brevity, the following notation may be adopted as in the source material:[28]

$$\vec{E}_n = \vec{E}(\omega_n) , \tag{2.21}$$

and likewise for similar functions or variables such as the amplitudes of the polarisation, $\vec{\mathcal{P}}(\omega_n)$. Thus, the material's polarisation can be expressed as:

$$\vec{P}(\vec{r},t) = \sum_n \frac{1}{2}\vec{\mathcal{P}}_n\left[\exp\left(i\vec{k}_n\cdot\vec{r} - i\omega_n t\right) + \text{c.c.}\right] , \tag{2.22}$$

summing over all positive nonzero frequencies. Likewise to (2.17), the components of $\chi^{(2)}$ along the three Cartesian axes, $\chi^{(2)}_{ijk}$, should relate the amplitude of the induced polarisation field along the *i*-axis, P_i, to the electric field components along the *j*- and *k*-axes. In the case of SFG:

$$P_i^{(2)}(\omega_{\text{SFG}}) = 2\varepsilon_0 \sum_{jk} \chi_{ijk}^{(2)}(\omega_{\text{SFG}};\omega_1,\omega_2)E_j(\omega_1)E_k(\omega_2) , \tag{2.23}$$

where $\omega_{\text{SFG}} = \omega_1 + \omega_2$, and the notation $\chi_{ijk}^{(2)}(\omega_{\text{SFG}};\omega_1,\omega_2)$ is to show that the first argument is always the sum of the latter two.[28] The latter two arguments are important to explicitly show, for example, when the sum frequency is a result of either SFG or SHG.

Following analysis of the anharmonic oscillator of a noncentrosymmetric medium as in (2.13), $\chi^{(1)}(\omega)$ can be expressed as

$$\chi^{(1)}(\omega) = \frac{Ne^2}{m\varepsilon_0 D(\omega)}, \tag{2.24}$$

where $D(\omega_j)$ is a complex denominator function, used for shorthand:[28]

$$D(\omega_j) = \Omega^2 - \omega_j^2 - 2i\omega_j\Gamma . \tag{2.25}$$

$\chi^{(2)}(\omega_{SFG};\omega_1,\omega_2)$ can then be expressed as

$$\chi^{(2)}(\omega_{SFG};\omega_1,\omega_2) = \frac{Ne^3\zeta^{(2)}}{m^2\varepsilon_0 D(\omega_{SFG})D(\omega_1)D(\omega_2)} . \tag{2.26}$$

Analogous to the relationship between linear susceptibility and polarisability, $\chi^{(2)}$ is related to the orientationally-averaged molecular hyperpolarisabilities of a sample,[32,41,42]

$$\chi^{(2)} = \frac{N}{\varepsilon_0}\langle\beta\rangle . \tag{2.27}$$

It is thus noted that the nonlinear susceptibility of a material can be used to deduce the net alignment and concentration of polarisable species that contribute to it, which becomes an important consideration in the exploitation of this phenomenon for spectroscopic measurements.[43]

2.2.3. Properties of Nonlinear Susceptibilities

SFG is a nonlinear process describing the interplay of three waves in three dimensions, and to fully characterise the interaction, the polarisation of each component must be known. As in (2.23), the summation shows the need to consider the complete set of orientations of the interacting fields.

When considered more generally:[28]

$$P_i^{(2)}(\omega_n + \omega_m) = \varepsilon_0 \sum_{jk} \sum_{(nm)} \chi_{ijk}^{(2)}(\omega_n + \omega_m, \omega_n, \omega_m) E_j(\omega_n) E_k(\omega_m) \ , \tag{2.28}$$

where the summation over (*nm*) indicates that the sum of *n* and *m* must stay constant. This gives rise to twelve total tensors: $\chi_{ijk}^{(2)}(\omega_n + \omega_m, \omega_n, \omega_m)$ and all permutations of its positive and negative arguments. Each tensor has many elements, so it is convenient to simplify them by symmetry arguments. The first is that polarisation, $P_i(\vec{r},t)$, and electric fields are physically measurable, so must be real.[28] This can be seen in equations (2.14) and (2.19). This therefore imposes that

$$\chi_{ijk}^{(2)}(-\omega_n - \omega_m, -\omega_n, -\omega_m) = \chi_{ijk}^{(2)}(\omega_n + \omega_m, \omega_n, \omega_m)^* \ , \tag{2.29}$$

Additionally, in a lossless medium, all components of $\chi_{ijk}^{(2)}(\omega_n + \omega_m, \omega_n, \omega_m)$ are real when all frequency components of the electric field, and the polarisations they induce, are far from a resonance.

2.2.3.1. Symmetries

In (2.28), the order of the indices *j*, *k*, and *n*, *m* are interchangeable, thus

$$\chi_{ijk}^{(2)}(\omega_n + \omega_m, \omega_n, \omega_m) = \chi_{ikj}^{(2)}(\omega_n + \omega_m, \omega_m, \omega_n) \ , \tag{2.30}$$

This is known as intrinsic permutation symmetry, equivalent to physically exchanging the two fields used in an experiment, which shows that neither field holds precedence over the other. Note, however, that this is only strictly true when considering SHG, where the fundamental fields are degenerate; in SFG, the distinct frequencies of both fields prevent this exchange. Furthermore, the first nonlinear susceptibility displays full permutation symmetry between the frequency arguments and Cartesian coordinates. For example:

$$\chi_{ijk}^{(2)}(\omega_o = \omega_n + \omega_m) = \chi_{jki}^{(2)}(-\omega_n = \omega_m - \omega_o) \ . \tag{2.31}$$

The negative signs arise as the first argument must be the sum of the latter two.

Supplementing with (2.29) and using the fact that $\chi^{(2)}$ is real in a lossless medium, it can be seen that

$$\chi^{(2)}_{ijk}(\omega_o = \omega_n + \omega_m) = \chi^{(2)}_{kij}(\omega_m = \omega_o - \omega_n) \; ; \tag{2.32}$$

a good example of how symmetry arguments narrow down the number of unique tensor elements.

Kleinman symmetry concerns nonlinear processes where the frequency of interacting waves is significantly smaller than those of the system resonances.[44] When this is true, $\chi^{(2)}$ can be taken to be approximately a constant, seen in Figure 2.2. The property of full permutation symmetry applies, as in (2.32), but as $\chi^{(2)}$ is independent of frequency, the cartesian indices can be exchanged freely, independent of the frequency indices:

$$\chi^{(2)}_{ijk}(\omega_o = \omega_n + \omega_m) = \chi^{(2)}_{kij}(\omega_o = \omega_n + \omega_m) \; , \tag{2.33}$$

or for any permutation of indices *i*, *j*, and *k* on the right-hand side. Kleinman symmetry is taken to be valid far from resonances and when the material is dispersionless, as the symmetry breaks down when approaching resonances.[45] Furthermore, Kleinman symmetry has been shown to be restricted in its general application by the difficulty in fulfilling its derivation criteria in many optical media,[46] and is strictly valid only under static fields.

Within the electric dipole approximation, SFG is not predicted to be generated in all media at sufficiently high electric fields and is constrained by the symmetry of the medium. If the medium possesses inversion symmetry, it should be expected that if $x \rightarrow -x$, then $\vec{P}(x) \rightarrow -\vec{P}(x)$ also. In the case of the first nonlinear polarisation term in (2.17), this is only feasible when $\chi^{(2)}$ vanishes. This argument is similar for all even-order susceptibility terms, indicating that SFG, and generation of even order fields, should only be prevalent where centrosymmetry is broken. As a result, the bulk of many solid-state homogenous media, covering many crystal classes and all liquids, should exhibit no SFG or other second order processes. However, at the surfaces of such solid-state media, the inversion symmetry is broken over short distances, which allows the second order processes to occur.[47] This is a key aspect that underpins the use of SFG for surface sensitive measurements on homogenous media, as even highly symmetric crystals can produce SFG from their surfaces.[48] This is not without its challenges, however, as the efficiency of such processes is very low. As many as 10^{12} photons are required to generate a single second-harmonic photon from a surface.[28]

This limitation has been mitigated by the use of high intensity laser systems and sensitive detectors now commonplace in modern optical setups.

Regarding liquid surfaces, on which the surface SFG work in this thesis is concerned, the symmetry of the surface also proves a major asset in reducing the independent terms of $\chi^{(2)}$. Neumann's principle, that a physical property of a medium must contain the spatial symmetry elements of its symmetry group, is a useful tool for studying nonlinear effects at surfaces, implying that $\chi^{(2)}$ transforms according to the symmetry group of the material's surface.[49] Most liquid surfaces are of the group $C_{\infty v}$, orientated in the *x*-*y* plane, and so transform as the groups 4mm or 6mm, reducing the number of unique elements in the $\chi^{(2)}$ tensor of the surface to only a few terms (Figure 2.3). Due to the highly symmetric nature of such an interface, only seven terms in the susceptibility tensor are nonvanishing, and on account of previous symmetry arguments, an even fewer number are unique:[50]

$$\chi^{(2)}_{xxz} = \chi^{(2)}_{xzx} = \chi^{(2)}_{yzy} = \chi^{(2)}_{yyz},$$
$$\chi^{(2)}_{zxx} = \chi^{(2)}_{zyy}, \tag{2.34}$$
$$\chi^{(2)}_{zzz}.$$

It can be seen from (2.34) the effects of intrinsic permutation symmetry and the fact that the *x*- and *y*-axes are considered degenerate.

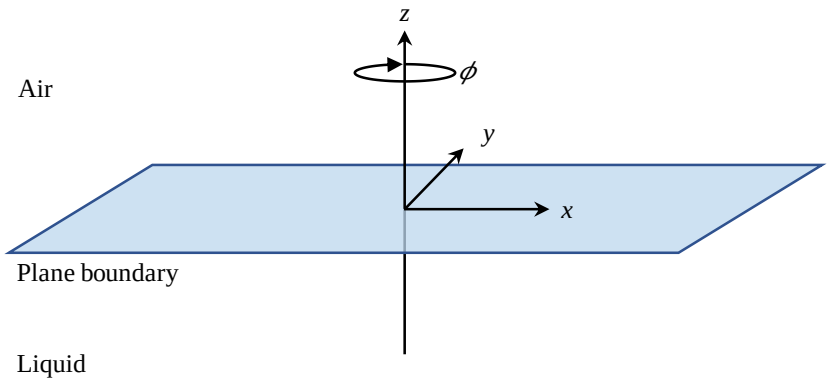

Figure 2.3: Symmetry of a liquid-air interface. For an isotropic liquid surface, the surface shows invariance under any size rotation ϕ.

2.2.4. Waves at Interfaces

Understanding SFG from interfaces requires some consideration as to the optical processes that occur at boundaries between media, between a condensed-phase medium and any other phase. In general, light incident on an interface between two media is reflected or transmitted in a linear-response regime, whereas higher-order processes lead to the observation of additional phenomena. Quantitative description requires insight into the boundary conditions that constrain the incident and outgoing waves, derived from Maxwell's equations.

2.2.4.1. Boundary Conditions

All electromagnetic fields must obey Maxwell's equations:[5]

$$\vec{\nabla} \cdot \vec{E} = -\frac{1}{\varepsilon} \vec{\nabla} \cdot \vec{P} \,, \tag{2.35}$$

$$\vec{\nabla} \cdot \vec{B} = 0 \,, \tag{2.36}$$

$$\vec{\nabla} \times \vec{E} = -\frac{\partial \vec{B}}{\partial t} \,, \tag{2.37}$$

$$\vec{\nabla} \times \vec{B} = \varepsilon\mu \left(\frac{1}{\varepsilon} \frac{\partial \vec{P}}{\partial t} + \frac{\partial \vec{E}}{\partial t} \right) . \tag{2.38}$$

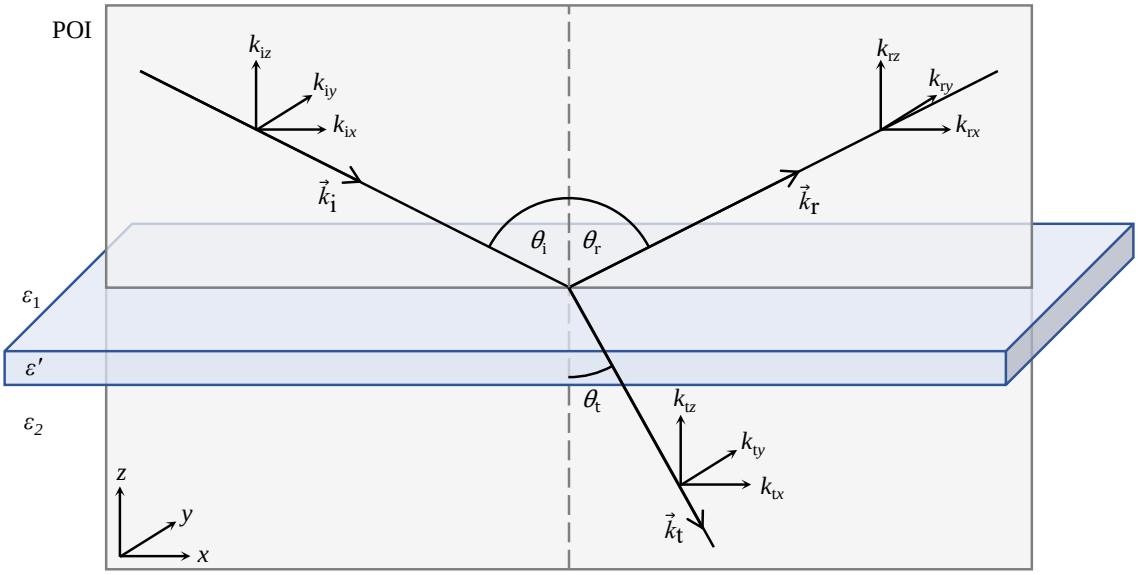

Figure 2.4: Geometry of light rays at an interface between two media in the *x*-*y* plane, showing the incident, reflected and transmitted waves of the fundamental frequency. POI = plane of incidence.

The above equations apply to a material with dielectric constant ε, relative permeability μ, and waves of electric and magnetic fields $\vec{E}$ and $\vec{B}$, respectively. Furthermore, transmitted and reflected wave components must obey Maxwell's equations on both sides of any interface, giving rise to boundary conditions.

For a wave incident on an interface which lies in the *x*-*y* plane, $\vec{E}_{\mathrm{i}}$, reflected and transmitted components, $\vec{E}_{\mathrm{r}}$ and $\vec{E}_{\mathrm{t}}$, respectively, will be generated. If the incident wave's polarisation lies in the *x*-*z* plane, the reflected and transmitted waves will also remain in that plane, i.e. all three waves will have a *y*-component of their wavevector $k_y = 0$. Additionally, all three waves will have a constant *x*-component, set by the incident wave.[51] The plane in which all three waves lie is termed the plane of incidence (POI), which includes the surface normal (Figure 2.4). The paths of the three waves can be constructed by simple geometry to show the angles of incidence and reflection, θ_{i} and θ_{r}, respectively are equal, and to derive Snell's law.[5]

Maxwell's equations can be equated for the total fields on each side of the boundary, giving rise to the following boundary conditions:[52]

$$(\varepsilon_1 E_1 + 4\pi P_1)_{\perp} = (\varepsilon_2 E_2 + 4\pi P_2)_{\perp} , \tag{2.39}$$

$$(E_1)_{\parallel} = (E_2)_{\parallel} , \tag{2.40}$$

$$(B_1)_{\perp} = (B_2)_{\perp} , \tag{2.41}$$

$$(B_1)_{\parallel} = (B_2)_{\parallel} , \tag{2.42}$$

where labels 1 and 2 refer to each of the two media, and $\perp$ or $\parallel$ refer to components of fields perpendicular or parallel to the *x*-*y* interface, respectively.

2.2.4.2. Fresnel Coefficients

When traversing between different media by reflection and transmission, the intensity of a wave is diminished at each event, as each boundary causes part of the wave to be reflected and part to be transmitted. The Fresnel coefficients give the relative amplitude of a transmitted or reflected wave to that of the incident wave, and are individual for the components parallel or perpendicular to the interface. For an incident wave polarised in the *x*-*z* plane, the Fresnel coefficients are:[53]

$$r_{\perp} = -\frac{\sin(\theta_i - \theta_t)}{\sin(\theta_i + \theta_t)} \,, \tag{2.43}$$

$$r_{\parallel} = +\frac{\tan(\theta_i - \theta_t)}{\tan(\theta_i + \theta_t)} \,, \tag{2.44}$$

$$t_{\perp} = \frac{2\,\sin\theta_t\,\cos\theta_i}{\sin(\theta_i + \theta_t)} \,, \tag{2.45}$$

$$t_{\parallel} = \frac{2\,\sin\theta_t\,\cos\theta_i}{\sin(\theta_i + \theta_t)\,\cos(\theta_i - \theta_t)} \,, \tag{2.46}$$

where r and t are the coefficients for reflection and transmission, respectively (Figure 2.5). The angles are defined in Figure 2.4, and for collinear ω_1 and ω_2 fields are only equal in θ_i. While SFG experiments typically make use of a signal reflected from the surface, the fundamental wave must first be transmitted into the interface in order to generate a response, which requires appreciation of both the reflected and transmitted waves at each frequency.

2.2.4.3. SFG at an interface

It is the interface polarisation that is responsible for generation of the sum frequency wave, caused by the oscillations of the incident fundamental waves. The incident fields ω_1 and ω_2 can arrive at any angle of incidence, which does not need to be the same for both fields, so long as they are spatially overlapped in the interfacial region of interest. Here this discussion will consider collinear fields with a common angle of incidence, as was used throughout experimental work in this thesis, though much of the discussed theory is general, or readily generalised. The interface polarisation term that forms the sum frequency, $\vec{P}^{(2)}(\omega_{SFG})$, termed the nonlinear source term, is formed by components of the fundamental waves transmitted into the interface:[51,54]

$$\vec{P}^{(2)}(\omega_{SFG}) = \chi^{(2)}(\omega_{SFG})\,\vec{E}_t(\omega_1)\,\vec{E}_t(\omega_2)\exp\left[i(\vec{k}_S^{(\omega_{SFG})}\cdot\vec{r} - \omega_{SFG}t)\right], \tag{2.47}$$

where $\vec{k}_S^{(\omega_{SFG})}$ is the wavevector of the nonlinear source polarisation, equal to $\vec{k}_t^{(\omega_1)} + \vec{k}_t^{(\omega_2)}$. The superscript indicates it belongs to a wave at frequency ω_{SFG}.

The nonlinear source polarisation shares the same *x*- and *y*-components as the sum-frequency waves it generates:

$$\vec{k}_{\mathrm{t}x}^{(\omega_1)} + \vec{k}_{\mathrm{t}x}^{(\omega_2)} = \vec{k}_{\mathrm{S}x}^{(\omega_{\mathrm{SFG}})} = \vec{k}_{\mathrm{r}x}^{(\omega_{\mathrm{SFG}})} = \vec{k}_{\mathrm{t}x}^{(\omega_{\mathrm{SFG}})}, \tag{2.48}$$

where $\vec{k}_{\mathrm{r}x}^{(\omega_{\mathrm{SFG}})}$ and $\vec{k}_{\mathrm{t}x}^{(\omega_{\mathrm{SFG}})}$ are the *x*-components of the sum-frequency wavevector for the reflected and transmitted waves, respectively (Figure 2.6). In the geometry presented, with the POI at $y = 0$, the same is true for all wavevector *y*-components, which are zero. Together these represent conservation of photon momentum tangential to the interface. For a vacuum-condensed phase interface ($\varepsilon_1 = 1$), the magnitudes of the wavevectors in (2.48) are given by

$$\left|\vec{k}_{\mathrm{t}}^{(\omega_{\mathrm{SFG}})}\right| = \frac{\omega_{\mathrm{SFG}}\sqrt{\varepsilon_2 \omega_{\mathrm{SFG}}}}{c}, \tag{2.49}$$

where *c* is the speed of light.

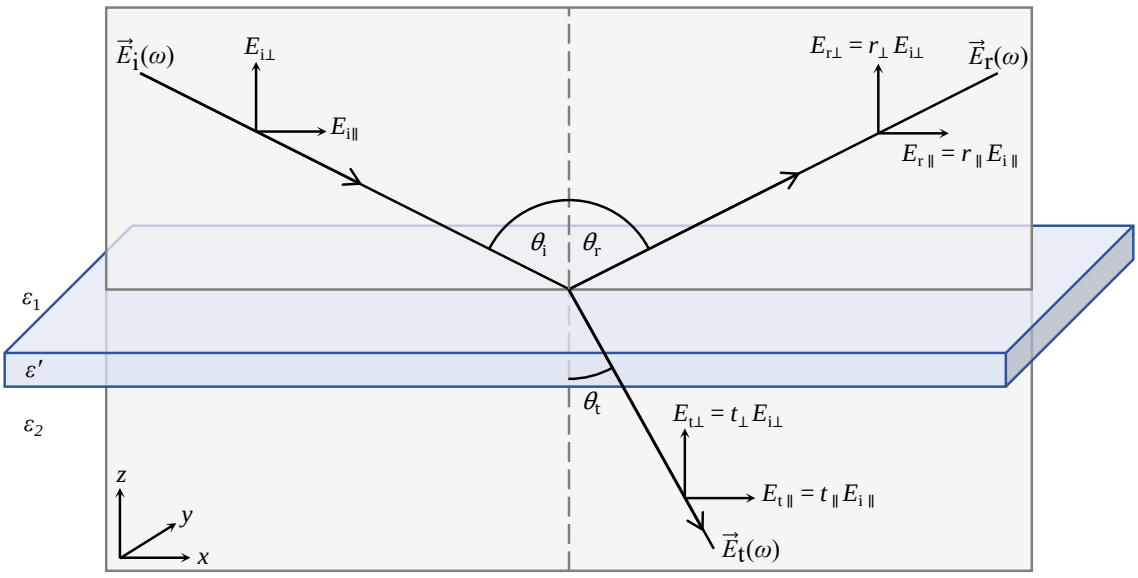

Figure 2.5: Geometry of parallel and perpendicular components of light waves at an interface.

The angles at which the nonlinear source term and the reflected and transmitted sum-frequency waves are formed at are thus found:

$$\sin\theta_{\mathrm{s}} = \frac{\sin\theta_{\mathrm{i}}}{\sqrt{\varepsilon_2(\omega_{\mathrm{SFG}})}}\,, \tag{2.50}$$

$$\sin\theta_{\mathrm{r}}^{(\omega_{\mathrm{SFG}})} = \sin\theta_{\mathrm{i}}\,, \tag{2.51}$$

$$\sin\theta_{\mathrm{t}}^{(\omega_{\mathrm{SFG}})} = \frac{\sin\theta_{\mathrm{i}}}{\sqrt{\varepsilon_2(\omega_{\mathrm{SFG}})}}\,, \tag{2.52}$$

where the angles $\theta_{\mathrm{r}}^{(\omega_{\mathrm{SFG}})}$ and $\theta_{\mathrm{t}}^{(\omega_{\mathrm{SFG}})}$ are defined in Figure 2.6. θ_{s} is the angle at which the nonlinear source polarisation is directed into the medium. Note that in general, the dielectric constant is a function of wavelength, so $\varepsilon_2(\omega_1) \neq \varepsilon_2(\omega_2) \neq \varepsilon_2(\omega_{\mathrm{SFG}})$, and the refracted transmission angles inside medium 2 are different for each field due to dispersion within the medium. By similar reasoning, (2.51) is only strictly true when $\varepsilon_1 = 1$, though when medium 1 is air this is approximately true.

The magnitudes of the sum-frequency fields produced, $E(\omega_{\mathrm{SFG}})$, are derived via the boundary conditions presented previously. Each of the reflected, $\vec{E}_{\mathrm{r}}(\omega_{\mathrm{SFG}})$, and transmitted, $\vec{E}_{\mathrm{t}}(\omega_{\mathrm{SFG}})$, waves can be resolved into two components parallel or perpendicular to the interface.[51] Here, the focus is on the sum-frequency component reflected from the surface, as this is typically measured experimentally. The magnitude of the reflected SFG component can be resolved into two polarisations:[55]

$$E_{\mathrm{P}}(\omega_{\mathrm{SFG}}) = 4\pi i k_{\mathrm{i}} \frac{k_{\mathrm{tz}} P_x + \left(\frac{\varepsilon_2}{\varepsilon'}\right) k_{\mathrm{ix}} P_z}{\varepsilon_2 k_{\mathrm{iz}} + \varepsilon_1 k_{\mathrm{tz}}}\,, \tag{2.53}$$

$$E_{\mathrm{S}}(\omega_{\mathrm{SFG}}) = 4\pi i k_{\mathrm{i}} \frac{k_{\mathrm{i}} P_y}{\varepsilon_1 k_{\mathrm{iz}} + \varepsilon_1 k_{\mathrm{tz}}}\,, \tag{2.54}$$

where ε' is the dielectric constant of the interface, and all k refer to the SFG wave. The labels P and S correspond to the components parallel and perpendicular to the POI, respectively (Figure 2.6). The polarisation terms P_i are found via equation (2.23), where each will use the susceptibility of the form $\chi_{ijk}^{(2)}$.

Hence, at an isotropic liquid surface the $E_S(\omega_{SFG})$ component is generated by a combination of $\chi^{(2)}_{xzx}$ and $\chi^{(2)}_{xxz}$, involving a combination of the electric field components parallel (x) and perpendicular (z) to the interface. This combination of polarisations is abbreviated to SPS or SSP, where the first letter gives the output ω_{SFG} polarisation and the latter two give the input polarisations of ω_1 and ω_2. For SHG with only one incident wave, this is typically abbreviated to SMix, for an S-polarised output, generated by an input wave containing both P and S components. Likewise, for SFG, PSS output components arise from $\chi^{(2)}_{zxx}$, and PPP output components from $\chi^{(2)}_{xxz}$, $\chi^{(2)}_{zxx}$ and $\chi^{(2)}_{zzz}$, by noting the degeneracy of x and y in (2.34).

A reflected sum-frequency wave generated from a surface with P- and S-polarised components can be expressed as

$$\vec{E}(\omega_{SFG}) = E_P(\omega_{SFG})\hat{p} + E_S(\omega_{SFG})\hat{s}\ , \tag{2.55}$$

where $\hat{p}$ and $\hat{s}$ are the unit vectors for P- and S-polarisations, respectively.

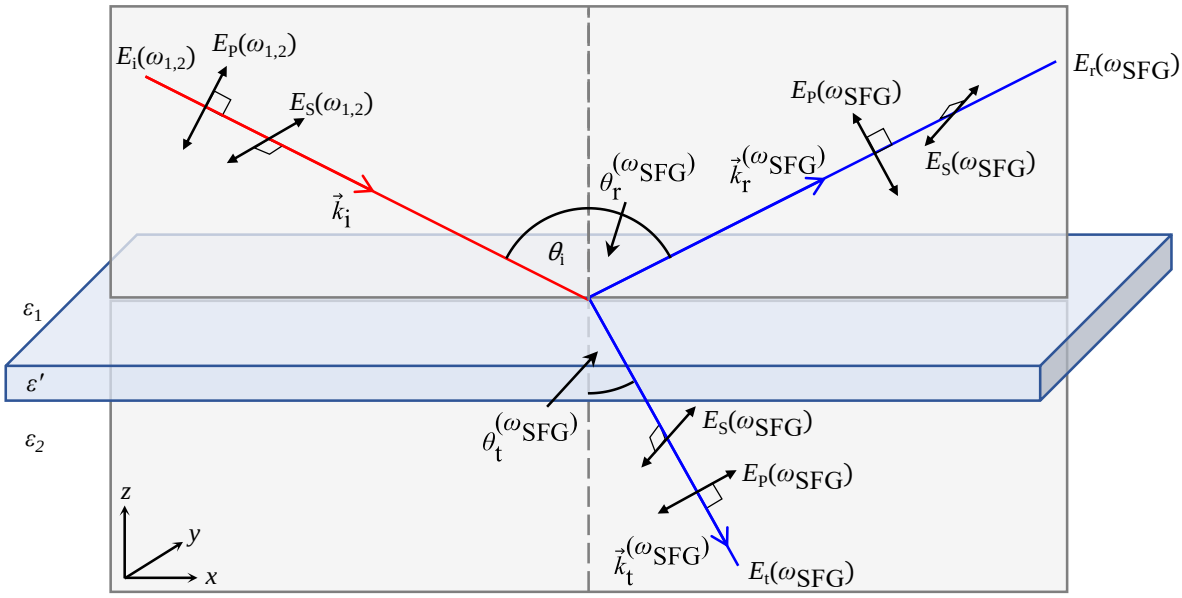

Figure 2.6: Geometry of SFG at an interface, showing the P and S polarisation directions, with P components within the POI and S components perpendicular to it.

The total reflected intensity generated from collinear SFG at a surface, $I(\omega_{SFG})$, is:[56,57]

$$I(\omega_{SFG}) = \frac{8\pi^3\omega_{SFG}^2}{c^3\sqrt{\varepsilon_1(\omega_{SFG})\varepsilon_1(\omega_1)\varepsilon_1(\omega_2)}\cos^2\theta_i}\left|\vec{e}_{\omega_{SFG}}\cdot\chi^{(2)}(\omega_{SFG}:\omega_1,\omega_2):\vec{e}_{\omega_1}\vec{e}_{\omega_2}\right|^2 I(\omega_1)I(\omega_2)\,, \qquad (2.56)$$

where $\vec{e}_{\omega_n} = \vec{L}(\omega_n)\cdot\hat{e}_{\omega_n}$. $\vec{L}(\omega_n)$ is the Fresnel factor for the field at frequency ω_n, and $\hat{e}_{\omega_n}$ is the unit polarisation vector at frequency ω_n.

2.2.4.4. Signal Contributions

In reality, measurements of the SFG response from a surface are not as straightforward as measuring a signal and quantifying the nonlinear susceptibility of an interface. Thus far, the above theory has been presented under the electric dipole approximation, in which all response to an applied field is a result of electric dipoles and not any higher-order multipoles, either electric or magnetic. With this added complexity, the sum-frequency response of the medium can be represented as a sum of the response from the surface and that of the bulk, where in general the bulk contributions will arise from higher order electric and magnetic multipoles in centrosymmetric media.[47,48,58,59] While these terms are weak in comparison to those from electric dipoles at the surface, the bulk volume is comparatively much larger, resulting in situations where the bulk contribution may dominate that of the surface. Since the bulk and surface contributions to the sum frequency are indistinguishable from one another, realising and minimising the bulk contribution is crucial to accurate surface-sensitive measurements.

Previous investigations into the relative magnitudes of the surface and bulk contributions have yielded conflicting results. Experimental and theoretical studies of solid-air surfaces have concluded that the two components can be of a similar order of magnitude,[48,60] but have the capacity to be individually resolved, albeit with complications created by material structure, gas phase composition or the requirement for additional samples for reference.[48] An effective approach would be to observe changes in reflected SFG signal caused by changing surface conditions to most definitively observe the relative contributions of the surface and bulk signals,[59] however it has been asserted that for materials with high refractive indices, the surface contribution dominates that of the bulk.[47] In media that are not centrosymmetric, the bulk contribution overwhelms that from the surface,[50] making such media poor candidates for surface-sensitive analysis by SFG or SHG.

As well as quadrupolar contributions from the bulk, surface quadrupolar terms can complicate the interpretation of a surface SFG signal. In the case of metal-air surfaces, the surface quadrupolar contribution has been shown to be of the same order of magnitude, but less significant than the electric dipole contribution, and much less than the surface anisotropy from a rotated surface.[61] Further studies have indicated that the surface quadrupolar contribution can be decreased in comparison to the surface dipole component by matching the refractive indices of the two interfacial media, such as in some liquid-liquid interfaces.[50,62] Furthermore, the surface quadrupolar contribution is less significant for interfaces supporting an adsorbed layer of high polar ordering, resulting in strong asymmetry, or if either of the fundamental or sum frequencies is near a strong electric-dipole-allowed resonance of the system.[62–64] Such resonance-enhanced techniques are frequently used for this reason, despite the resulting breakdown of the Kleinman symmetry case.[46,64] Like the electric quadrupolar and magnetic dipolar terms arising from the bulk, these multipole surface contributions to the total sum-frequency signal at an interface are in general indistinguishable in surface SFG measurements, and their minimisation for accurate measurements is highly sought-after.

2.2.4.5. Surface resonances

The nonlinear response measured from a surface experiment is a coherent sum of all the polarisation sources that can result in a nonlinear response. As outlined above, the surface and bulk contributions, which are dipole or higher-order multipole generated, are indistinguishable. Measurement of the magnitude of the surface nonlinear susceptibility will actually be an *effective* surface nonlinear susceptibility, $\chi^{(2)}_{S'}$:[65]

$$\chi^{(2)}_{S'} = \chi^{(2)}_{S} + \chi^{(2)}_{B} , \tag{2.57}$$

where $\chi^{(2)}_{S}$ and $\chi^{(2)}_{B}$ are the surface and bulk nonlinear susceptibilities, respectively. The resonant enhancement of $\chi^{(2)}_{S'}$ in SHG or SFG experiments infers that $\chi^{(2)}_{S'}$ is also a sum of resonant and nonresonant components:[66]

$$\chi^{(2)}_{S'} = \chi^{(2)}_{NR} + \sum_{j}\sum_{n} \frac{A_j(\Omega_j)}{\omega_n - \Omega_j + i\Gamma_j} , \tag{2.58}$$

where $\chi_{NR}^{(2)}$ is the real, nonresonant contribution and A_j, Ω_j and Γ_j are the amplitude, resonance frequency and damping constant for resonance j, respectively. As any of the fields ω_{SFG}, $\omega_{1\text{ or }}$ ω_2 may be resonant with a transition, the resonant term is summed over each field, ω_n. The second term on the right-hand side is the resonant contribution, $\chi_R^{(2)}$. Here, ω is experimentally variable: either the fundamental frequency for SHG or the tuneable (usually IR) component for SFG. The imaginary component, $\mathrm{Im}(\chi_{S'}^{(2)})$, governs absorption resonances of the medium or interface:[40]

$$\mathrm{Im}(\chi_{S'}^{(2)}) = \sum_j \frac{\Gamma_j A_j(\Omega_j)}{(\omega - \Omega_j)^2 + \Gamma_j^2} \ . \tag{2.59}$$

The magnitude of the resonant contribution is linearly dependent on the surface concentration of species of interest, whereas the nonresonant term is approximately independent of the concentration, or is generally assumed to be. Hence, it is the resonant contribution that is of fundamental interest, and which contains real and imaginary components, the latter of which is enhanced significantly at resonances. Since the SFG signal from a surface is proportional to the square of the nonlinear susceptibility, it can be seen from the square of (2.58) that there are terms depending quadratically on surface concentration, and others linearly on them. The relative magnitudes of $\chi_{NR}^{(2)}$ and $\chi_R^{(2)}$, depending on the system and proximity to a resonance, will give rise to a SFG signal that varies between linearly and quadratically with the concentration of a surface species.

2.3. Surface Sum-Frequency Generation Spectroscopy Techniques

Since its first observation in the 1960s, the use of SHG or SFG as experimental techniques, and indeed many other nonlinear optical techniques, have evolved significantly. Key advantages of SFG are its applicability to any interface that can be accessed by light, and the ability to probe surfaces non-destructively. Interest in nonlinear optical techniques as surface probes has increased markedly over the years thanks to several breakthroughs in the field, such as the discovery of surface-enhanced nonlinear processes in the 1970s and ’80s that brought a fresh motivation for the practical use of SFG.[67–70]

Thereafter it has been used to study many interfacial systems, with significant attention devoted to molecular orientation at interfaces,[63] surface symmetry[60,71] and surface dynamics.[72] SFG has even been shown to have use in surface microscopy.[73] More recently, advanced phase-sensitive methods have opened up new ways to study the orientation of species at interfaces, and surface dynamics can be studied on ultrashort timescales via time-resolved methods.

The following discussion will in most cases refer to SFG processes and experiments, however SHG will also be included as it is closely related. Indeed, most early surface nonlinear optical techniques were conducted as electronic surface SHG spectroscopy.

2.3.1. Homodyne Measurements

In its most straightforward form, surface SFG measurements are simply a measure of $\left|\chi^{(2)}\right|^2$ from an interface, as seen through equation (2.56). In practice, both reflective and transmissive geometries are effective, though reflective geometries are perhaps most common due to their applicability on non-transmissive samples. Figure 2.7 shows a setup for a simple surface SHG experiment, as an example of a SFG experiment where the frequencies ω_1 and ω_2 are identical. This illustrates how basic optical equipment can be used to investigate the nonlinear properties of a surface.

As in (2.56), the intensity of the reflected surface SFG signal is linearly dependent on the input intensity of each fundamental frequency, so stable pulsed lasers are highly desirable for these nonlinear measurements due to their high peak power per pulse. Additionally, such lasers may be focussed onto the region of interest to further raise the resultant signal, the limit of which is usually the point at which the surface undergoes laser-induced breakdown. In the past, homodyne techniques have been used to monitor the adsorption and desorption of molecular layers at an interface, such as electrode cycling, as the nonlinear susceptibility of an interface varies with the density of adsorbed molecules.[74,75] Surface nonlinear techniques were shown to possess a high sensitivity to surface adsorbates, which could distinguish them by resonant enhancement,[63] and were also used to follow the process of two-dimensional phase transitions on a liquid surface by inferring molecular orientation.[41]

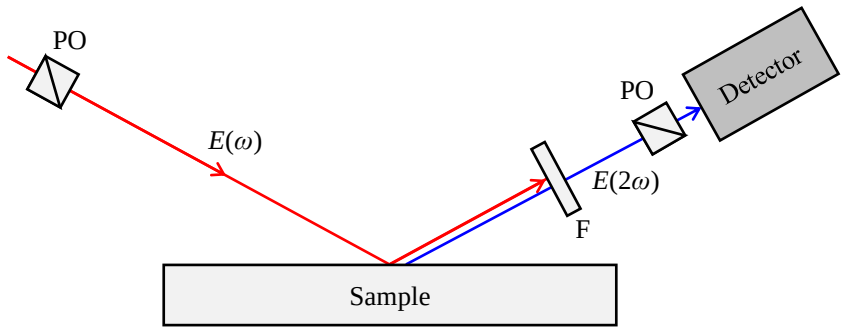

Figure 2.7: Simplified arrangement of optical equipment for a collinear, reflection SHG experiment, where $\omega_{SFG} = 2\omega$. PO is a polarising optic to select input/output polarisations of the fundamental and second harmonic and F is a spectral filter.

2.3.2. Vibrational Sum-Frequency Generation

For its many benefits, SHG presented drawbacks during its development, such as the limited capability to resolve the broad electronic transitions it probed in the visible region. It was theorised that surface-bound species could be better discriminated via their vibrational spectra, though sufficiently sensitive photodetectors in the IR region were not readily available at the time. To resolve this problem, development was stimulated into SFG spectroscopy. In vibrational sum-frequency generation (VSFG) spectroscopy, two input electric fields (laser pulses) are focussed onto a sample surface: one fixed-wavelength beam in the visible region and the other a tuneable IR beam (Figure 2.8). This setup is advantageous as it enables resonant enhancement at vibrational frequencies by scanning the frequency of the IR input but maintains the output in the visible region where detectors are more sensitive.

In SFG measurements, the two incident fields are typically non-collinear, so that the resultant ω_{SFG} signal can be filtered spatially. The reflected angle of the SFG generated in this way is given by analysis of the wavevectors of all three fields:

$$\sqrt{\varepsilon_1(\omega_{SFG})}\,\omega_{SFG}\sin\theta_r^{(\omega_{SFG})} = \sqrt{\varepsilon_1(\omega_1)}\,\omega_1\sin\theta_{i1} + \sqrt{\varepsilon_1(\omega_2)}\,\omega_2\sin\theta_{i2}\ , \qquad (2.60)$$

where θ_{i1} and θ_{i2} are the angles of incidence for the fields of frequency ω_1 and ω_2, respectively.

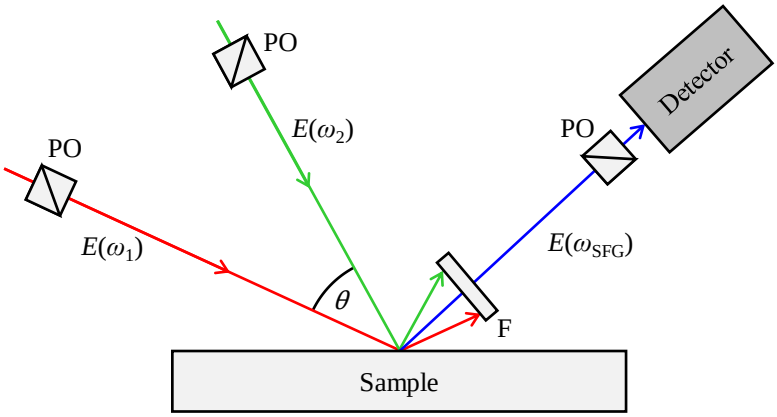

Figure 2.8: Simplified arrangement of optical equipment for a noncollinear, reflection SFG experiment. PO is a polarising optic to select input/output polarisations of the fundamentals and sum frequencies, F is a spectral or spatial filter.

The SFG signal is enhanced near resonances, such as when the tuneable IR frequency comes close to an allowed vibrational transition of a surface.[76] In this way, the vibrational spectra of surface-bound species can be recorded, enabling identification of surface species by their vibrational spectra.[77,78] This has been used in the past to probe systems of interest where other methods have been inadequate, such as in studies on surfactant monolayers[32,79] and revealing the vibrational structure of the liquid water-air surface.[80] An additional benefit of SFG spectroscopy over SHG is its lower sensitivity to bulk nonlocal contributions to the overall nonlinear response, found by comparing reflection and transmission experiments of the same systems.[81,82] Essentially, SFG spectroscopy has the capacity to be a more powerful, or at least more general, surface-specific technique than SHG, albeit at a cost of increased experimental complexity.

2.3.3. Phase Sensitivity

Only a few decades after its first demonstration, direct SFG methods had proven to be a valuable tool in the study of surfaces and interfaces but were limited in the information they could measure. Direct methods are limited to measuring the magnitude of the nonlinear susceptibility, $\left|\chi^{(2)}\right|^2$, and are therefore largely insensitive to the complex nature of $\chi^{(2)}$. The real and imaginary components of $\chi^{(2)}$ can thus be difficult to distinguish without a phase-sensitive method, as illustrated by Figure 2.9, and the relative magnitudes of the components are often necessary to provide accurate information about molecular orientation at a surface.[83]

Moreover, it is the imaginary component of $\chi^{(2)}$ that is often the most informative for the majority of interfacial chemical systems: the imaginary component scales linearly with surface concentration and is related to the absorption of the species generating the nonlinear response. The first phase-sensitive SHG measurements were made as early as 1965,[84] however the technique received little attention at the time, and it was only years later that phase-sensitive SFG measurements became the norm.

2.3.3.1. Phase-Delay Methods

Accurate measurement of $\chi^{(2)}$ phase requires comparison to a reference of a known phase, which can be achieved through interference of the sum-frequency field with another wave the same frequency. The geometry of such interference setups can be either collinear (Figure 2.10) or noncollinear. The phase-sensitive addition generally incorporates a phase-shifting unit (PSU) and reference material into a typical reflection-geometry setup.[85] The PSU serves to change the relative phases of waves passing through it with respect to one another by altering their group velocities,[5] so that when the fundamental fields also induce sum-frequency generation at the reference, the two nonlinear outputs will have different relative phases. Alternatively, the reference may be placed before the sample, so long as the PSU is located between them. The detected signal is then the interference of the nonlinear outputs from the sample and reference. Varying some characteristic of the PSU creates an interference pattern from which the phase of the sample $\chi^{(2)}_{S'}$ can be determined relative to $\chi^{(2)}_{S'}$ of the reference.

In general, fitting of the complex component of the resonant contribution, $\chi^{(2)}_{R}$, from a $\left|\chi^{(2)}\right|^2$ spectrum is unreliable due to the non-unique solutions that can be obtained (Figure 2.9). While the matter is simplified for a handful discrete resonances, many resonances, or continuous resonances, can complicate fitting markedly. Such is the case for the air-water interface, or any liquid where the strength of intermolecular forces varies continuously between neighbouring molecules.[66]

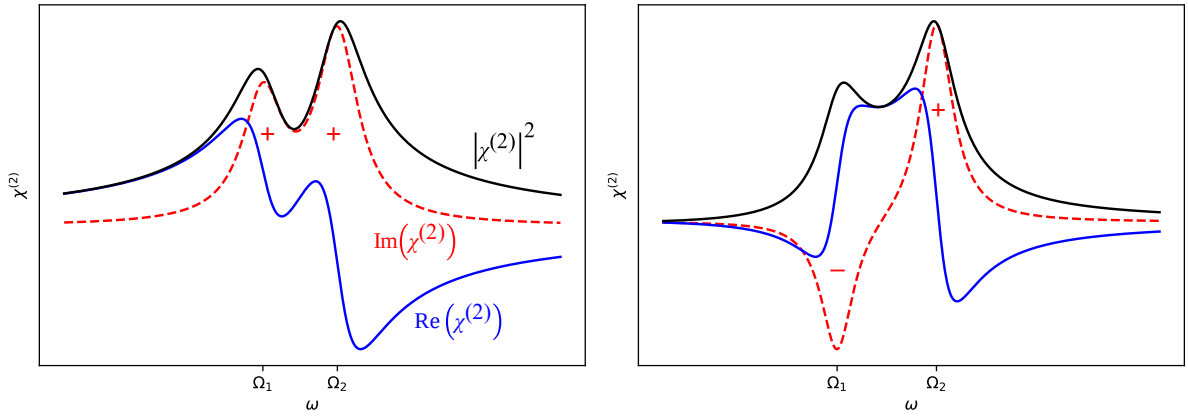

Figure 2.9: Example spectra of overlapping peaks in a $|\chi^{(2)}|^2$ spectrum (black), showing two distinct solutions for similar spectra, where the sign of the imaginary component can be important for interpretation. The real, $\mathrm{Re}(\chi^{(2)})$, and imaginary, $\mathrm{Im}(\chi^{(2)})$, components are shown in blue and red-dashed, respectively.

When a sum-frequency wave is generated from the sample or reference by the fundamentals, both propagating sum-frequency waves have defined phases, ϕ_S and ϕ_{LO}, respectively. The subscript LO when referring to the reference is an acronym for local oscillator (LO) used to describe the interfering wave. The PSU advances the phase of the nonlinear response between the sample and LO by some variable shift $\delta\phi$. The resulting phase of the superposition of the two sum-frequency responses, Φ, is

$$\Phi = \phi_S + \phi_{LO} + \delta\phi \,. \tag{2.61}$$

As the SFG intensity is proportional to $|\chi^{(2)}|^2$, the detected signal is a function of Φ, granting access to information about the surface's phase:[85]

$$|\chi^{(2)}|^2 = |\chi^{(2)}_{S'} + \chi^{(2)}_{LO}|^2 = |\chi^{(2)}_{S'}|^2 + |\chi^{(2)}_{LO}|^2 + 2\chi^{(2)}_{S'}\chi^{(2)}_{LO}\cos\Phi \,. \tag{2.62}$$

The phase of the sample surface can be extracted from (2.61) when $\delta\phi$ tends to zero and ϕ_{LO} is known.[84]

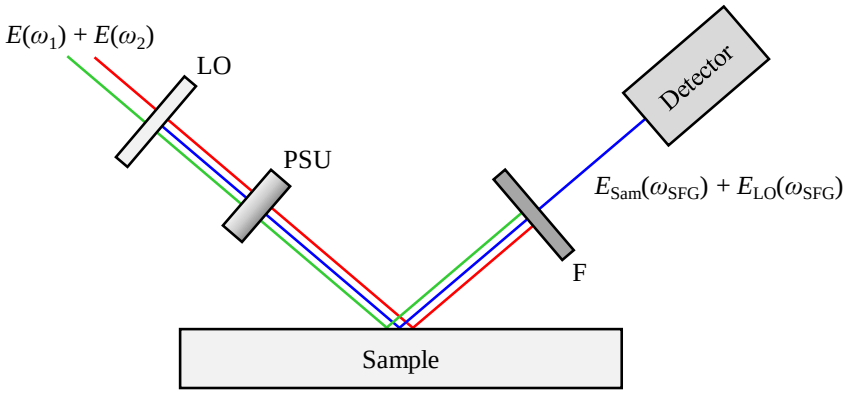

Figure 2.10: Collinear phase-sensitive SFG setup. LO = local oscillator, PSU = phase-shifting unit, F = filter.

When ϕ_{LO} is not known, the sample can be replaced by a reference with known phase ϕ_R, so that the phase of the interference is then $\Phi' = \phi_R + \phi_{LO} + \delta\phi$, and ϕ_S can be found via $\Phi - \Phi'$. Quartz is typically used as a reference due to its high nonresonant bulk signal, as it is noncentrosymmetric, which can be approximated to be real, and the sign of which can be found by piezoelectric measurements.[86] It has been shown that for nonresonant bulk materials, ϕ_S is always 0 or π, depending on the molecular orientation, with a surface of such material advanced in phase by $\pi/2$.[51]

While this method of phase determination is accurate, this method must be repeated for each discrete wavelength across a spectral range of interest, and furthermore at each phase value, which may necessitate long experiment times and high experimental stability. Scanning methods which reduce experiment duration have been employed in the past, but showed reduced accuracy. However, it has been shown that the phase spectrum of a surface can be retrieved by four sequential spectral scans.[66,87] Two of the scans are done by removing the LO to measure $\left|\chi^{(2)}_{S'}\right|^2$ of the sample, and removing the sample to measuring $\left|\chi^{(2)}_{LO}\right|^2$ of the LO. The other two scans utilise both the sample and LO to take two spectral measurements $S_1(\omega_{SFG})$ and $S_2(\omega_{SFG})$ with $\delta\phi$ and $\delta\phi - \pi/2$, respectively. The phase spectrum of the surface is related by the ratios of the signal intensities and the nonlinear susceptibilities:

$$\frac{S_2(\omega_{SFG}) - \left|\chi^{(2)}_{S'}\right|^2 + \left|\chi^{(2)}_{LO}\right|^2}{S_1(\omega_{SFG}) - \left|\chi^{(2)}_{S'}\right|^2 + \left|\chi^{(2)}_{LO}\right|^2} = \tan\left(\phi_S - \phi_R + \delta\phi\right) \tag{2.63}$$

The accuracy of measurements can be improved by additional measurements at a range of $\delta\phi$ values.

2.3.3.2. Multiplex Techniques

Figure 2.11 shows a simplified multiplex SFG setup. Femtosecond fundamental pulses are focussed onto a surface, inducing an ultrafast nonlinear response. A PSU and LO is used as in previously discussed phase-sensitive methods. The SFG pulse generated at the sample surface is delayed in time with respect to that from the LO, in the scheme where the sample is irradiated before the reference. The LO sum-frequency pulse will lead that of the sample by

$$T = d\left(\frac{1}{v_g} - \frac{1}{c}\right) , \tag{2.64}$$

where d is the propagation distance through the PSU and v_g is the group velocity of the sum-frequency in the PSU medium. The total sum-frequency output from the LO at a point $\vec{r}$, $\vec{E}_{tot}(\vec{r}, t)$, will therefore contain two coherent waves with a phase difference, separated in time:

$$\vec{E}_{tot}(\vec{r}, t) = \vec{E}_S(\vec{r}, t - T) + \vec{E}_{LO}(\vec{r}, t) , \tag{2.65}$$

where $\vec{E}_S$ is the time-delayed (typically by a few ps) sample-generated pulse and $\vec{E}_{LO}$ is the pulse generated at the LO. In the frequency domain,

$$\tilde{E}_{tot}(\vec{r}, \omega) = \tilde{E}_S(\vec{r}, \omega)\exp(i\omega T) + \tilde{E}_{LO}(\vec{r}, \omega) . \tag{2.66}$$

Thus, when the SFG response is Fourier transformed, the signal intensity can be used to deduce the real and imaginary components of the surface nonlinear susceptibilities:[88]

$$\left|\chi^{(2)}\right|^2 = \left|\chi^{(2)}_{S'}\right|^2 + \left|\chi^{(2)}_{LO}\right|^2 + \chi^{(2)}_{S'}\chi^{*(2)}_{LO}\exp(i\omega T) + \chi^{*(2)}_{S'}\chi^{(2)}_{LO}\exp(-i\omega T) , \tag{2.67}$$

where the third and fourth terms on the right-hand side give rise to the superimposed interference fringes over the spectrum which contain the phase information. Comparison to an identically obtained spectrum of a reference of known phase enables deduction of the sample surface phase spectrum. The main steps of measurement and analysis are shown in Figure 2.12.

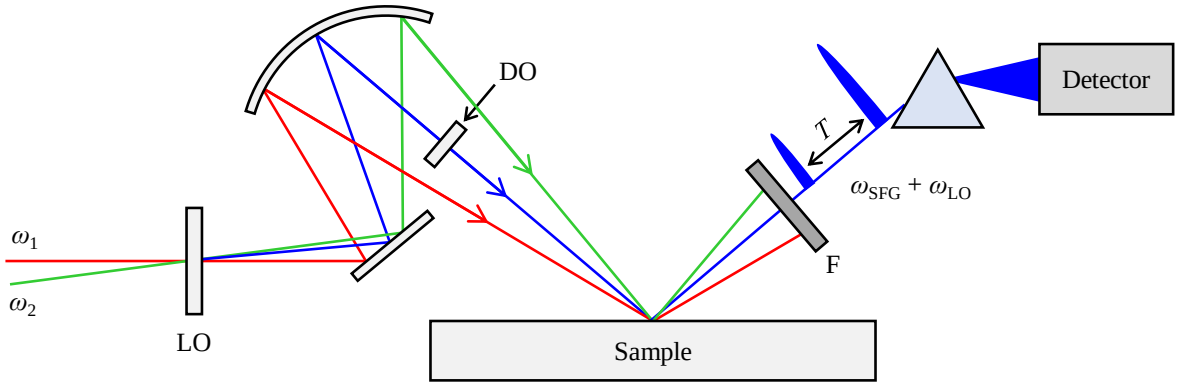

Figure 2.11: Schematic multiplex SFG setup. The superposition of the SFG fields arriving at the detector from the sample and LO are separated in time by *T*. LO = local oscillator, DO = delay optic, F = spatial or spectral filter.

A major benefit of knowing the phase of the SFG response of a surface is the ability to infer absolute molecular orientation. Past studies have successfully achieved phase sensitivity for both SFG and SHG techniques.[65,81] Much attention has been directed at aqueous interfaces with solids and gases, and the use of $\mathrm{Im}(\chi^{(2)}_{S'})$ in determining the orientation of the polar water molecules under different conditions.[89]

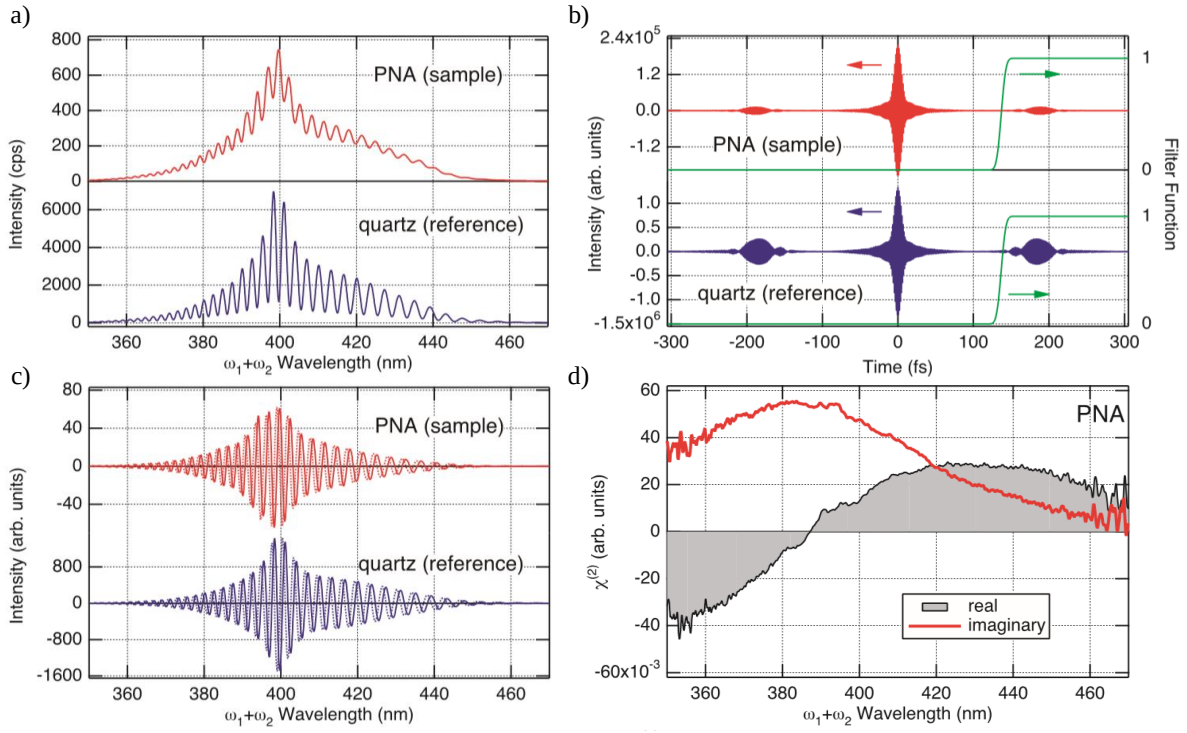

Figure 2.12: Example multiplex analysis for a phase-sensitive SFG method. a) Raw spectrum of I_{tot} for sample (PNA) and reference (quartz). b) Time-domain interferograms obtain by inverse Fourier analysis of a), using a filter function shown in green. c) $E^{(2)}_{S'}E^{*(2)}_{LO}\exp(i\omega T)$ spectrum from Fourier analysis of b), showing real and imaginary components as solid and dotted lines, respectively. d) Complex $\chi^{(2)}$ spectra of PNA monolayer at the air/fused silica interface. Adapted from Figures 1 and 2 from 'Heterodyne-detected electronic sum frequency generation: "Up" versus "down" alignment of interfacial molecules', by S. Yamaguchi and T. Tahara (2008).[88] Reprinted and adapted with permission.

2.3.4. Time-Resolved Surface Measurements

One of the greatest advantages of surface SFG, as with many optical spectroscopies, is its capacity to utilise time-resolution in measurements. Since it is an optical method that probes the electronic response of a medium, time resolution can reveal dynamics down to femtosecond timescales at which electronic motion takes place. Similar to TA spectroscopy, time-resolved surface SFG measurements rely on measuring changes induced by a temporally well-defined event, such as excitation by a laser pulse. Hence, many time-resolved surface measurements also rely on a pump-probe scheme as described earlier, where the pump and fundamental pulses must be spatially overlapped on the surface. The subsequent dynamics can be monitored through a nonlinear response, such as a change in surface SFG intensity, phase or vibrational resonance spectrum.

Measurement of slow processes such as molecular adsorption or desorption and polymerisation on surfaces has been carried out since the 1980s, acting as a first indication of dynamics that could be measured over time.[75,90] Soon after, studies had already shown the ability to probe surface melting processes by SFG on a sub-picosecond timescale.[91] As laser systems continued to improve, surface studies into molecular dynamics began in the 1990s, probing dye molecule relaxation on liquid surfaces, observing rotational dynamics on picosecond timescales.[92–94] These studies showed surface dynamics to be distinctly different from in the bulk for several molecules, with some processes much faster or slower depending on how the species of interest interacted with the surface. Femtosecond dynamics of excited state interfacial solvation were probed soon after, in which processes such as population recovery, orientational relaxation and solvation could each be resolved.[95,96] Via SFG, the relaxation of surface vibrational modes can be probed, and thermalisation of an interface has been observed on an ultrashort timescale. As has been seen in many cases, surface dynamics can differ significantly from their bulk counterparts, driving surface SFG studies towards understanding surface ultrafast dynamics.

3. Experimental

This section describes the layout of optical components used to conduct TA and SFG experiments within this thesis, as well as subsequent post-processing and general data analysis methods. The theoretical background of components or procedures are explored where relevant.

3.1. Laser System

The laser system used to drive TA and SHG experiments is a compact Yb:KGW laser (Light Conversion, CARBIDE CB5).[97] The laser output is centred at approximately 1026 nm, with a maximum output power of 5 W. 1026 nm pulses have a temporal width of approximately 250 fs, a typical spectral full width at half maximum (FWHM) of 8 nm, and maximum energies of ~ 83 µJ pulse^{-1} at 60 kHz. The high repetition rate is beneficial for reducing 1/f noise (pink noise) between laser shots, whereas a high peak power is favourable for SHG experiments where the reflected SHG intensity is proportional to the square of the fundamental intensity. Additionally, high pulse energies allow a significant pump pulse energy to remain even after conversion to the fourth harmonic for TA and SHG excitations. A 1026 nm fundamental output is advantageous for the probing of hydrated electrons, which has been a subject of focus in the Verlet group.[98–100] This way, white light (WL) supercontinua generated for the TA probe cover the region of maximal absorbance of the hydrated electron uninterrupted, without the spectral gap at 800 nm commonly seen in broadband experiments driven by Ti:Sapphire systems.

3.2. Transient Absorption Setup

The TA setup performs time-resolved absorption measurements in bulk solution, forming a clear point of reference for observing changes in interfacial dynamics. The layout of TA components is shown in Figure 3.1.

The initial output of the laser is directed through a half-wave plate (HW0) and variable polarising beam splitter (VBS0), used to select the relative pulse energies supplied to either the SFG or TA experiments. Horizontally polarised components are directed to the TA side, whereas vertically polarised components are received by an optical parametric amplifier (OPA) to drive SFG measurements.

3.2.1. Transient Absorption Pump

The horizontally polarised portion of the fundamental directed to the TA setup passes through HW1 and is split again by VBS1. This time, the horizontally polarised component is transmitted by VBS1 for use in pump harmonic generation, while the vertically polarised component is reflected for probe generation. The horizontal component passes through lenses L1 and L2 to resize the beam, then through a Pockels cell (PC) which rotates the polarisation of a passing light pulse by 90° when a potential difference is applied across its terminals. This was triggered at 30 kHz, with a variable delay from the 60 kHz triggering signal of the laser. Details can be found in the thesis of A. Tyson.[99] The resultant effect of the PC with such triggering was to rotate the polarisation of every second pulse, so that transmitted pulses had alternating horizontal and vertical polarisations. As a result, each transmitted and reflected pulse train after VBS2 contained alternate pulses at 30 kHz intervals. The transmitted horizontally polarised pulses were incident on a retroreflector mounted on a translation stage (TS1), to adjust the pump-probe time delay, *t*, for time-resolved measurements. The beam size was adjusted through a Galilean telescope of lenses L3 and L4 for pump harmonic generation.

The harmonic generation section of the setup allowed conversion of the laser fundamental into second, third or fourth harmonics (513 nm, 342 nm or 257 nm, respectively) for use as pump pulses. In each case, a number of type 1 β-barium borate (BBO) crystals were used for frequency doubling or addition. In the case of the third harmonic specifically, a birefringent calcite plate was used to provide temporal overlap and high conversion efficiency, of the fundamental and second harmonic. All harmonic setups were constructed to have consistent output polarisation (either horizontal or vertical) upon propagation to the sample by use of half-wave plates in their layout. After generation of the harmonics, interchangeable sets of selective mirrors mounted on magnetic bases are used to direct each harmonic to the experimental samples. For TA experiments, the pump was focussed through the sample by a curved mirror, CM1, then dumped afterwards.

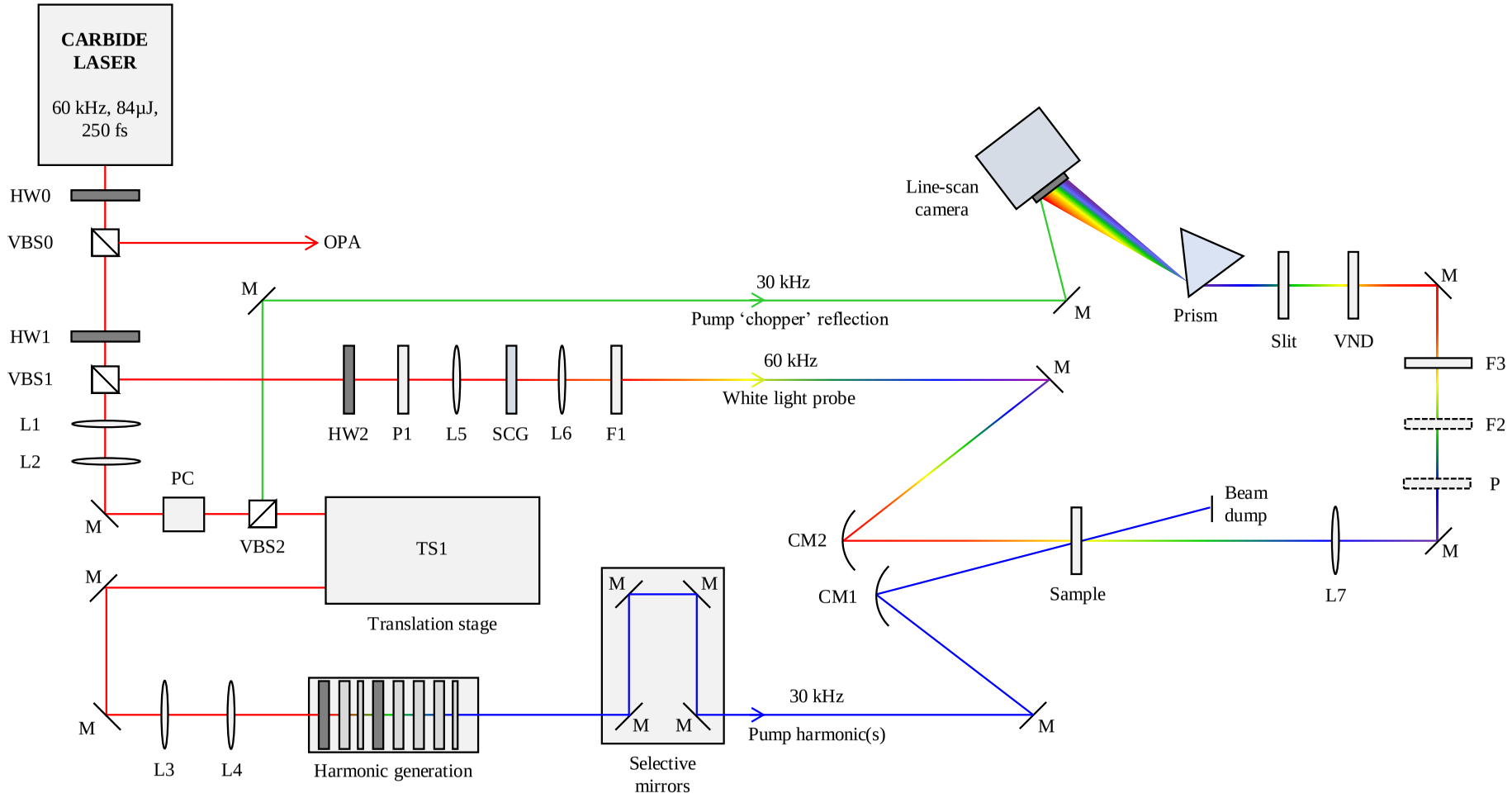

Figure 3.1: Simplified schematic for TA setup. HW = half-wave plate, VBS = variable beam splitter, L = lens, M = mirror, PC = Pockels cell, TS = Translation stage, CM = curved mirror, SCG = supercontinuum generator, F = filter, VND = variable neutral density filter, OPA = optical parametric amplifier, P = polariser.

3.2.2. White Light Probe

The vertically polarised component of the fundamental reflected by VBS1 was used to generate WL supercontinuum pulses for use as a broadband probe. HW2 is used to ensure the pump and probe beams are at the magic angle (~54.7°) with respect to one another, so as to mitigate observed effects of polarisation anisotropy. The WL pulses were generated in a sapphire window, whereby the fundamental was converted into a continuum of frequencies from the infrared to the visible (~1000 – 450 nm). Lenses L5 and L6 were used to focus the fundamental into the sapphire window and to recollimate afterwards, respectively. After WL generation, a shortpass filter, F1 was used to attenuate the unconverted fundamental.

The WL pulses were focussed into the sample by a curved mirror CM2, where they were partly absorbed by either the unpumped or excited sample. Upon leaving the sample, the WL containing the spectral information about the species of interest was recollimated by L7, and the fundamental was further filtered by F3. A variable neutral density filter (VND) was used to modulate the intensity of the WL to avoid overexposure of the camera used for detection. A vertically-orientated adjustable slit was employed to select a narrow, central portion of the beam for dispersal onto a line-scan CCD camera (Imaging Solutions Group, Allegro Orion 2K) by a prism. The slit ensures a better spectral resolution in measurements and for calibration. A typical measured WL supercontinuum is shown in Figure 3.2. The detector was synchronised to the laser to trigger at 60 kHz.

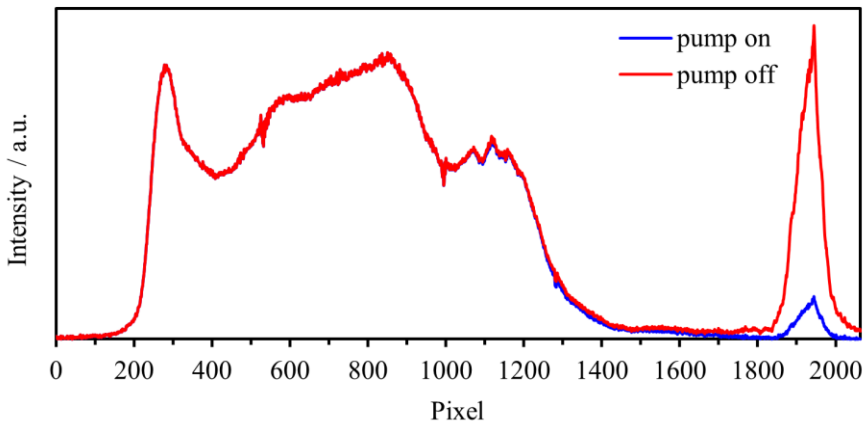

Figure 3.2: Intensity profile of the WL probe generated from sapphire, dispersed onto a line CCD by a prism (pixels ~200-1400), with the chopper reflection used to assign spectra as pump off or pump on (centred approx. pixel ~1950).

For strongly scattering samples, such as proteins,[101] an additional polariser could be placed after the sample in order to minimise scattered pump light from reaching the detector. The polariser could be rotated to minimise the intensity of the scattered light, while also decreasing the intensity of the WL spectrum collected. Due to the varying degree of polarisation across the WL supercontinuum, the polariser affected the detected spectral profile as well as overall intensity. Usually, shorter wavelengths were attenuated more due to their greater degree of depolarisation,[102] which does mean that farther towards the blue edge of the spectrum, the magic angle condition is less well satisfied.

3.2.3. Chopper Reflection

The vertically polarised, reflected fundamental from the PC was directed towards the camera. The beam was attenuated by a neutral density filter and directed through a tightly closed iris to ensure it is incident only on a small area of the detector, and at sufficiently low intensity. The 'chopper' reflection is directed onto the high end of the camera's CCD array, where it acts as a flag to denote if the recorded spectrum is pump-off or pump-on, indicated by the presence or absence of the chopper reflection, respectively (Figure 3.2). The flag is positioned at the high end as it was found that when the camera reads intensity in the direction of increasing pixel number, high intensities on the low end of the array would cause intensity to 'bleed' into the pixels measured afterwards. At the high end, this effect does not affect the area of the camera used for measurements. The chopping is performed at half the repetition rate of the laser, so transient absorption spectra are background-normalised at a rate of 30 kHz using consecutive laser pulses.

3.2.4. Flow Cell

Repeated excitation by the high intensity of the focussed pump and probe pulses can cause photodegradation of a sample solution at the repetition rates used. To lessen sample breakdown, approximately 200 cm^3 of solution was continuously pumped (MarchMay, AC-2CP-MD) through a 1″ detachable flow cell (Harrick, DLC-M25). The cell path length was 0.5 mm, capped with two 0.5 mm calcium fluoride windows to ensure high transmission across the spectral range of the probe and pump harmonics. The focussed pump and probe pulses can cause damage to the flow cell windows over the timescale of an experiment, so the flow cell was translated horizontally across the beam, perpendicular to the direction of laser propagation.

3.2.5. Post-Processing

A raw TA spectrum as obtained above shows change in optical density as a function of pixel number and time, which must be properly calibrated to yield a true DAS as a function of wavelength and time. Specifically, these steps involve background subtraction, wavelength calibration and chirp calibration. The first step is a simple background subtraction of the DAS, made by subtracting a time-averaged spectrum of timesteps up to t_0. This gives a true DAS compared to times before t_0, removing artefacts caused by scattered light.

3.2.5.1. Wavelength Calibration

Calibrating pixel number to wavelength was performed using a filter with characteristic transmission profile (Thorlabs, FGB67, Figure 3.3(a)), as used in other spectrometer designs.[103]

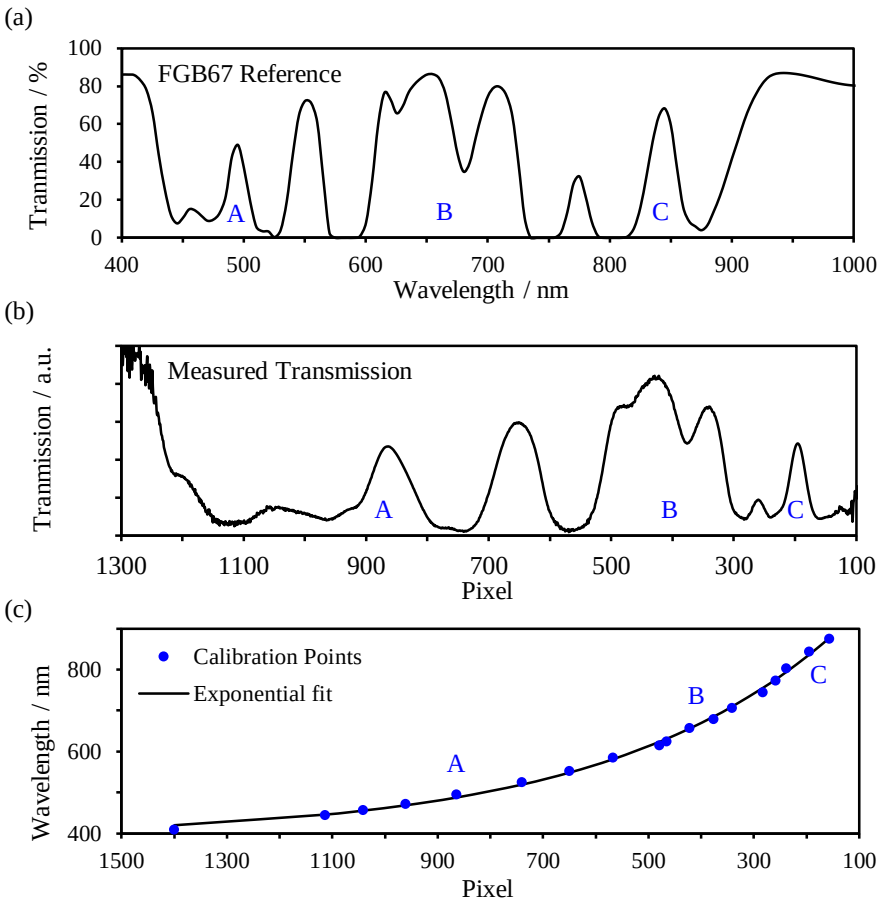

Figure 3.3: Steps used to wavelength-calibrate TA data. (a) Reference filter transmission (FGB67, Thorlabs). (b) Measured transmission spectrum measured in situ, as a function of pixel number. (c) Calibration curve used to transform data, showing the number of features used for calibration, and the fit of a calibration function to the data. A, B, and C label some example spectral features used for assignment.

The filter was selected on account of the high density of transmission features in the spectral range of the WL continuum which gave more points of reference for calibration. A pump-off TA measurement was performed at a single timepoint, both with and without the filter (F2, Figure 3.1) in the path of the WL. A transmission spectrum could then be plotted in terms of pixel number (Figure 3.3(b)). Next, the pixel numbers corresponding to transmission features can be fitted to their corresponding wavelengths of the reference data via an arbitrary, well-fitting function (Figure 3.3(c)). In this case, a function of the form

$$\lambda(p) = Ae^{-B(p)} + \mathrm{C} \ , \tag{3.1}$$

was used, where *A*, *B* and *C* are calibration constants, and *p* is the pixel number. A calibrated WL spectrum obtained using sapphire to generate a supercontinuum is shown in Figure 3.4.

3.2.5.2. Identifying and Aligning t_0

For meaningful analysis of dynamics from TA spectra, t_0 must be accurately assigned to the point at which pump and probe overlap is first achieved. To this end, a compound with strong excited state absorption or emission in the visible region is generally used in place of the sample of interest, for example laser dyes such as fluorescein. The delay stage is scanned end to end and the first instance of signal denotes the approximate position of t_0 at the blue edge of the spectrum (Figure 3.5).

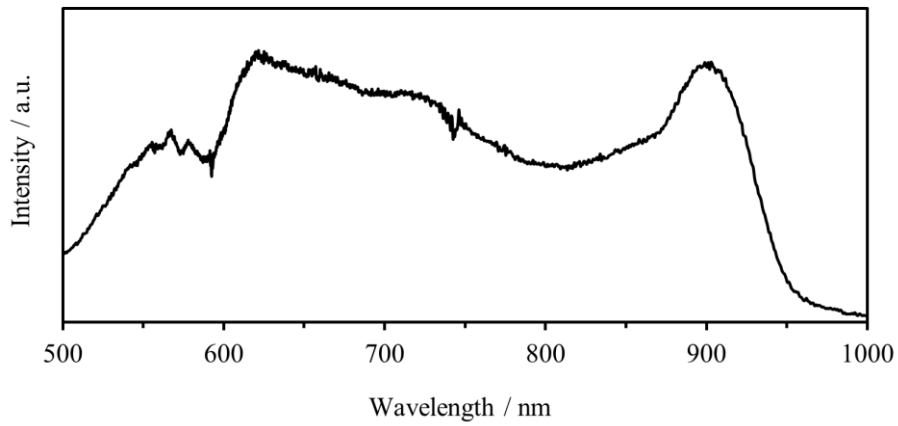

Figure 3.4: Calibrated WL spectrum generated from sapphire seeded by 1026 nm light, showing spectral distribution over the well-calibrated range.

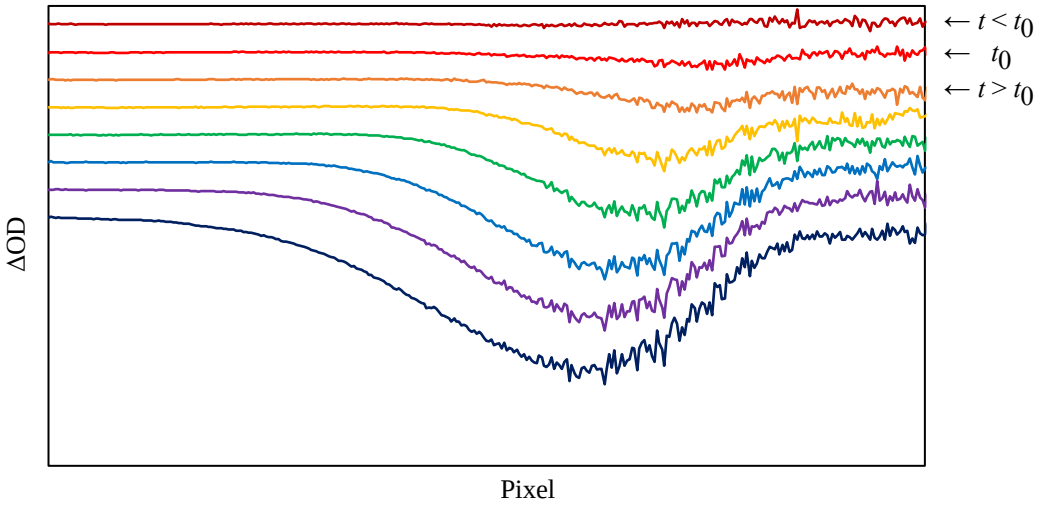

Figure 3.5: TA spectra of fluorescein at early t, showing the onset of stimulated emission used to assign t_0. Spectra are shown with t increasing from top to bottom. All are centred at ΔOD = 0 and have been offset for clarity.

At early times, signal is usually seen to shift across the pixel axis due to group velocity dispersion of the different wavelengths of light, known as chirp. Due to the interchangeable nature of the pump harmonic setup, t_0 must be found for each harmonic separately.

The raw TA spectra appear distorted due to the WL wavelengths interacting with the sample at different times, visible in Figure 3.5 as the early time signal moving across the camera. This arises from group velocity dispersion of the WL wavelengths due to their generation within the supercontinuum medium and propagation to the sample. Rather than use specialised optics to correct for these effects in the physical setup, the choice was made to address these in a post-processing manner so that the setup remains general and readily tuneable.

The chirp was corrected using TA spectra of a neat solvent such as water or methanol, where a nonresonant pump-probe signal is seen at t_0 for each probe wavelength. The nonresonant signal has been attributed to stimulated and impulsive stimulated Raman scattering of the pump and probe.[104,105] The time delays t corresponding to the peak of the nonresonant signal are then plotted as a function of wavelength or pixel, and fitted to t_0 using a second arbitrary correction transform (Figure 3.6(c)), of the form

$$t'(p) = t - \frac{a}{p+b} + c \ , \tag{3.2}$$

where $t'(p)$ is the corrected timesteps for each pixel, and a, b and c are constants.

The chirp is a property of the WL probe and is thus independent of pump wavelength (Figure 3.7). Additionally, as the nonresonant scattering signal was caused by overlap of the pump and probe, it allowed estimation of the time-resolution inherent to the setup, akin to pump-probe cross-correlation. Consequently, the time resolution of a TA measurement from this setup was approximately 200-250 fs.

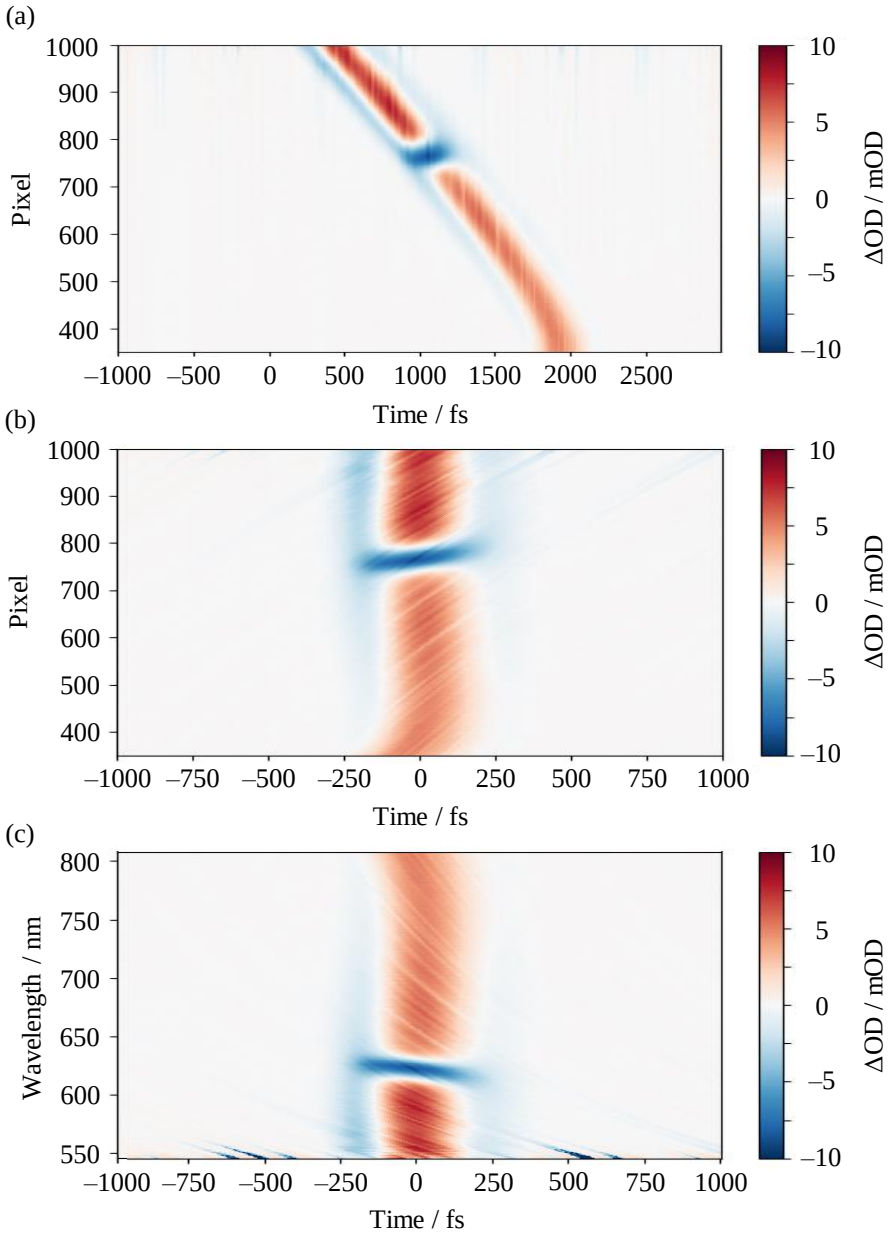

Figure 3.6: Main steps in TA post-processing of DAS for pure water pumped at 515 nm. The narrow band is a signal from nonresonant scattering of the pump and probe. (a) Background-subtracted DAS, (b) chirp correction by alignment of nonresonant scattering band to t_0, (c) wavelength calibration of DAS from pixel to wavelength.

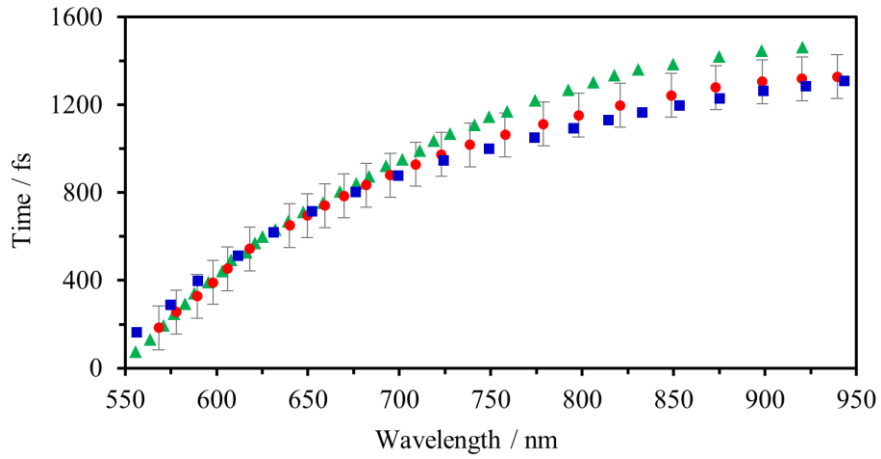

Figure 3.7: Comparison of the form of the chirp of the WL probe at different pump wavelengths, as a function of wavelength. Red circles are data at 515 nm, green triangles at 343 nm and blue squares at 257 nm. Error bars are shown for one dataset only and represent the FWHM of the chirp band.

3.3. Surface Sum-Frequency Generation Setup

Surface-sensitive measurements were made using a newly-developed time-resolved optically Kerr-gated electronic SFG spectroscopy setup.[106] Complementary to the TA, which probes bulk photodynamics through electronic spectroscopy, electronic surface SFG was used to probe interfacial photodynamics.

3.3.1. Sum-Frequency Generation Pump

For SFG experiments, pump harmonics were generated in exactly the same way as for TA measurements, except the chopper reflection was unused, so was blocked. After their generation, the addition of a mirror on a magnetic base was used to divert the beam towards the surface setup. A series of highly reflective mirrors and a periscope guided the pump to a concave focussing mirror (CM3, Figure 3.8) above the SFG sample surface. CM3 was positioned above the focussing mirror for the SFG fundamentals, so that the pump arrived at the surface at an angle of incidence of 63°. The reflected component was blocked above the reflected SFG beam.

3.3.2. Sum-Frequency Generation Fundamental Fields

3.3.2.1. ω_1 – 620-900 nm

The ω_1 field was generated by a commercial 513 nm-pumped OPA (Orpheus, Light Conversion), giving access to wavelengths of 620-1000 nm using the signal output, or 1050-2600 nm using the idler. Typical signal output pulse energies were ~3.8 μJ at 60 kHz. The ω_1 pulses were resized using a plano-convex lens pair (f = 5 cm and 30 cm), resulting in a larger beam diameter (~1 cm) for tighter focussing at the surface. An iris at the focus of the lens pair was used to help remove residual non-signal light from the OPA output. A 550 nm longpass filter was used to remove residual second harmonic used to pump the OPA. A broadband HWP (HW3) was used to select the polarisation of the field arriving at the surface, and a periscope was used to raise the beam above the sample. The top of the periscope used a beamsplitting mirror (reflecting <950 nm and transmitting >950 nm) (DM) to reflect the ω_1 field to a f = 20 cm concave focusing mirror aimed at the surface (CM4). The resulting angle of incidence for the probe beams was 73°. This would have led to some astigmatism at the focus, which was deemed acceptable, but could be compensated for using an off-axis parabolic mirror instead.

3.3.2.2. ω_2 – 1026 nm

The ω_2 field was formed by redirecting the 1026 nm beam used for white-light generation in TA experiments by a removable mirror mounted on a magnetic base, positioned before the sapphire crystal. For SFG experiments the pulse energies used for ω_2 were ~ 4 μJ at 60 kHz. The redirected beam was aligned onto a retro-reflecting pair of mirrors atop a manual delay stage (TS2), followed by another periscope to a height above the sample surface. The ω_2 beam was then transmitted through the beamsplitting mirror DM in the ω_1 line to become collinear with the ω_1 field and was focussed onto the surface in the same way.

Temporal overlap of the SFG fundamentals was found using a BBO crystal above the surface where both beams were collinear. When set to the correct phase-matching angle the relative time delay between ω_1 and ω_2 could be varied using the manual delay stage (TS2) in the ω_2 line. When the two pulses were correctly overlapped, the sum-frequency field could be observed exiting the BBO crystal.

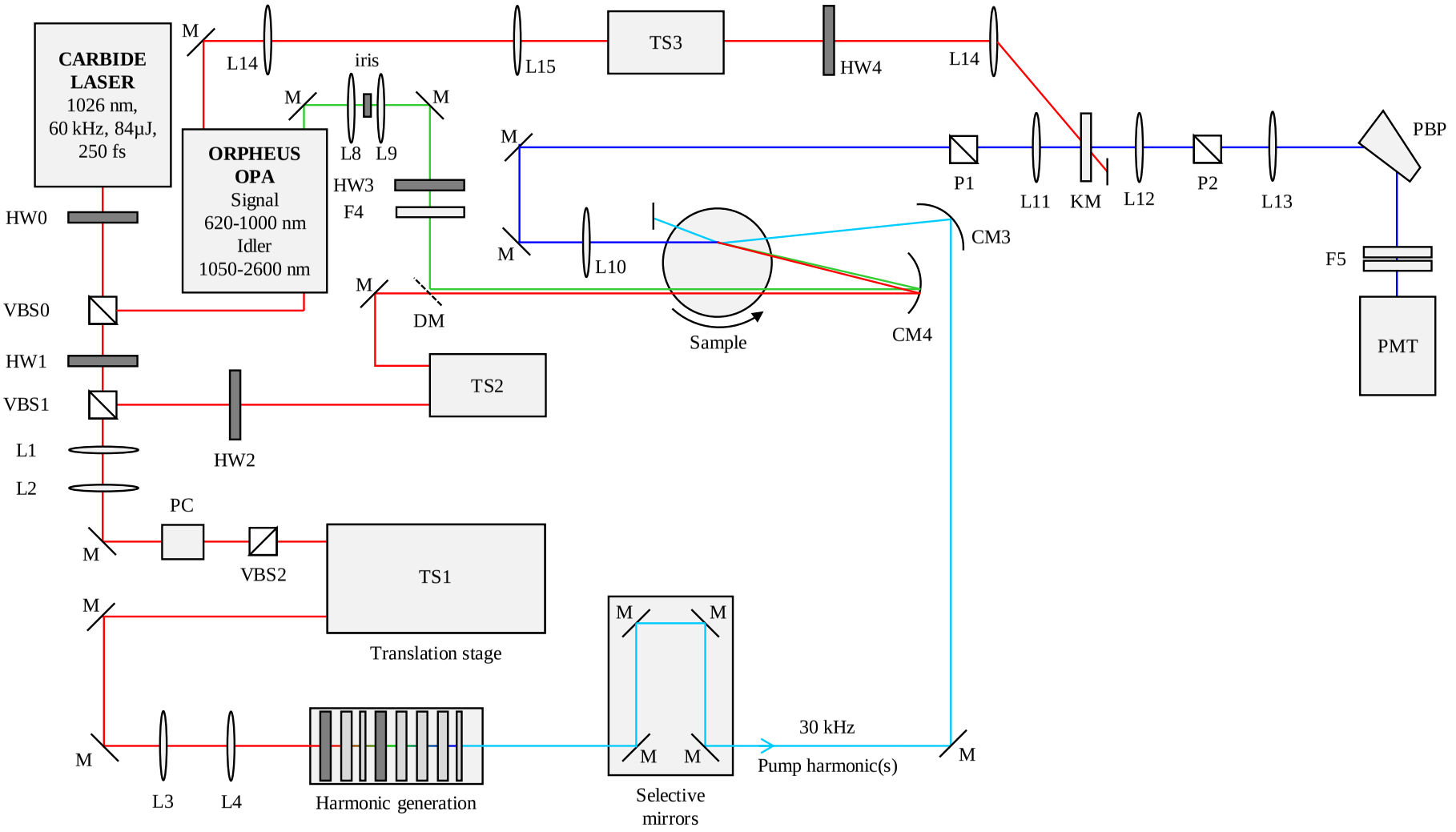

Figure 3.8: Simplified schematic for surface SFG setup. HW = half-wave plate, VBS = variable beam splitter, L = lens, M = mirror, PC = Pockels cell, RR = retroreflector, CM = curved mirror, F = filter, P = polariser, TS = translation stage, DM = dichroic mirror, KM = Kerr medium, PBP = Pellin Broca prism, PMT = photomultiplier tube.

3.3.3. Sample Surface

Samples of approximately 75 ml were contained in a ~12 cm diameter glass dish which was rotated continuously at approximately 0.5 rev s^{-1} to translate fresh sample surface through the beam. The focus of the ω_1 and ω_2 beams was located at the liquid surface, where the spot size of both beams is similar: circular, around 150 μm in diameter. To counter the effects of evaporation, the height of the liquid was kept constant using a home-built liquid height monitor which maintained the liquid surface to within ± 14 μm.[99] This consisted of a low power laser reflected off the liquid surface onto a quadrant photodiode, which produced a voltage signal based on the position of the laser and hence the height of the surface. When the sample surface height dropped due to evaporation, the voltage signal was used to a motorised syringe pump injected solvent back into the sample. Additionally, various implements were used to disrupt the surface flow by lowering them into the solution, to reduce surface bleaching over longer experimental times. An aluminium mesh was first used but was found to be unsuitable in alkaline solutions with sodium hydroxide due to its reaction with the solution. A toothbrush was found effective at reducing sample degradation over longer timescales and was compatible with basic solutions.

Spatial overlap of the ω_1 and ω_2 beams on the liquid surface was performed with the help of a USB microscope camera. Optimisation of overlap was performed by maximising the steady-state SFG signal of a solution of a surface-active compound that provided strong resonant SFG response: malachite green (MG).

After the surface, the reflected component of the SFG and fundamentals passed through an iris to reduce collection of scattered light, as well as fluorescence and white light generated from the bulk. A plane mirror returned the beam to a horizontal plane, where it was recollimated by an f = 20 cm plano-convex lens. After the surface, the ω_1, ω_2 and ω_{SFG} beams were collinear, and initial alignment to the detector was performed on the SFG generated from a BBO crystal before the sample surface.

3.3.4. Pump-Probe Overlap

Pump-probe temporal overlap was performed by locating the SFG of ω_{pump} and ω_2 beams within a BBO crystal located at the approximate position of the sample surface. A removable mirror placed before the sample surface reflected the ω_{pump} and ω_2 beams into a BBO crystal inclined at the (205 = 257 + 1026) nm phase matching angle.

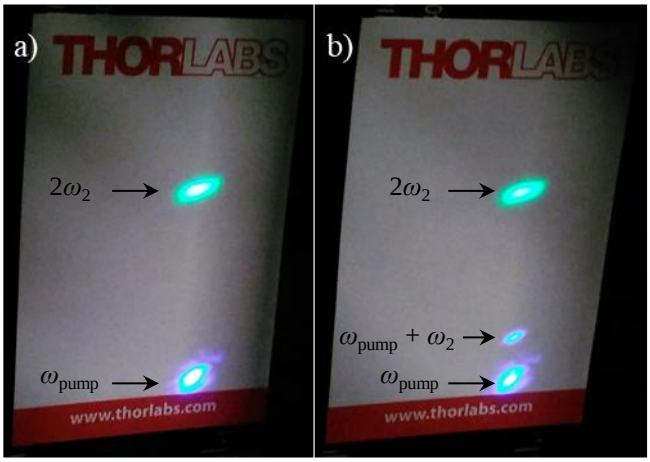

Figure 3.9: a) A BBO crystal placed approximately at the surface with ω_{pump} and ω_2 beams spatially overlapped inside it shows transmission of a 513 nm component from frequency doubling of the ω_2 beam (ω_2 is not visible) and transmission of the 257 nm beam as fluorescence of the paper. b) When ω_{pump} and ω_2 are temporally overlapped an additional spot is visible: 205 nm (generated via 257 + 1026 nm fields).

The pump delay stage could then be scanned to find the position at which SFG is generated between the pump and ω_2, giving an initial estimate of t_0 (Figure 3.9). The 'true' t_0 of the sample surface was found using MG as a model system. The typical shift between the two locations is within 1 ps. Pump-probe spatial overlap was also achieved using a USB microscope to view the surface (Figure 3.10). The pump spot, or the fluorescence caused by the pump spot, is overlapped with the ω_1 and ω_2 spots. Optimisation is achieved using the temporal response of MG.

3.3.5. Optical Kerr Gating

A disadvantage of detecting SFG in the electronic region of the spectrum is that many compounds fluoresce in the spectral region of the SFG probe. Due to the very low nonlinear response of many compounds, even weak fluorescence can dwarf the nonlinear response at the same wavelength. This can make signal detection very difficult, especially for homodyne photon-counting measurements that cannot effectively remove the fluorescence contribution.

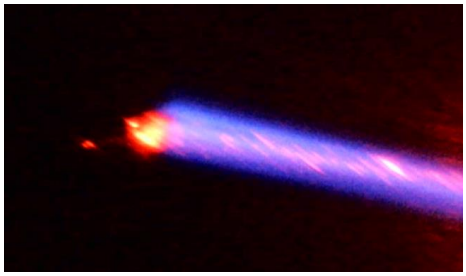

Figure 3.10: USB microscope image of a sample surface with ω_1, ω_2 and ω_{pump} present, showing the spot shape, spatial overlap of the beams and bulk fluorescence caused by the pump.

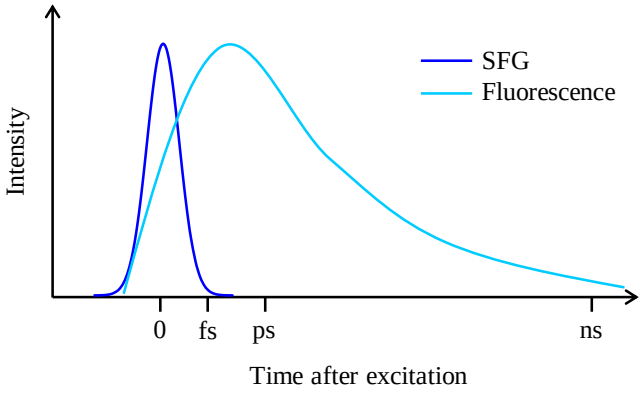

Figure 3.11: Example timescales of surface SFG and bulk fluorescence response from a liquid sample. The relative intensities of the SFG and fluorescence will be dependent on the surface hyperpolarisability and fluorescence quantum yield, respectively.

Selective spectral filtering can help, as may spatial filtering at beam foci, for example, however these were insufficient to resolve the SFG signal from some compounds investigated. Instead, a kind of temporal filtering was used which capitalises on the difference in timescales between the SFG signal and fluorescence responses from a sample.

Whereas fluorescence lifetimes are generally on the nanosecond timescale, the SFG response from a surface is closely related to the cross-correlation of the ω_1 and ω_2 fields (Figure 3.11). For the laser system used here, the resultant SFG pulses are on the order of 200 fs wide. To preserve the SFG light and reject longer-lifetime fluorescence the light at the SFG wavelength can be gated around the SFG signal. This requires a gate that can operate on the femto-picosecond timescale, which excluded the use of mechanical or electrical gates due to their limited response times (typically microseconds or nanoseconds). Instead, we make use of a simple optical gating system with response times on the femto-picosecond regime: optical Kerr gating (OKG). When referring to Kerr gating henceforth, only the optically-induced process will be considered, rather than the electro-optic Kerr effect induced by a voltage.[107,108]

3.3.5.1. Kerr Gating Efficiency

OKG utilises a time-dependent birefringence induced in a material by an optically-delivered electric field, and is shown schematically in Figure 3.12. The desired SFG probe light (along with fluorescence from the bulk) is transmitted through the first of a crossed-polariser pair. Ordinarily, if the KM is non-birefringent, no light would be transmitted from the pair of crossed polarisers. The intense, plane-polarised gate pulse causes an anisotropic change in the refractive index of the KM.

For a gate pulse much longer than the probe, the difference in refractive index parallel, $\delta n_{\parallel}$, and perpendicular, $\delta n_{\perp}$, to the gate polarisation is given by[109,110]

$$\delta n_{\parallel} - \delta n_{\perp} = \lambda K E^2 , \tag{3.3}$$

where λ is the probe wavelength, K is the optical Kerr constant and E is the electric field strength of the gate pulse. This difference in refractive index causes a differential phase change, $\delta\phi$, between probe polarisation components parallel and perpendicular to the gate:

$$\delta\phi = \frac{\pi L}{\lambda} K E^2 , \tag{3.4}$$

where L is the length of the Kerr gating region. The differential phase delay between the two orthogonal components of the probe causes a change in polarisation; the probe's initial linear polarisation becomes elliptical and then circular as $\delta\phi$ increases. For higher values of $\delta\phi$ the probe will be elliptically polarised once again and, when $\delta\phi = \pi$, will regain linear polarisation orthogonal to its original polarisation. In this idealised case, the KM effectively acts as a transient half-wave plate, enabling maximum transmission through the crossed-polariser arrangement. In general, $\delta\phi \neq \pi$, and the transmission, T, of a crossed-polariser Kerr gate varies with

$$T \propto \sin^2\left(\frac{\delta\phi}{2}\right) . \tag{3.5}$$

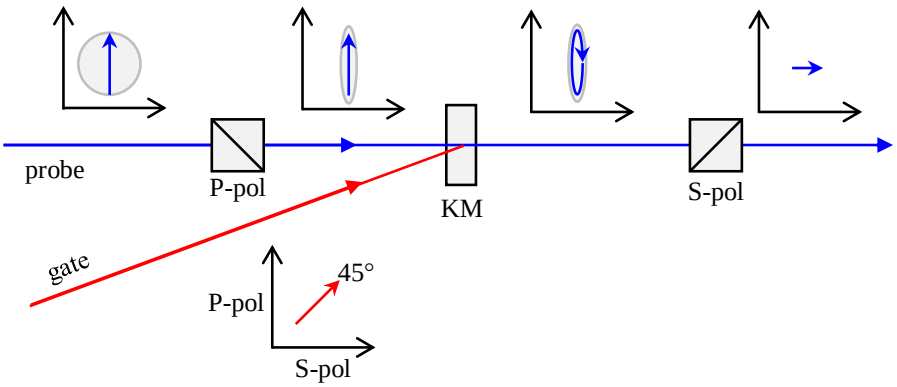

Figure 3.12: In OKG, a gate pulse (red) rotates the polarisation of a probe (blue) within a Kerr medium (KM). Axes represent the polarisation of the fields involved, showing P and S polarisations on the vertical and horizontal axes, respectively. A fluorescence background is shown in grey, isotropically polarised.

3.3.5.2. Gate pulse

The gate pulse is derived from unconverted 1026 nm light used to pump the OPA. Approximately 16 μJ pulse^{-1} is accessed via a secondary emission port from the OPA, which is recollimated as best as possible by a lens pair (both f = 10) and directed towards a series of gold mirrors. The gate beam is reflected off the first at a shallow angle to make multiple passes with one mounted on a manual translation stage, enabling tuneable temporal overlap of the SFG and gate pulses. The gate beam is directed upwards to the level of the OKG arrangement, and through a f = 5 cm plano-convex lens to be focussed within the KM for maximum local intensity. At its focus the gating pulse is approximately 50 μm wide, corresponding to a peak intensity of 30 GW cm^{-2}. The probe and gate beams were in the same horizontal plane, with an angle of approximately 15° between them.

As the gate pulse is focussed to increase the local intensity, the probe must be focussed too so that as much of the probe pulse is transmitted through the gate as possible. In the OKG setup assembled here, the SFG probe is focussed by a plano-convex lens pair (f = 17.5 and 3 cm, respectively) between the polarisers, with the KM at the focus, so that the probe focus area was of a similar size to the gate.

3.3.5.3. Kerr Medium

A range of dielectric materials have been used for Kerr gating, include liquids,[109] liquid crystals, solid glasses and crystalline media.[111] A key property these substances have in common is a high $\chi^{(3)}$, which is closely related to their Kerr constant. A few Kerr media were investigated for use in the surface SFG spectroscopy setup: fused silica, benzene, toluene, nitrobenzene and (111)-cut gadolinium gallium garnet (GGG) (Pi-Kem). Specifically, their gating efficiency and width were measured as a function of time delay, t_g, between the gate and probe pulses at a fixed gate power. In all cases the gate pulses were at 1026 nm, and the probe at 423 nm. Probe light was generated both from a BBO crystal and from a MG sample surface to compare the effects of a high intensity of SFG or a more characteristic intensity of SFG response expected from a surface.

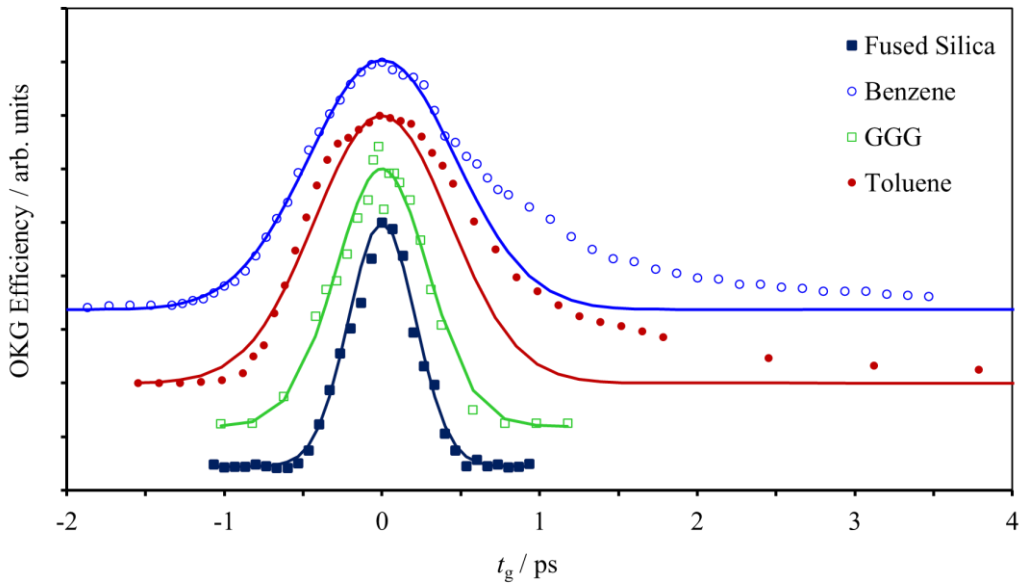

Figure 3.13: OKG response in various materials. Solid lines are Gaussian fits to the rising edge of the gate function. Positive t_g indicates the gate pulse arrives before the probe.

Initially, 1 mm thickness fused silica windows were trialled and successfully showed gating behaviour on SFG from a BBO crystal. The results are shown in Figure 3.13. The gate's temporal profile displayed a FWHM of 500 ± 50 fs at the gating power used. This demonstrated the induced birefringence in fused silica was electronic in nature, resulting in a prompt response of the material, similar to the temporal width of the gating pulse. Note that this was longer than the ~250 fs expected, most likely because of the width of the broadened probed pulse generated in a BBO crystal, but additionally the high gate power may have caused broadening of the material response.[112,113] Temporally, this was advantageous for fluorescence omission, as provided the gate is open for ~250 fs, the SFG should be effectively transmitted with minimal fluorescence. However, the peak efficiency measured was quite poor – on the order of a few percent. For some applications this may be quite acceptable, however considering the low signal levels inherent to SFG spectroscopy, high efficiency was a key feature required for the gating.

GGG was also investigated, as it had been reported to have a higher efficiency at comparably low pump powers.[111] A 5×5×0.5 mm GGG crystal was used for gating tests. At the same pump power, a maximum gating transmission of over 50% was achieved, which was decided acceptable for SFG measurements. The response of the GGG was symmetric and fast, as in fused silica, owing to the similar electronic origin of the birefringence. Gating a signal from BBO showed a FWHM of 690 ± 50 fs, whereas the SFG response from a sample surface was transmitted within 650 ± 50 fs.

Unfortunately, at the gate power required for high efficiency, the GGG was shown to burn over short-term use. More problematically, the burn sites themselves showed a time-independent birefringence that would cause transmission of the probe through the analyser even in absence of the gate. GGG may be a promising material for gating SFG signals if the gate beam is more carefully controlled with respect to its geometry and power. Burning could be reduced by continuous translation of the window if gate-probe overlap could be stably maintained.

To compare solid and liquid media for OKG, the common KMs carbon disulfide and benzene were both considered,[114,115] however benzene was selected first because of its ease of use. A benzene sample was contained in a sealed standard 1 cm fused quartz cuvette between the polarisers. The advantages of benzene as a medium were immediately apparent; testing showed a gating transmission as high as 85-90% and the liquid medium allowed excess heating from the gate pulses to be convected away. Localised boiling occurred within the benzene, but the focus of the gate was offset slightly from that of the probe, ensuring the transmitted beam maintained good stability and shape. In contrast to the solid media, the gating response in benzene showed a visible orientational contribution, evident in the asymmetry of the gating transmission. For $t_g < 0$ (probe arrives before gate), the transmission showed a Gaussian rise, whereas when $t_g > 0$ the trailing edge of the gate shows clear deviation from Gaussian behaviour, seen in Figure 3.13. The asymmetry of the trailing edge was a result of the benzene molecules oriented by the gate pulse relaxing back to an isotropic distribution by rotation, on a longer timescale than the electronic relaxation. For SFG from a nonlinear crystal, the FWHM of a Gaussian fitted to the rise of the transmission profile was 1.0 ± 0.1 ps, whereas from a surface SFG signal it was 470 ± 50 fs, although the latter is based on significantly less data points. Peculiarly, gating from a surface signal shows the gate to be more symmetric, with the broadened tail absent. In reality, the gate width of the former is longer than 1 ps on account of the asymmetric broadening of the training edge, resulting in a true FWHM closer to 1.2 ps.

Over periods of use on the order of several hours, the benzene used as a KM yellowed and developed a fine black particulate, likely resulting from destructive processes where the gate focusses. Both these observations corresponded to a decrease in the efficiency of the OKG of the sample, which must be replaced regularly. Additionally, under high gate intensities the benzene KM showed some kind of emission that spectrally overlaps the SFG. The cause was likely a multiphoton luminescence process, which was visible by eye near the focus of the gate.

This may instead have been supercontinuum generation withing the benzene, however no WL was seen after the KM, and it would be expected that pumping at 1026 nm would lead to significant observable intensity to achieve broadening down to ~400 nm. The light generated withing the KM was difficult to filter before detection, but was reduced to acceptable levels using an additional focus after the Kerr gate: after the KM, the second lens was not used to recollimate the beam, but to create a second tight focus after the analyser, where a pinhole was placed. A third plano-convex lens (f = 20 cm) was used to recollimate the beam before detection. This served to eliminate most of the unwanted light from the gate pulse, typically restricting it to less than 5 detected photon counts per second.

Nitrobenzene was also investigated on account of its large documented Kerr constant, higher than that of benzene.[116,117] Despite a high potential efficiency, the transmission of the nitrobenzene itself at 423 nm was not favourable on account of the yellow colour of the potential sample, which may result from impurities formed over long-term breakdown. At wavelengths above 450-500 nm this may prove a superior material to benzene, or if a freshly prepared and pure sample is used.

Finally, toluene was also used as a gating material. It displayed very similar properties to benzene, exhibiting a gating function with a gaussian rise and asymmetric exponential tail on a similar timescale to benzene. With the geometry and gate power used here, toluene's gate rise was found to have a FWHM of 1.0 ± 0.1 ps for SFG generated from a BBO crystal, and 350 ± 50 fs for SFG signal from an aqueous MG surface. Toluene showed greater long-term stability when subject to the gate pulse intensity and became the favoured material for use in experiments owing to its similar performance and lower toxicity than benzene. Data presented in subsequent chapters was either collected with benzene or toluene as the KM. Distinction has not been made on account of their comparable efficiencies and gating widths.

3.3.6. Detection Scheme

The Kerr-gated light was spectrally filtered around the SFG wavelength with a combination of bandpass filters (typical width 15 nm), and incident on a photomultiplier tube (PMT) (H7732-10, Hamamatsu). The 60 kHz SFG pulses resulted in ~10 ns electrical pulses, which were fed to an amplifier-discriminator (F100-TD) (Advanced Instruments Corp.) producing 50 ns transistor-transistor logic pulses for inputs above 0.75 mV. These were electrically gated so as to reduce pulses from stray photons or thermal noise on the PMT.

The gated pulses were split into two channels by custom electronics, one containing all the pump-on pulses and the other the pump-off ones. Finally, both channels were connected to a USB data acquisition box (USB-6210, National Instruments) configured as a digital edge counter. The counters were read by a LabVIEW program designed to interface with the motorised translation stage for straightforward experimental control. This way, an experiment could probe the SFG photons generated as a function of pump-probe time delay.

3.3.7. Signal Processing

As discussed in Section 2, the number of SFG photon counts, or intensity, is proportional to $|\chi^{(2)}_{S'}|^2$, so to properly access useful information the photon count signal must be square-rooted prior to analysis. Before this, a few steps are required to prepare the data. In theory, the two channels should be exactly equal before t_0, excluding noise. They are not, in fact, due to RF noise from the Pockels cell interfering with the pump-on channel between the PMT and discriminator, and also any fluorescence that makes it through the crossed polarisers. This is accounted for by subtracting the constant offset between the two channels before zero. The pump-on channel can then be normalised against the pump-off channel in a simple division, exploiting the high frequency shot-to-shot background subtraction that the Pockels cell affords the experiment. Once properly normalised, the data can then be square-rooted, resulting in a signal that should be proportional to $\chi^{(2)}_{S'}$ of the sample.

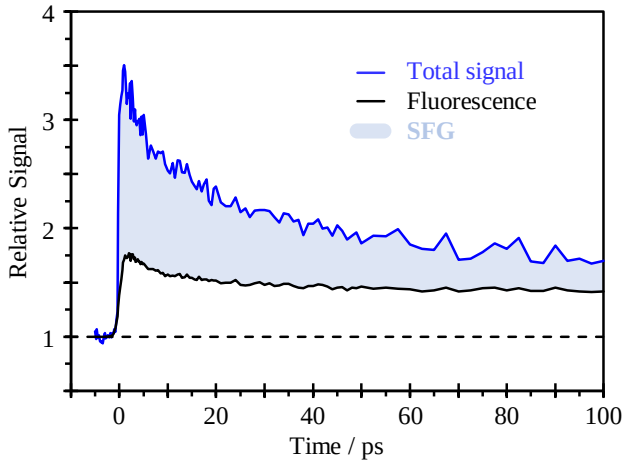

Figure 3.14: Example of a time-resolved, OKG SFG measurement of 150 mM aqueous sodium phenolate, showing the typical size of fluorescence contributions with respect to the SFG signal. The detection wavelength was 423 nm, using fields of 720 nm and 1026 nm for ω_1 and ω_2, respectively, with an ω_{pump} of 257 nm. Data are normalised to the pump-off background.

The raw photon-counted signal of the sample still contained time-resolved fluorescence signal, evident by transients collected in absence of both fundamental beams; although the gate pulse was fixed in time with respect to the SFG from the surface, the pump delay moves relative to both SFG and the gate as *t* was scanned. This means the PMT would see a Kerr-gated fluorescence signal over the course of an experiment too, which could be removed by fitting the signal and subtracting from the pump-on channel (Figure 3.14) before any normalisation. The fluorescence was generally of poor quality due to intentional minimisation and filtering to omit this, but could be used to observe crude fluorescence lifetimes for a bulk system. On the timescales available, this often took the form of a signal rise with an instrument response function (IRF) close to the gate response of the benzene KM (~1 ps) followed by a decay on the picosecond timescale and a large apparent offset which was the decay of the fluorescence on the nanosecond timescale. The 'true' SFG signal was then square rooted to give a quantity proportional to the concentration of surface species of interest which could be fitted to kinetic models and compared to bulk processes via TA spectroscopy.

4. Time-Resolved Optically Kerr-Gated Electronic Sum-Frequency Generation of Malachite Green

4.1. Background

During the development of surface electronic SHG/SFG (ESFG) spectroscopies, dyes were commonly used as model systems on account of their surface-active qualities and large $\chi^{(2)}$ in the optical region of the electromagnetic spectrum.[94,118] Interfacial dynamics, solvation and structure were probed through resonances with their electronic transitions. In particular, malachite green (Figure 4.1(a), MG) has proven a popular compound as a way to benchmark newly developed techniques.[119–121] MG was used here similarly in order to initially explore the feasibility of OKG-ESFG and then to allow comparison to a well-studied system. All data presented here were collected using ~50-100 µM aqueous MG solution (malachite green carbinol hydrochloride, Sigma-Aldrich in high-purity water).

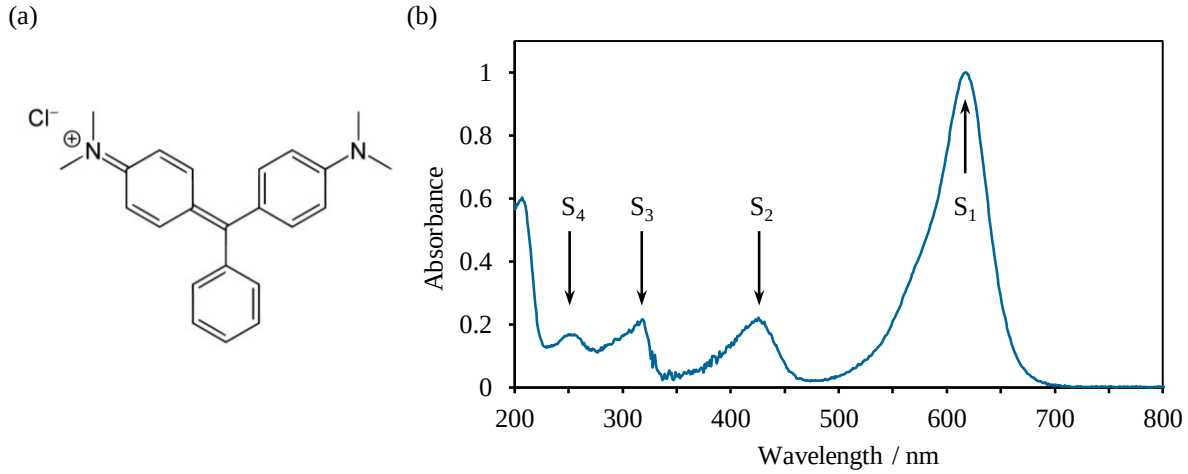

Figure 4.1: (a) Chemical structure of malachite green carbinol hydrochloride (MG). (b) Normalised bulk absorption spectrum of aqueous malachite green. Labels and arrows indicate approximate $S_n \leftarrow S_0$ transitions.

4.2. Time-Resolved Kerr-Gated Measurements

The bulk absorbance spectrum of aqueous MG shows a strong $S_1 \leftarrow S_0$ absorption with a maximum close to 620 nm and a weaker $S_2 \leftarrow S_0$ absorption peaking close to 420 nm. Excitation of MG at 257 nm is resonant with the S_3 and/or S_4 excited state (Figure 4.1(b)) and afterwards, in solution, the molecules relax back to S_0 on a picosecond timescale.[122]

Time-resolved experiments were conducted using two field combinations. One probed the resonance with $S_2 \leftarrow S_0$ only, using fields 720 nm, 1026 nm and 423 nm for ω_1, ω_2 and ω_{SFG}, respectively. The other probed both $S_1 \leftarrow S_0$ and $S_2 \leftarrow S_0$ resonances simultaneously, using fields of 620 nm, 1026 nm and 386 nm. Based on the transition intensities of bulk MG, in the latter configuration it is expected the majority of resonance enhancement results from ω_1 interacting with the $S_1 \leftarrow S_0$ transition. In both cases the nature of the resonances effectively probed the ground state population of surface MG molecules.

4.2.1. ω_{SFG} Resonance Enhancement

The effect of resonance enhancement of the SFG field can be viewed by monitoring the SFG intensity whilst scanning one of the fundamental fields; in this case ω_1. As ω_1 is tuned from 700-950 nm, the SFG wavelength varies from 416-493 nm, respectively, spanning a large portion of the $S_2 \leftarrow S_0$ transition. Wavelengths from 615-700 nm (385-416 nm SFG) could also be generated by the OPA, accessing the $S_1 \leftarrow S_0$ transition.

Figure 4.2 shows the effect of tuning ω_1, and hence ω_{SFG} also, on the field strength of the surface SFG. Tuning of ω_1 resulted in a variation of the SFG intensity, displaying a maximum close to the peak of the $S_2 \leftarrow S_0$ transition. The S_2 peak of the SFG intensity is blue-shifted relative to the bulk by 8 ± 5 nm. The shift is likely a result of the weaker interactions of the polar solvent molecules with the dipole of the S_2 state, resulting in decreased stabilisation of the excited state. The reduced interaction is a product of the incomplete solvation of the MG molecule, and reduced water density at the surface. This behaviour has been seen similarly for the S_1 peak of MG at the water-air aerosol interface, which was observed to blue-shift by 5 nm, via sum-frequency scattering experiments of aqueous aerosols.[121] The smaller S_1 shift may be a result of the different interfacial character/surface curvature of the aerosol environment, or reflect the dipole magnitudes of the two excited states; a higher dipole, as for S_2, may show a larger shift because interactions with solvent molecules will be stronger, hence their absence will show the greatest change.

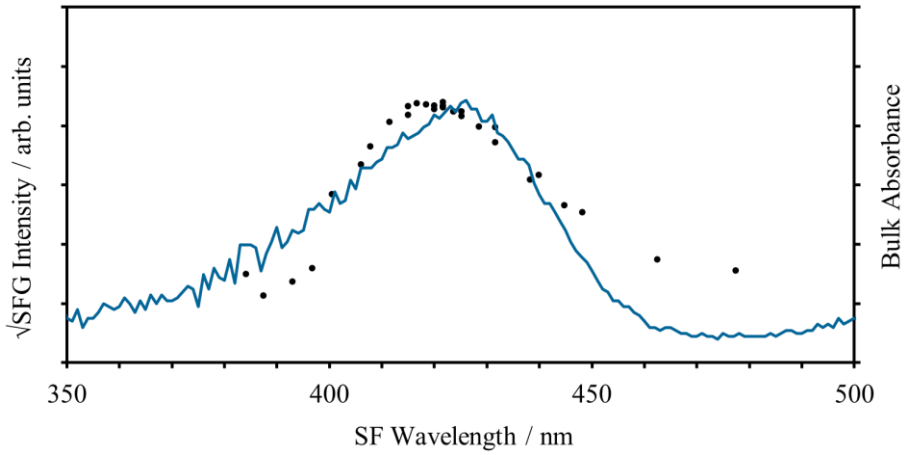

Figure 4.2: Surface (PPP) sum-frequency generation of aqueous malachite green as a function of sum-frequency wavelength (black, points). The bulk absorption spectrum is shown in blue.

The magnitude of the maximum shift observed may also be dependent on the SFG polarisation combination used because of orientation of MG molecules at the surface, though its dependence was not explored here. It is noted, however that the error on the peak position here is large with respect to the observed shift, so without supporting calculations this is somewhat speculative.

At OPA wavelengths of less than 680 nm (SFG below 410 nm) it was expected that a second peak would form due to resonance with the $S_1 \leftarrow S_0$ transition. No obvious evidence of this was seen, even at OPA wavelengths close to 620 nm. The reason behind this is unclear, especially as previous studies have used SHG fundamentals resonant with the $S_1 \leftarrow S_0$ transition to observe the interfacial dynamics of MG.[94] It maybe reflect a narrowing of the S_1 transition band, as has been seen in a sum-frequency scattering experiment study.[121] Alternatively, the double resonance with ω_{SFG} and ω_1 fields may cause some kind of complication with regards to signal interpretation; if the SFG generated from each resonance is out of phase with one another, the SFG may interfere destructively with itself. Unfortunately, due to this setup's insensitivity to the phase of the SFG, this can only be speculated at.

The processed time-resolved, optically Kerr-gated SFG (TR-OKG-SFG) (423 nm; 720 nm, 1026 nm) response of the aqueous MG surface is shown in Figure 4.3, collected in PPP configuration. Before t_0, the signal shows a large resonant background on account of the resonance with the $S_2 \leftarrow S_0$ transition of the surface MG. At t_0 the MG is excited to higher electronic state and a ground state bleach is seen by the reduction of the SFG intensity, which then recovers as the MG relaxes back to the S_0 ground state.

The recovery consists of a few short-lived components on sub-picosecond to picosecond timescales, and a longer component on the order of hundreds of picoseconds. For data collected over the first hundred picoseconds, approximate models consisting of either a bi-exponential decay with no offset, or a mono-exponential decay with a long-term offset were used. For both fits, the model was convoluted with an instrument response function of 250 fs. In the case of the bi-exponential model, components were found to have lifetimes of 11 ± 1 ps and a longer-lived component of close to 600 ps. The longer component has a lifetime much larger than the range over which the dynamics were measured, and when approximated to a constant offset, the mono-exponential model yields a decay lifetime of 15 ± 1 ps.

The surface relaxation is longer than seen in bulk, attributed to the aqueous surface structure providing increased frictional resistance to the internal conversion pathway to the ground state.[94] This effect has been seen at a number of interfaces and in solution, and generally coincides with the viscosity of a solvent or solid surface structure. The lifetimes presented here are also longer than typically observed for isolated MG at a surface, but this may be attributed to aggregation of MG molecules at the surface, which have been found to have longer excited state lifetimes than the monomeric form.[122] The surface activity of MG results in a high interfacial concentration, increasing the prevalence of aggregates, which have been shown to impact surface measurements even at low bulk concentrations.[123] The blue-shift in the observed PPP spectrum of the MG interface may also result from contribution from aggregates, which have been observed to have blue-shifted features.[124]

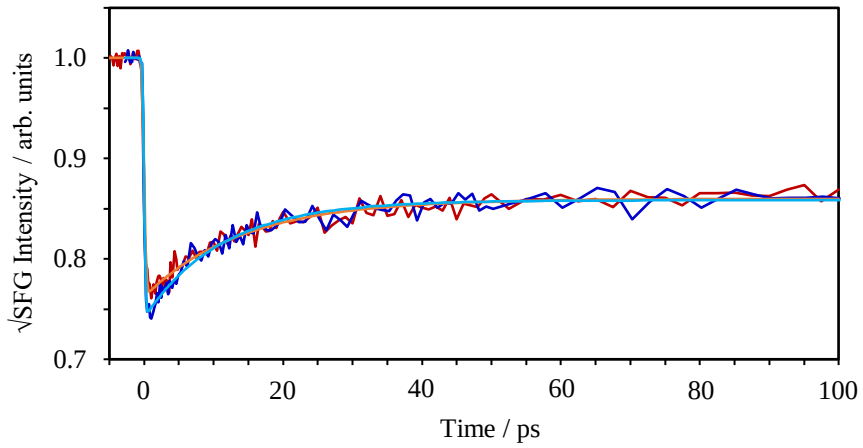

Figure 4.3: Time-resolved surface (PPP) SFG signal of aqueous MG with (blue) and without (red) OKG. Fitted models are shown in light blue and orange, respectively.

It was necessary to confirm the OKG setup did not affect observation of the dynamics and, therefore, it was compared to an identical experiment with the gate permanently open (polarisers set parallel to one another, with the gate pulse removed). The observed signals were highly consistent within their error, supportive for the gating not perturbing observed signals (Figure 4.3). When fitted the same way, a biexponential model gave lifetimes of 10 ± 1 ps and approximately 900 ps, whereas a monoexponential decay gave a lifetime of 12 ± 1 ps.

To further probe the effectiveness of the OKG for surface SFG signals, a strong fluorophore was added to the bulk solution: coumarin 2 (coumarin 450). Coumarin 2 fluoresces strongly in the region 400-500 nm, overlapping the detected wavelength region. Even at low pump intensities and with a small concentration of coumarin, the pump-on photon counting channel was completely saturated, such that no transient signal could be observed. With the gating in place, a transient signal was observed, reflecting the depletion of the ground state MG at the surface (Figure 4.4). The signal was generally poor, partly as the pump beam was low intensity to reduce saturation of the ungated signal for comparison, but shows that surface SFG signal could still be probed even in the presence of overwhelming bulk fluorescence. Moreover, it is important to note that a negative change was seen even when a positive contribution would be expected from the time-resolved fluorescence profile, which should be accounted for before interpreting any surface dynamics. Fluorescence contributions will be covered in more detail in chapter 5. Having implemented the OKG of the SFG probe and tested its impact on the observed signals, the TR-OKG-ESFG setup was to be used to investigate compounds of interest, for example some experiments trialled before its development that were unsuccessful because of bulk fluorescence.

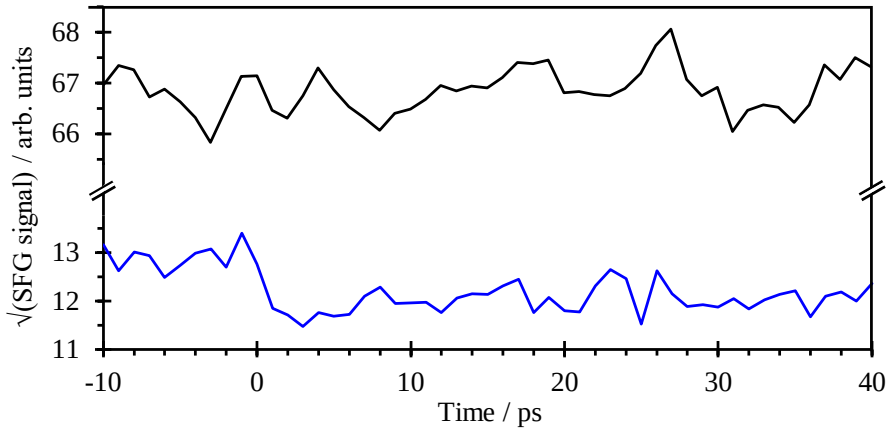

Figure 4.4: Time-resolved surface (PPP) SFG signal of aqueous MG with added coumarin 2 in ethanol, with OKG (blue) and without OKG (black).

4.2.2. ω_1 Resonance Enhancement

Over the course of the development of the TR-OKG-ESFG setup's development, some other experiments were performed on MG to test what experiments were feasible with the laser system and setup configuration, which are presented here and in section 4.3. A second experiment probed both $S_1 \leftarrow S_0$ and $S_2 \leftarrow S_0$ using 387 nm, 620 nm and1026 nm. As both resonances probe transitions originating from the ground state, it was expected a similar SFG signal would be seen as in 4.2.1, with the majority of signal originating from resonance with the lowest excited state. The results of a TR-OKG-ESFG experiment (386 nm; 620 nm, 1026 nm) are shown in Figure 4.5. Overall, the dynamics are very similar to those recorded at 720 nm (Figure 4.3), displaying a resonant background, followed by a bleaching and recovery on similar timescales. When compared to the corresponding gated transients at ω_1 = 720 nm, analysis of the shorter wavelength signal using a biexponential model resulted in lifetimes of 7.8 ± 0.9 ps and a longer component of approximately 200 ps. A monoexponential model gave a longer lifetime of 16.5 ± 0.9 ps. The data at 620 nm also shows a greater recovery of the signal bleach.

The difference in timescales may reflect cooling dynamics upon excitation/relaxation, with different SFG wavelengths probing slightly different geometries on the ground state after relaxation of the excited molecules. This would most likely manifest as a shifting of the peak wavelength of the ground state bleach, however this is not readily observable with the narrowband probe used here. Either a number of transient SFG spectra at different wavelengths could be recorded and compared, or use of a broadband probe, as in typical VSFG measurements, could be exploited to view spectral changes too. This would also have the additional benefit of revealing the effects of any additional transients that may be contributing to the observed $\left|\chi^{(2)}\right|^2$ measured. The changes in dynamics between the two probe fields may also be attributed to differences in sample concentrations or pump energies, neither of which were carefully controlled between these measurements. In the case of concentration, the degree of aggregation has been shown to strongly affect the relaxation timescales observed.[122]

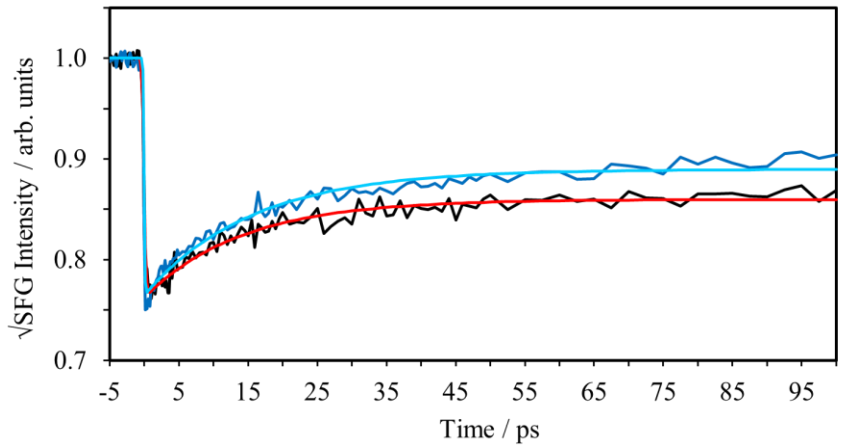

Figure 4.5: Time-resolved surface (PPP) SFG signal of aqueous MG with ω_1 = 620 nm (blue) and with ω_1 = 720 nm (black), normalised with respect to the fitting on one another. Fitted models are shown in light blue and red, respectively. Data presented are for ungated measurements.

4.3. Static Surface Polarisation/Orientation

As mentioned in section 2.2.2, an advantageous feature of SFG is its ability to infer orientation of a molecule at an interface.[43] When observing a resonantly-enhanced signal, the orientation of the TDM responsible for the resonance can be inferred with respect to the lab frame, as was done for MG here to explore this approach. The determination can be simplified for phase-resolved measurements, however a number of studies have utilised homodyne, or direct, methods for orientational analysis.[125–127]

By selectively choosing input and output polarisations of the incident and sum-frequency fields, different terms in $\chi^{(2)}$ can be probed. $\chi^{(2)}$ can be related to the molecular coordinate system via a transform, which contains the orientational information. This approach requires knowledge of the adsorbed molecules' β with respect to the molecular coordinate system. For long rod-like molecules, β is usually dominated by a single axial component along the primary molecular axis, and although MG does not fit such a physical description, this approach will be assumed here; with the field combination chosen as in section 4.2.1, $\beta(\omega_{SFG}; \omega_1, \omega_2)$, will be dominated by a component parallel to the TDM of the $S_2 \leftarrow S_0$ transition, which is assumed to be in the plane of the molecule.

Hence, the average tilt angle, ϕ, of MG at the aqueous/air interface with respect to the surface normal can be found using the following:[128,129]

$$\frac{2\chi^{(2)}_{xzx}}{\chi^{(2)}_{zzz}+2\chi^{(2)}_{zxx}} = \frac{1}{2}(1-\cos^2\phi)\,, \tag{4.1}$$

where the surface normal is parallel to z. This has been determined under the assumptions that the component of β parallel to the TDM dominates over the other contributions and there is a sharp distribution of tilt angles, for example a delta function, $\delta(\phi)$. The effective susceptibilities can be found experimentally by measuring the SFG intensity at their assigned polarisation combinations and using (2.56) along with the appropriate Fresnel factor for each field.

4.3.1. Malachite Green Surface Tilt Angle

The SFG intensity from an aqueous/air surface of approximately 100 µM MG was measured in various polarisation combinations, shown in Figure 4.6. Polarisations were selected using a HWP in each of the input fields, and a single Glan-laser polariser (P1) in the SFG path. Polarisers were not used in the path of the fundamental fields, as they were observed to be well-polarised. The SFG signal was viewed on an oscilloscope as the PMT output voltage, which was linearly proportional to the SFG intensity at the gain and intensity range used.

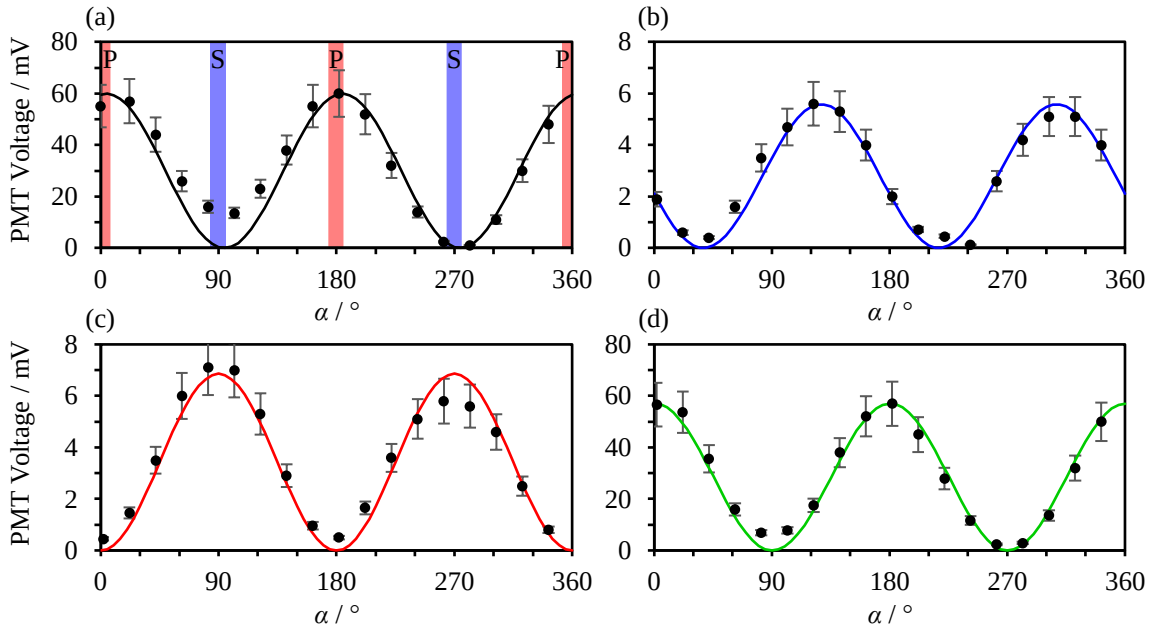

Figure 4.6: Surface SFG intensity as a function of polariser P1 angle, α, collected from a MG sample surface. (a) αPP, (b) αSP, (c) αPS and (d) αSS polarisation configurations. α = P (0°) or S (90°) shown for one panel only, as red or blue shaded regions, respectively.

Table 4.1: Parameters used in determination of MG tilt angle.

ω_n	λ_n / nm	$n_1(\omega_n)$	$n_2(\omega_n)$	$n'(\omega_n)$	$L_{xx}(\omega_n)$	$L_{zz}(\omega_n)$
ω_{SFG}	423	1.0003	1.3381	1.1521	1.2719	0.4069
ω_1	720	1.0003	1.3302	1.1488	1.2718	0.4118
ω_2	1026	1.0003	1.3266	1.1473	1.2717	0.4141

The SFG signals in Figure 4.6 show a clear $\sin^2(\alpha)$ dependence, indicating the SFG was dominated by a single component for each polarisation combination. Asymmetry in the plots was a product of the rotation of Glan polariser used to analyse the SFG due to imperfect alignment. The full range of the plots also shows the symmetry allowed and forbidden combinations corresponding to the maxima and minima, with the largest SFG signals generated by PPP and PSS polarisations. Values obtained for the allowed polarisation configurations were used, along with the Fresnel factors in Table 4.1, to deduce the tilt angle of the MG with respect to the surface normal.

The refractive index of the interfacial layer, n', is typically difficult to measure, and has a large effect on the tilt angle value calculated. It is usually taken to be the refractive index of the bulk phase, for an aqueous/air interface, or the average of n_1 and n_2. Alternatively, n' can be estimated via a modified Lorentz model,[129] giving approximately $n' = 1.15$ for an air/water interface, though may be slightly higher due to the presence of hydrocarbons at the interface.

The data above yield a tilt angle of $\phi = 25 \pm 8$ ° for MG at the aqueous/air interface. This is smaller than the ~40° angle found in previous studies doubly resonant with S_1 and S_3,[94] though this more upright orientation may be adopted due to a higher surface concentration used here. The effect of concentration on the broadening of the distribution of ϕ is also unclear, and it has been noted that assuming sharp distributions where this is not the case can cause the determined value of ϕ to tend towards an erroneous value.[130] The effect of surface concentration on the orientation of MG could be probed by varying the bulk concentration, for example.

4.4. Conclusions

The work presented here has demonstrated the principle and application of a TR-OKG-ESFG spectroscopy experiment by observing the ultrafast dynamics of MG at the air/water interface. It has been shown that by optically Kerr-gating the SFG signal from a sample surface, a large fluorescence signal from the bulk can be effectively suppressed by orders of magnitude. Importantly, too, it has been shown that the dynamics observed are unaffected by Kerr-gating the detected signal. This detection technique may enable access to pertinent interfacial systems by TR-SFG spectroscopy that were previously difficult to observe due to emission ranges that overlap detection wavelengths.

The Kerr gating has been used in conjunction with a homodyne-detected ESFG arrangement, however its application is in principle quite general, and could be modified in a number of ways. For example, unlike most fluorescence upconversion techniques, OKG is broadband, so long as the dispersion within the KM is small enough to keep temporal overlap between the gate and probe. While broadband fluorescence up-conversion techniques have been developed, these are generally limited to spectral widths of a few hundred nanometres in the visible.[131,132] This enables the extension of OKG to broadband ESHG and ESFG setups as long as the KM is transparent across the spectral range. Phase-sensitive ESFG setups using either spatial interference or phase-delay methods that would transmit through the KM simultaneously would also be compatible, though multiplex methods where the sample and LO interfere from temporally-separated pulses may not be compatible; the gate can be made longer at the expense of greater fluorescence admission, however the gate probe and LO may experience different phase contributions within the KM if the refractive index evolves between the two pulses.

The Kerr medium can be chosen to favour either temporal resolution (fluorescence rejection) or signal transmission efficiency depending on the ratio of SFG signal to the bulk fluorescence. A more sophisticated gating arrangement, such as moving to a collinear gating geometry, or use of off-axis parabolic mirrors for cleaner focussing would improve the general implementation. Additionally, use of a well-collimated properly-shaped gate pulse, rather than an unconverted OPA residual, would likely improve the setup further by improving the spatial quality of the gate at the focus. However, the arrangement presented here does serve as a good example of how this can be incorporated into existing setups with minimal disruption or rearrangement of optical components.

Examples of different resonance regimes have been explored briefly, probing ultrafast dynamics of MG using either ω_{SFG} resonant with $S_2 \leftarrow S_0$, or ω_1 resonant with $S_1 \leftarrow S_0$. As both resonances essentially probed the ground state population, similar dynamics were seen in both cases, with differences attributed variations in sample preparation or pump power. Orientation of MG molecules at the aqueous/air surface has also been probed as an example of the depth of information that SFG spectroscopy can access from interfacial systems.

Having developed and demonstrated a TR-OKG-ESFG setup using a model compound, the next chapter presents the use of this technique to probe new information of an interfacial system of current interest.

5. Phenolate Photo-Oxidation at the Aqueous/Air Interface

5.1. Background

Several scientific studies of the Verlet group have focussed on solvated electrons, either in solution,[98] in water clusters,[133] or at aqueous interfaces.[100,134] Solvated electrons play an important role in several areas of chemistry including catalysis, redox reactions, biochemical processes and electrochemistry. They represent the most basic solvated anion: a solvated negative charge with no nuclear structure. To this end, their importance is fundamental in the study of solvation and electron transfer in the condensed phase, with a number of studies dedicated to their generation in various solvents from a range of compounds.[135–139] Popular such compounds include simple inorganic salts or aromatic molecules, such as phenol and its anion, phenolate, which are components of chromophores in a number of natural systems.[140–142]

Phenol has been well-studied in the gas and condensed phases on account of its photochemistry. UV excitation of phenol at 267 nm in the gas phase or in aqueous solution results in electron ejection on a nanosecond timescale:[143,144]

$$\mathrm{PhOH} \xrightarrow{267\ \mathrm{nm}} \mathrm{PhO}\cdot + \mathrm{H}^+ + \mathrm{e}^- \ , \qquad (5.1)$$

where, in solution, the electron goes on to be solvated as $\mathrm{e}^-_{(aq)}$.

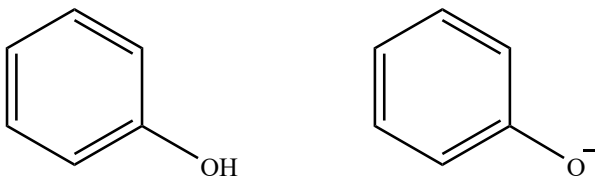

Figure 5.1: Chemical structure of phenol (left) and phenolate (right).

The mechanism of this photodetachment is thought to occur via excitation into the $\pi\pi^*$ S_1 state of phenol, followed by access to a dissociative $\pi\sigma^*$ state, resulting in loss of an electron as well as a proton. Phenol has been shown to eject an electron on much shorter timescales at higher excitation energy, highlighting the involvement of energy-dependent pathways.[143]

Alternatively, photo-oxidation of phenol's anionic form at the same wavelength occurs on a picosecond timescale:[98,145]

$$PhO^- \xrightarrow{267\ nm} PhO\cdot + e^-_{aq} \quad . \tag{5.2}$$

Here, in the absence of a $\pi\sigma^*$ state, the excited phenolate ejects an electron promptly after a $\pi\pi^*$ transition. The mechanism in (5.2) has been shown to be wavelength-dependent, ascribed to electron tunnelling to facilitate charge separation,[98] or contribution from partial excitation of S_2, with different subsequent dynamics.[146] The photo-oxidation dynamics of phenolate show similarities to charge-transfer-to-solvent (CTTS) transitions[147] of aqueous halides as observed via the ejected electrons; following charge separation, the electron exists in an incompletely-solvated form in close proximity to the parent radical that either geminately recombines, or escapes the parent to become fully solvated at a greater separation distance. In the case of CTTS transitions, the distance of prompt ejection scales with the excitation energy.[148]

The phenolate anion is of key interest here not only because of its bulk dynamics, but also owing to the significant differences seen in its photochemistry at aqueous surfaces. A time-resolved surface heterodyne-detected VSFG study claimed that at the aqueous-air interface the photo-oxidation of phenol proceeds 10^4 times faster: observing electron loss from phenol within 100 fs.[149] The experiment probed the vibrational spectra of the aqueous interface in the O-H stretching region, enabling observation of the solvent, as well as the phenol O-H moiety. The phase-sensitive nature of the setup allowed the $\mathrm{Im}(\chi^{(2)})$ spectrum to be monitored separately and allowed spectral features to be assigned based on previous studies. After UV excitation, the surface vibrational spectrum exhibited ultrafast changes that were grouped into three components, all appearing within 100 fs of excitation (the time resolution of the measurements). A signal attributed to the hydrated electron, based on previous work by the same group,[150] was seen to decay within 300 fs: orders of magnitude faster than seen in bulk measurements by TA.[98,143,148]

A transient with a time constant of 80 ps was ascribed to the proton lost from the phenol molecule, in reasonable agreement with estimated proton diffusion,[151] and a long-lived transient was assigned to the phenoxyl radical that remains solvated at the surface for over 300 ps. The rapid disappearance of the electron from the spectra was thought to capture the surface electron diffusing away from the interface towards the bulk and out of the probing depth of the experiment, and was noted to be faster than the theoretically-predicted electron diffusion rates.[152] A following study supported the spectral interpretation with theoretical calculations predicting the observed increase in photo-oxidation.[153] However, in the VSFG study, the effect of resonance of the ω_{SFG} field with the optical absorption of the electron was never discussed, which may have implications across the entirety of the probe range that was used.

The above VSFG analysis relies on deconvoluting the recorded $\Delta Im(\chi^{(2)})$ spectra in a similar manner as a TA experiment while probing for products in a spectral region where many chemical species will elicit an O-H stretch response. Most species that disrupt the surface structure of pure water will cause a change, thus it may not be trivial to properly assign transients if the O-H stretch region is not specific enough. This also relies on the dynamics of the solvent adequately, and promptly, describing the kinetics of the photoproducts. With these factors in mind, it was believed a more transparent approach would be to monitor the surface photoproducts *directly* via surface ESFG spectroscopy, rather than VSFG.

The planned experiment aimed to study photodetachment of the electron from phenol or phenolate at the aqueous-air interface. The fields used would be (423 nm; 720 nm, 1026 nm): resonant with the hydrated or pre-hydrated electron with 720 nm and 1026 nm fields, respectively. The 720nm field is close to the peak of the hydrated electron's absorption spectrum, corresponding to its p ← s transitions.[154,155] Phenol/phenolate shows no bulk absorption towards the visible and the phenoxyl radical absorption is nearer 400 nm,[145,156,157] hopefully preventing the probing of overlapping surface spectral features if they did not shift much relative to the bulk. In the case of phenol, it has been shown that at high concentrations, as would be found at the surface, UV excitation gives rise to excimer absorption peaking near 600 nm,[158] which may be present at the surface, even at pH values of up to 12 due to the modified pK_a of phenol at the aqueous/air interface.[159]

Initial attempts showed homodyne detection in the near UV-visible regime came with an inherent problem: fluorescence from the bulk phenolate as a result of 257 nm pump excitation, which overlapped the 423 nm probe region. This was especially problematic for the sensitive detection using photon counting.

The modified TR-OKG-ESFG technique in section 3.3 was developed that then enabled measurement of the SFG from the surface even in the presence of fluorescence from the bulk sample.[106]

5.2. Results

5.2.1. Transient Absorption

To form a logical point of reference for surface data, bulk dynamics were studied using TA. Bulk measurements were performed on 0.1 M sodium phenolate, made by combining phenol and sodium hydroxide solution and achieving a pH of 12-13 to ensure a high deprotonation of phenol molecules (pK_a = 10). All experiments were carried out on solutions at 20 °C, equilibrated to that of the surrounding environment. High purity water (Millipore, Milli-Q Gradient A10, 18.2 MΩ) was used in all cases. The TA plot of aqueous phenolate, excited at 257 nm, is shown in Figure 5.2.

The TA spectrum of aqueous phenolate has been well-studied previously.[98,135] At t_0, following excitation at 257 nm, a broad positive band rises and peaks within two picoseconds and subsequently decays on a timescale of tens of picoseconds. The positive band, representing the optical absorption of the hydrated electron, blue-shifts and narrows within the first 5 ps, stabilising at around 720 nm.[160] TA spectra and kinetics traces are shown in Figure 5.3 and Figure 5.4, presenting the difference in kinetics across the shifting spectral profile. The effect of this, when viewed over small wavelength ranges, is that at longer wavelengths the profile appears to peak earlier and decay faster, whereas shorter wavelengths show a delayed peak and less of an initial decay in intensity (Figure 5.4).

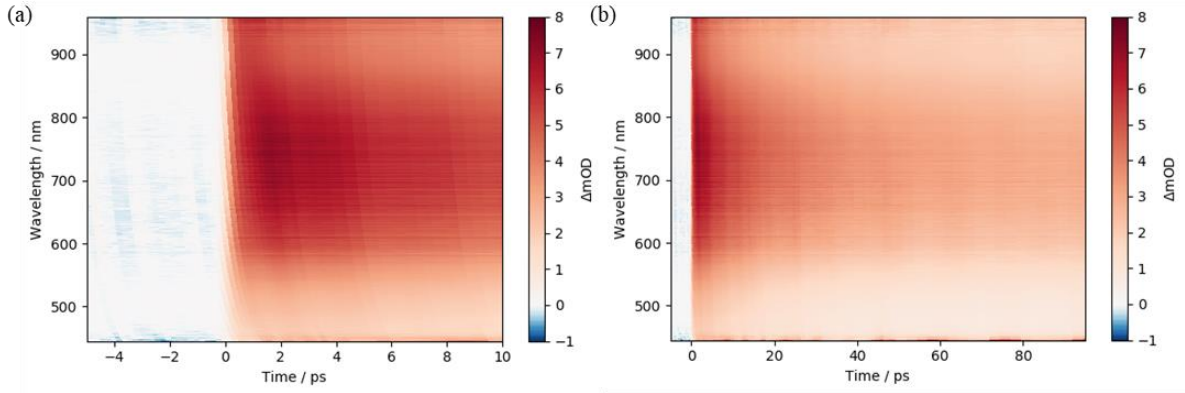

Figure 5.2: TA spectra of 0.1 M aqueous phenolate excited at 257 nm (a) at early times and (b) at longer times. The broad positive peak after t = 0 arises from the hydrated electron.

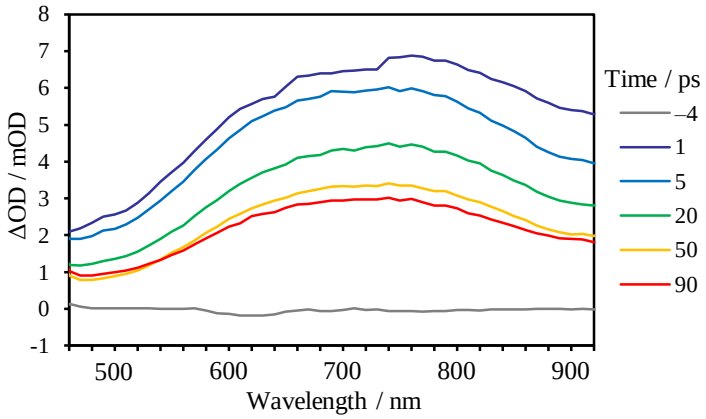

Figure 5.3: TA spectra at different pump-probe delay times showing spectral profile of the hydrated electron following photodetachment from 0.1 M phenolate excited at 257 nm.

The form of the TA kinetics can be described well by the mechanism presented in Figure 5.5, which was originally used to describe the electron population following photodetachment of aqueous chloride.[161,162] After excitation at 257 nm, the excited phenolate ions eject an electron at a production rate k_p. The electron remains in close proximity with the parent radical, even within the same solvation shell. The electron-radical contact pair then either nonadiabatically recombines (primary/geminate recombination) at a rate k_n, or dissociates at a rate k_d, resulting in a separate radical and 'free' hydrated electron that goes on to be fully solvated. At much longer time delays in the nanosecond regime, the electron population continues to decay via secondary recombination or diffusion-controlled interaction with reactive species, leading to a long-term signal decay. On the time scales probed here, the electron population instead appears to reach a steady-state offset at long delay times, termed the 'escape yield', which can offer a metric of the fraction of electrons that escape recombination with the parent.

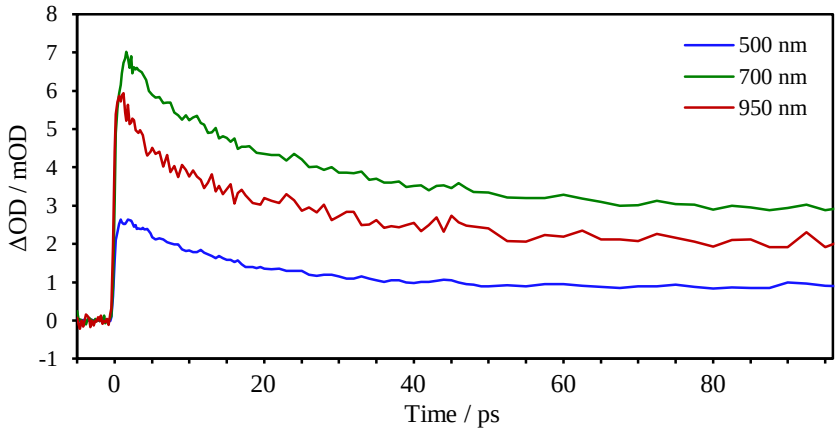

Figure 5.4: TA kinetics showing the form of the hydrated electron signal at following photodetachment from 0.1 M phenolate excited at 257 nm.

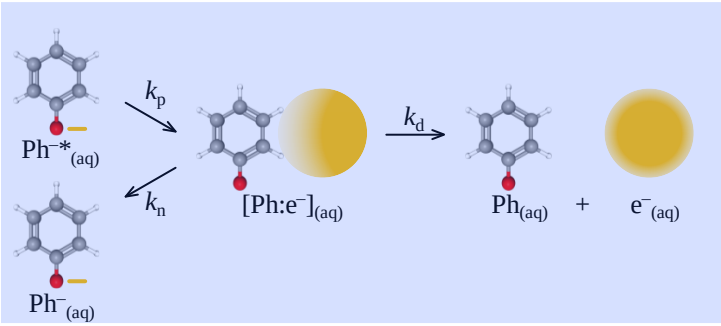

Figure 5.5: Mechanism of bulk aqueous phenolate photo-oxidation at 257 nm.

Assuming the absorption spectrum of the electron, whether in the contact pair or as a free hydrated electron are indistinguishable, the absorption signal will be a sum of both species. The population of hydrated electrons and contact pairs in bulk, $N_{e,B}(t)$, can be expressed as

$$N_{e,B}(t) = \frac{k_d}{k_d + k_n} + \frac{k_p}{k_d + k_n - k_p}\left[\frac{k_p - k_d}{k_p} e^{-k_p t} - \frac{k_n}{k_d + k_n} e^{-(k_d + k_n)t}\right]. \quad (5.3)$$

This model was convoluted with a Gaussian IRF with a FWHM of 250 fs observed via the chirp band from solvent-only TA data, as presented in section 3.2.5.2. Fitting this model to the data at 720 nm yields the lifetimes k_p^{-1} = 0.5 ± 0.1 ps, k_n^{-1} = 32 ± 2 ps and k_d^{-1} = 43 ± 4 ps (using scipy.optimize.curve_fit in Python 3), which are quite consistent with previous measurements.[98] In the above expression, the fraction k_d / (k_d + k_n) is the escape yield, which manifests as a constant offset in the model. The quality of the fit is highlighted in Figure 5.6, showing that the model describes the data well. With the photo-oxidation of phenolate in bulk solution described accurately, these timescales could then be compared properly to the surface dynamics investigated.

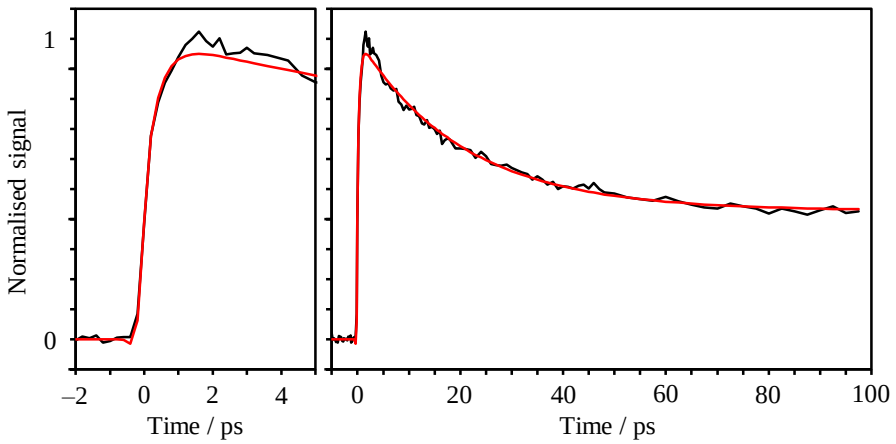

Figure 5.6: Normalised TA kinetics at 720 nm following photodetachment from 0.1 M phenolate excited at 257 nm (black) and fit specified by equation (5.3) (red).

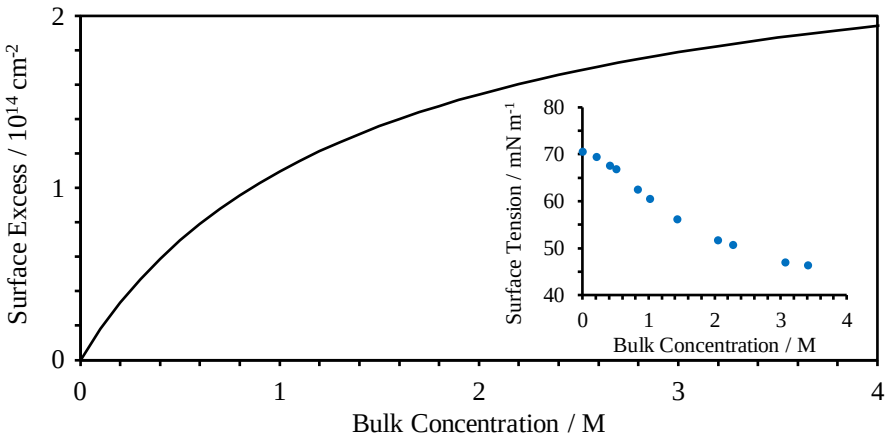

Figure 5.7: Surface excess curve of aqueous sodium phenolate solution at pH 13. Inset: Surface tension data used to determine the surface excess curve.

5.2.2. Sum-Frequency Generation

TR-OKG-ESFG measurements were made on 0.15 M sodium phenolate prepared similarly to TA measurements (also at a pH of 12-13). Surface tension measurements (Appendix B) indicated this corresponded to a 7% surface coverage of phenolate molecules (Figure 5.7), in agreement with previous studies.[159] The sample was excited at 257 nm, and the SFG response was probed using the fields (423 nm; 720 nm, 1026 nm). The detection range was approximately 415-430 nm. Initial time-resolved measurements focussed on observing the electron dynamics following surface photodetachment, for comparison with bulk. The raw results of a TR-OKG-ESFG measurement are shown in Figure 5.8. The data presented in Figure 5.8 show an average of 8 scans, with each data point constituting 3×10^5 laser shots per scan.

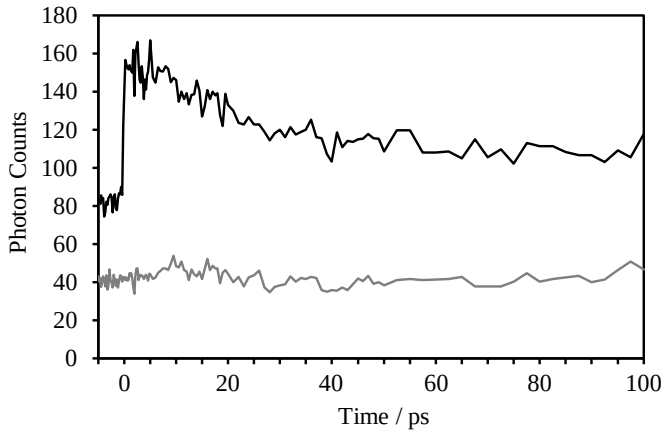

Figure 5.8: Raw TR-OKG-ESFG photon counts collected for the photo-oxidation of surface phenolate, excited at 257 nm. Fields used are (423 nm; 720 nm, 1026 nm). Pump-on is shown in black and pump-off is shown in grey.

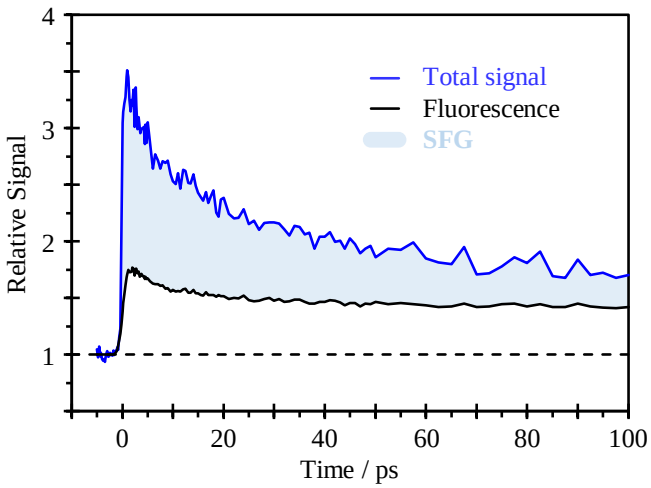

Figure 5.9: Relative photon count levels of SFG and fluorescence measurements. The data is normalised to the pump-off count before zero. The averaged SFG and fluorescence data is shown. Note figure has been shown before, as Figure 3.14, in describing how the SFG signal is extracted from the raw data.

The raw pump-on traces show a fast rise around t_0, followed by a decay similar to bulk dynamics seen with TA. As mentioned previously, the raw data shows a contribution from bulk fluorescence as well as surface SFG. This can be separated by taking an identical measurement where the SFG fundamental fields are blocked before the sample surface (Figure 5.9). The fluorescence contribution, $S_F(t)$, can be fitted to an arbitrary function that describes the signal well:

$$S_F(t) = \left(A\, e^{-bt} + C\right) \;*\; \mathrm{IRF}_{OKG}(-t_g)\,, \tag{5.4}$$

where A, b and C are constants describing the amplitude, rate and longer-term offset of the fluorescence decay, respectively. $\mathrm{IRF}_{OKG}(-t_g)$ is the instrument response function of the OKG arrangement, assumed to be Gaussian with a FWHM of approximately 2 ps. An example of this fit compared to the form of the fluorescence is shown in Figure 5.10. When benzene or toluene were used as the KM this was not strictly true, and the leading edge of the fluorescence traces measured showed a broader rise due to the exponential orientational relaxation of the KM. This was not accounted for in S_F but did not affect the dynamics after t_0; as a result, 'corrected' SFG data showed a small rising contribution before t_0. This was generally small compared to the prompt signal after t_0. S_F was then be subtracted from the raw pump-on data, leaving only the SFG contribution. This can then be normalised to the pump-off channel count at each corresponding time delay and square-rooted to correspond to the concentration of e_S^- and compared to the bulk dynamics via TA, shown in Figure 5.11.

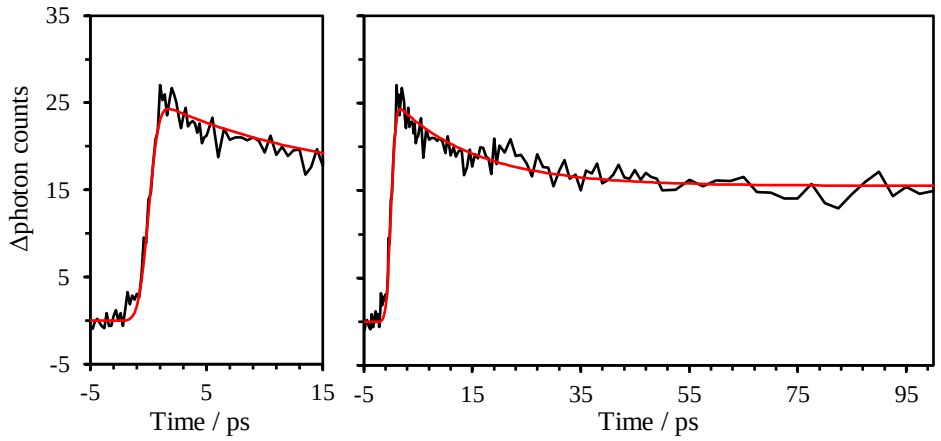

Figure 5.10: Difference in photon counts between pump-on and pump-off channels for 257 nm excitation of phenolate in the absence of SFG signal (black), with fitting according to equation (5.4), for a single measurement. Before t_0 a small non-gaussian rise can be seen as a result of the trailing edge of the Kerr gate. Detection wavelengths were 415-430 nm.

5.3. Discussion

Figure 5.11 compares the normalised TA ΔOD data at 720 nm and the normalised √SFG relative photon count (423 nm; 720 nm, 1026 nm). The signals should be comparable, as in both cases, the amplitudes present a measure of signal that is proportional to the concentration of hydrated electrons (and contact pairs) in each environment: in the case of TA, through the change in absorption at 720 nm; and for SFG, through the resonance-enhancement of the SFG field via the electrons' (and contact pairs') TDM at 720 nm, once plotted as √SFG.

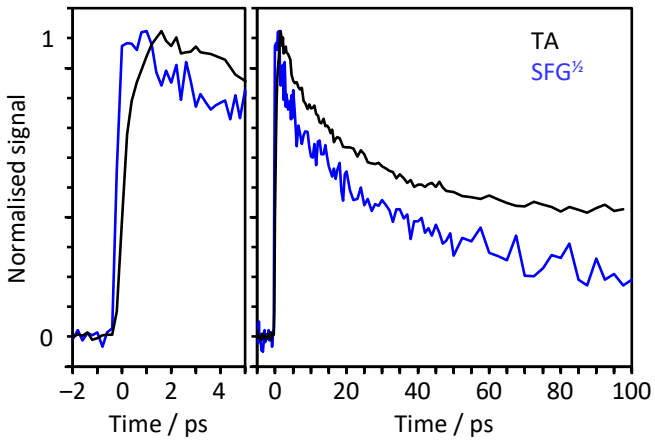

Figure 5.11: Normalised comparison of TA and SFG data corresponding to the concentration of hydrated electrons produced by the photo-oxidation of aqueous phenolate. TA data in black, SFG data in blue. The square root of the SFG intensity is shown so that both signals are proportional to concentration.

The surface dynamics appear overall similar to in the bulk at 720 nm. The electron signal shows a fast rise and subsequent decay, however there are clear differences in the dynamics. At the surface, the signal rise is much faster; practically limited by the time resolution of the experiment (~250 fs). Furthermore, whereas the TA signal reaches a steady offset by approximately 100 ps, the surface signal apparently continues to decay on a shorter timescale. Indeed, trying to fit the bulk model to the surface data showed much poorer agreement than the TA signals. The bulk model as described by equation (5.3) oscillated around the data and failed properly to capture the decay at long times without reaching a constant offset. An adapted model was derived to describe the surface dynamics, based on the bulk kinetic model. Firstly, a very similar model was proposed that set $k_p >> k_n$, k_d, reflecting the very rapid initial onset of signal. Equation (5.3), in the limit $k_p \rightarrow \infty$ can be rewritten as

$$N_{e,S}(t) = \frac{k_d}{k_d + k_n} + \frac{k_n}{k_d + k_n} e^{-(k_d + k_n)t}, \tag{5.5}$$

However, this only served to better describe the early dynamics.

In order to properly reproduce the late-time dynamics it was clear a modification to the mechanism of photodetachment was necessary. A plot of $\ln[N_{e,S}(t)]$ shows that the model is not a single exponential decay, and has multiple components, as seen by Figure 5.12. Given the additional decay of the electron signal at long times, an additional process was considered that would remove electron population from the surface, but which also had reasonable physical meaning. In bulk studies of hydrated electrons produced from the CTTS of iodide anions, additional decay pathways were added to account for the decay of the long-term offset over hundreds of picoseconds.

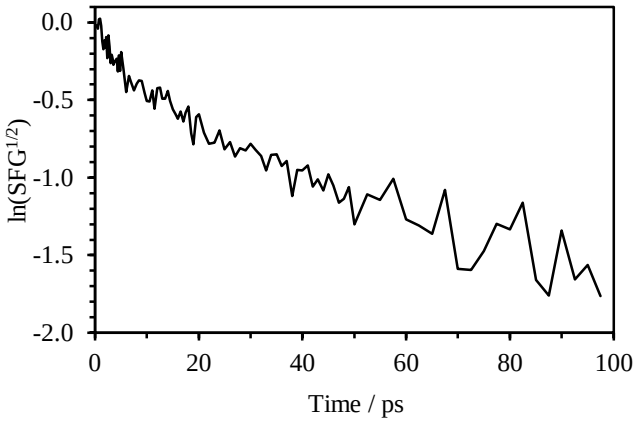

Figure 5.12: Natural logarithm of SFG in Figure 5.11, showing signal is not mono-exponential.

Analysed via a similar model, the electrons dissociated from the contact pair were allowed to diffusively recombine to reform contact pairs that could then repeat the initial kinetics.[148] The rapid disappearance of electron signal in TR-VSFG studies of phenol was attributed to electron diffusion away from the surface and towards the bulk, which moved the electron out of the interfacial probing depth of the SFG field. If a similar process were observed here, this would take place after dissociation of the contact pair as the free electron migrates towards the bulk and leaves the parent radical at the surface; the phenoxyl radical was expected to maintain a similar or higher surface activity of the anion.[149,163] Alternatively, if the electron was highly surface-bound, it may be confined to a form of two-dimensional diffusion along the interface, which may make recombination with the parent more likely if an axis of translational freedom is removed.[164] While distinct from one another, both processes would manifest as a greater decay in the overserved SFG signal at long times. With this in mind, a revised mechanism was presented, as illustrated in Figure 5.13, where the bulk mechanism has been reproduced for ease of comparison.

The revised surface mechanism can be rationalised as follows: excitation of surface-bound phenolate at 257 nm to $Ph^{-*}_{(S)}$ results in rapid ejection of an electron, such that the process k_p is essentially instantaneous. The electron likely detaches close to the parent and then can either recombine at a rate k_n, or the contact pair can dissociate at a rate k_d to give a free surface electron, $e^-_{(S)}$. Subsequently, the $e^-_{(S)}$ will diffuse toward the bulk (or along the surface) at a net rate k_b, resulting in depletion of the observed signal.

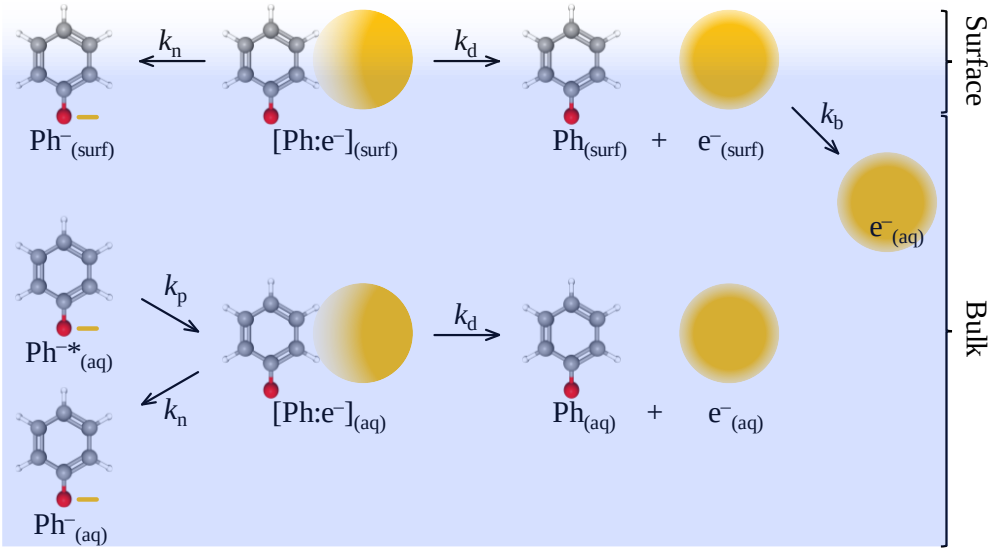

Figure 5.13: Schematic of kinetic models following photo-oxidation of phenolate at the aqueous/air surface and in bulk solution. At the surface, k_p has been omitted for clarity.

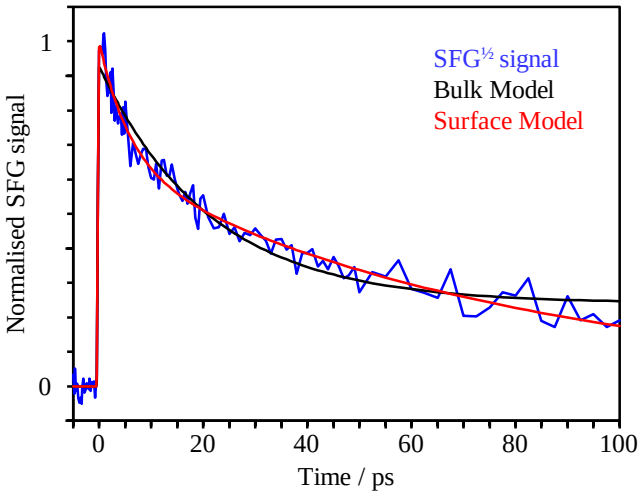

Figure 5.14: Comparison of surface SFG signal (blue) with bulk (black) and surface (red) fitting models. The surface model accounts for diffusion away from, or confined on, the surface.

The differential rate equations relating to the contact pair and surface electron populations can be solved (see Appendix B) to give the number of surface species (contact pairs and surface electrons) that contribute to the SFG signal, $N_{e,S}(t)$:

$$N_{e,S}(t) = \frac{k_d}{k_b - (k_d + k_n)}\left[e^{-(k_d + k_n)t} - e^{-k_b t}\right] + e^{-(k_d + k_n)t} \quad . \tag{5.6}$$

This assumes the process k_b can be well-described by a single exponential decay, and that the $\chi^{(2)}_{S'}$ spectrum of the electron is indistinguishable whether it is in a contact pair or free. Figure 5.14 shows the fit of this model and of the modified bulk model to the SFG signal, highlighting the improved fitting of the surface model which indicated the proposed surface mechanism was describing the dynamics more accurately. The form of the surface model should also allow proper comparison to the rate constants of the bulk model which correspond to the same processes.

Table 5.1: Lifetimes for kinetic processes following the photo-oxidation of aqueous phenolate in the bulk and at the aqueous/air interface. [a]The lifetime was not included in the fit but was taken to be ($k_p \gg k_d$ and k_n).

	k_p^{-1} / ps	k_n^{-1} / ps	k_d^{-1} / ps	k_b^{-1} / ps
Bulk	0.5 ± 1	32 ± 2	43 ± 4	–
Surface	$\ll$0.2[a]	16 ± 1	11 ± 2	78 ± 6

The discussed lifetimes of kinetic processes in both environments are presented in Table 5.1. It can be seen that overall the interfacial dynamics are broadly similar, but faster by 2 to 4 times, in the case of k_n and k_d, respectively, and with an additional electron loss pathway at longer times. The acceleration of the rate constants can be affected by a number of factors; the lower water density at the interface will impact polarisation, electrostatics, hydrogen bonding and the anisotropy of the above factors as well. Intuitively, the increase in k_d could be rationalised as the lower density of water molecules would be expected to enable the contact pair $[Ph{:}e^-]_{(S)}$ to dissociate more readily, because it would be easier to break the solvation cage surrounding both species. The faster nonadiabatic recombination (k_n) could be justified as the free energy surfaces are altered leading to changes in charge transfer rate in a Marcus-type model. Similar behaviour was seen for the CTTS dynamics of aqueous iodide at the aqueous/air interface, which showed increases by factors of 1.3 in k_d and 1.4 in k_n.[134] The larger effect for phenolate compared to iodide may be associated with the system's size or with other factors such as electric fields at the surface and the dipole moment of the phenoxyl radical, which points toward the vapor phase and may direct the initial charge transfer forming the contact pair.

The second clear difference between the surface and the bulk signals is an almost instantaneous appearance of the signal: $k_p^{-1} \ll 200$ fs, which was limited by the time resolution of the experimental setup. As mentioned previously, the TA data at 720 nm corresponds to the fully thermalised $[Ph{:}e^-]_{(S)}$, but after its initial generation the electron is not fully solvated, and blue-shifts as it thermalises and localises within a solvation shell. In the SFG experiment, the 1026 nm field was resonant with this presolvated contact pair at earlier times. Additionally, the larger spatial distribution of the presolvated electron is likely associated with a larger $\chi^{(2)}$,[165] which will further amplify the early signal in a nontrivial way. Hence, the appearance dynamics are expected to be faster in the SFG experiment compared to the transient absorption due to the additional resonance, and are estimated to decay within a few hundred femtoseconds.

Finally, the term k_b, whether associated with electron diffusion towards the bulk or geminate recombination, is a purely surface effect. Importantly, hydrated electrons are also generated in the bulk below the surface layer, due to the experimental arrangement of the pump field directed down into the surface. In principle, electrons formed this way could diffuse from the bulk to the surface, as the process k_{-b}. On the other hand, the concentration gradient of phenolate, and thus the electrons generated, does oppose this, so it is unclear how significant an effect this process will have.

Theoretical work suggests that electron diffusion from the surface to the bulk takes place on an approximately 10 ps time scale,[152,166] which is broadly consistent with the k_b value observed here. If additional surface secondary geminate recombination contributed to k_b, then the internalisation would be even slower, suggesting that migration of $e^-_{(S)}$ to the bulk may be the dominant process.

While the photo-oxidation of phenolate at the water/air interface differs from the bulk, the difference is quite modest in comparison to that observed for phenol using time-resolved heterodyne-detected VSFG, where electrons were formed within 100 fs and migrated to the bulk within 300 fs (i.e., before any dynamics associated with k_d).[149] However, the photodynamical mechanisms are also very different for phenol and phenolate. The decay of phenol involves H atom tunnelling through a barrier connecting the initially excited $^1\pi\pi^*$ state to the dissociative $^1\pi\sigma^*$ state.[167,168] At the water/air interface, it was argued that the $^1\pi\sigma^*$ state was stabilized relative to the $^1\pi\pi^*$ state, with calculations supporting this suggestion.[153,169] In phenolate, there is no $^1\pi\sigma^*$ state and the overall charge-transfer dynamics differ substantially.[170] Furthermore, it is unclear how much the structural rearrangement of the radical following electron ejection will affect the local structure and fields at the interface compared to phenol.[171] Hence, it is perhaps not so surprising that the aqueous/air interface might impact the overall dynamics so differently for phenol and phenolate.

5.4. Phenol

As well as photo-oxidation of phenolate at the aqueous/air interface, experiments were also performed on phenol. Initially, solutions of 200 mM were used, however concentrations were reduced in order to reduce the potential effects of surface excimers that might arise. Subsequently, 25 mM and 57 mM phenolate were used, in order to match the samples used in the previous surface VSFG study.[149] These lower bulk concentrations were chosen to give a 20% and 50% surface coverage of phenol, respectively. No acid or base was added, resulting in pH values of between 5 and 6, respectively. The 200 mM samples corresponded to ~ 80% surface coverage, at bulk pH 5. Surface coverage was verified via drop-shape surface tensiometry, shown in Figure 5.15.

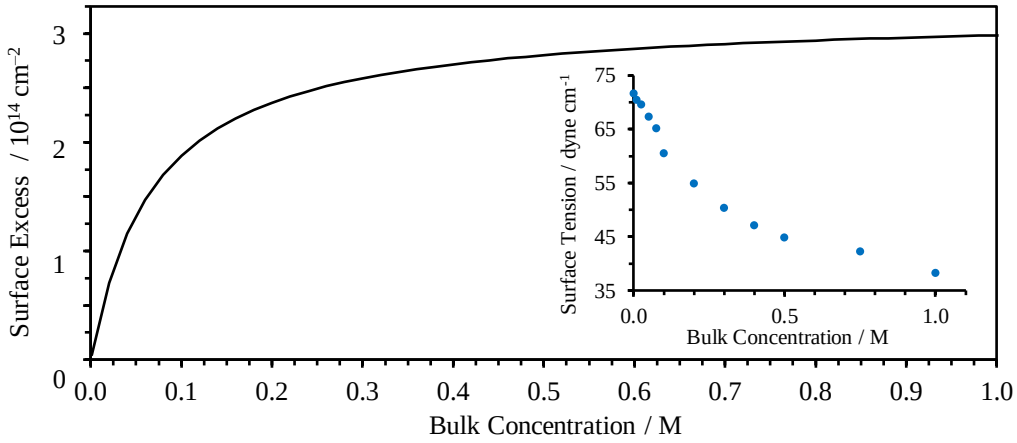

Figure 5.15: Surface excess curve of aqueous phenol solution. Inset: Surface tension data used to determine the surface excess curve.

Given the observation of hydrated electron dynamics on surface phenolate, the setup here was used to attempt to probe the electron produced from phenol in the same environment. A small selection of the results of TR-OKG-ESFG experiments on all three of the above concentrations using the same field combination are shown in Figure 5.16. Strikingly, no SFG signal was observed; there were no discernible transient changes in SFG over the first few 100 ps, including close to t_0. Samples of sodium phenolate that showed transient SFG signal were then acidified with hydrochloric acid and showed disappearance of signal, whereas phenol solutions that showed no signal had sodium hydroxide added and showed the signals as described in section 5.2.2. Despite phenol's higher fluorescence quantum yield compared to phenolate,[172] very little fluorescence is seen the transients in Figure 5.16. This is due to the spectral range of detection used: 415-430 nm. In aqueous solution, phenol's fluorescence maximum lies close to 300 nm, whereas for phenolate the emission maximum red shifts to 340 nm, and thus is more evident in the time-resolved data once gated.

No signal was seen despite being sensitive to a change of < 3% of the nonresonant background level. By comparing absolute signal levels between the phenol and phenolate experiments, it was concluded that phenolate produced more than 100 times the SFG signal at early times than the level of noise in Figure 5.16, corresponding to more than 10 times the concentration in interfacial electrons.

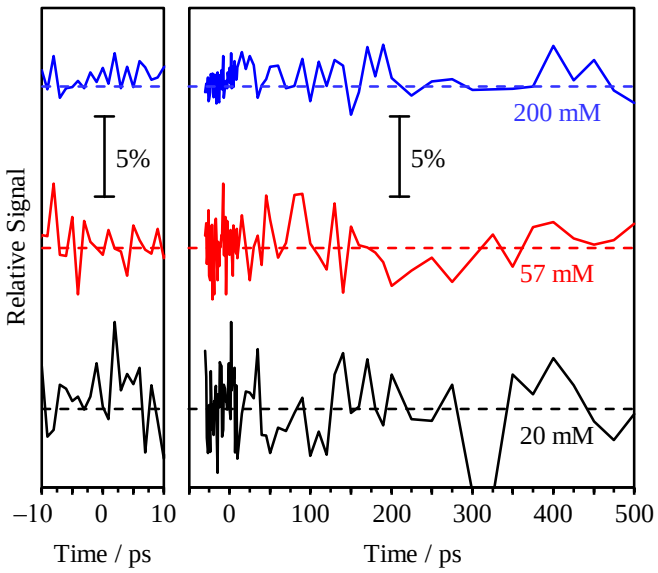

Figure 5.16: Averaged relative difference in pump-on vs. pump-off photon counts for three phenol concentrations. Within the error, there was no discernible SFG signal. At high bulk concentrations, a small offset can be seen aft er t_0 from the time-resolved fluorescence transmitted by the OKG.

The absence of electron signal was surprising in light of the previous TR-VSFG study on phenol, but there are possible explanations. Some of this difference can be accounted for by the potentially larger excitation cross section for phenolate compared to phenol. Excitation at 257 nm compared to 266 nm could have an impact and may alter the dynamics,[98,170] as has been shown for phenolate, although it would seem likely that hydrated electrons would also be formed at 257 nm. The sensitivity of the phenol experiment may also differ from that of phenolate because of differences in their respective electronic structure,[170] seen by the bulk absorption spectra of both species in Figure 5.17. Specifically, it has been shown computationally that S_2 lies much closer to S_1 in phenolate than in phenol, and that the S_2 has a photoexcitation cross section that is about 3 to 4 times larger than excitation to S_1.[170] At 257 nm, it is possible that there is contribution from excitation to S_2 in addition to S_1. Moreover, the cross-section of excitation of phenol at 257 nm compared to 266 nm in bulk water is approximately 3 times lower (Figure 5.17). However, at 257 nm, the absorption cross sections are in fact very similar between phenol and phenolate, and there is insufficient difference to suggest that the ESFG experiment here would not be sensitive to electrons for the phenol surface. Furthermore, there is much larger concentration of molecules initially at the surface in phenol than phenolate. For phenolate, the surface coverage is ~7% (Figure 5.7) compared to 25%, 50% and 80% (Figure 5.15) for phenol. Taking the initial concentration and the cross-sections into account, the experiment here should be sufficiently sensitive to observe the hydrated electron from photo-excited phenol at 257 nm under the experimental conditions used.

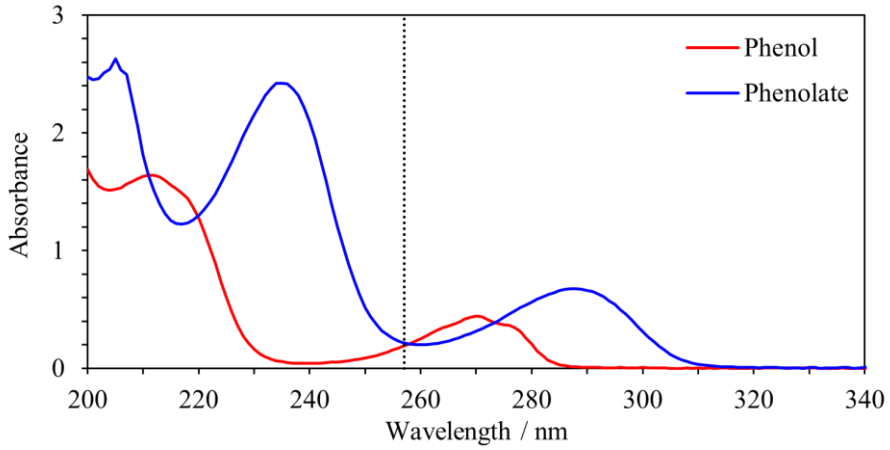

Figure 5.17:Bulk absorbance spectra of 3×10^{-4} M aqueous phenol solution (red) and 3×10^{-4} M aqueous sodium phenolate solution (blue). The dashed line indicates the 257 nm pump wavelength used in surface and bulk time-resolved measurements.

Though, this doesn't accurately account for changes in absorption cross-section due to the interface, or other factors such as initial yields of electrons which are not known for both at the water/air interface. As an example, interfacial CTTS spectra have been shown to red-shift and narrow in the case of iodide, so it is plausible that similar changes may affect phenol and phenolate.[173] Alternatively, one could ask if the OH stretching region of water in VSFG studies is sufficiently specific to identify the various intermediates that could be formed, such as the initially excited $^1\pi\pi^*$ state which was not considered.

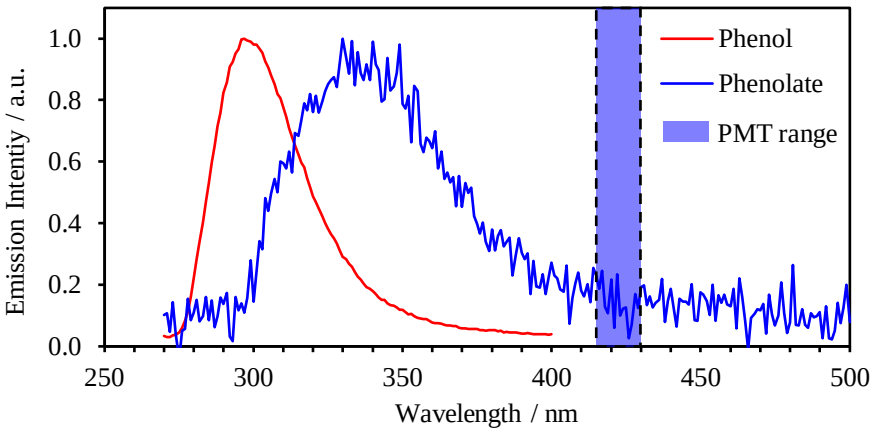

Figure 5.18: Normalised emission spectra for phenol (red) and phenolate (blue), excited at 257 nm. The detection range in the TR-OKG-ESFG experiments was 415-430 nm, shaded in blue.

5.5. Conclusions

Hydrated electrons generated by photo-oxidation of the phenolate anion were probed directly at the aqueous/air interface by TR-OKG-ESFG spectroscopy.[174] The dynamics of the hydrated electron appear similar to those in bulk but were 2 to 4 times faster at the surface. A modified mechanism has been proposed to describe the dynamics, with additional signal decay at the surface attributed to diffusion of the electron from the surface to the bulk, or increased geminate recombination via a different mechanism.

Photo-oxidation of surface phenol was investigated too, which had previously been observed to generate hydrated electrons as a photoproduct. No electron signal was observed, in contrast with recent TR-VSFG studies of the same system. Despite this, it is believed this setup should have the sensitivity to observe this system too, and potential reasons for the absence of hydrated electron signal from phenol are discussed.

6. Electronic Surface Spectrum of the Hydrated Electron

6.1. Introduction and Motivation

Surface ESFG spectroscopy is a powerful spectroscopic tool which can reveal a wide range of information about interfacial chemical systems, including both structure and dynamics. Simple direct methods utilising three narrowband fields are comparatively easy to implement, but are insensitive to the full depth of information that can be obtained through these nonlinear methods. As mentioned in chapter 5, overlap of multiple resonances can make signal interpretation challenging; the identity of the transitions contributing to the resonant enhancement is key for accurate interpretation of the signals and cannot always be easily disentangled. For instance, it is unclear whether the instantaneous appearance of SFG signal in chapter 5 is a result of the prehydrated electron, prompt absorption in the 720 nm range, or even a resonant species at 423 nm. Probing at discrete wavelengths is thus insensitive to the broader picture, and especially spectral shifts, which are important for probing processes such as solvation, isomerisation or wavepacket dynamics on excited states.[175–179]

Broadband TA spectroscopy allows clear visualisation of these processes, such as for the hydrated electron in Figure 5.2, which clearly shows the blue-shifting of the optical absorption as the electron solvates. The effect this has on the observed dynamics over the range of the spectrum is significant, as fitting of equation (5.3) yields values of k_p, k_n, and k_d that are wavelength dependent (though there have been models that take this into account[148]). Consequently, without a broadband perspective of a dynamic system, important spectral information can be overlooked or misinterpreted.

Broadband SFG has become the norm for VSFG studies which frequently use a narrowband ω_1 in the visible or near-IR and a broadband, tuneable ω_2 range that spans the IR vibrations of interest.

Indeed, most broadband studies use ω_2 as their broadband field, whether for vibrational or electronic SFG, by generating the IR range from difference-frequency generation in OPAs.[150,180–182] This typically produces more stable, or easily accessible, continua than those generated in the visible region via bulk media or optical fibers.[183,184] Unfortunately, the generation of such a broadband source was beyond the initial capabilities and scope of the TR-OKG-ESFG setup presented here. Instead, for these first measurements, a more basic approach was used: sequentially scanning ω_1 (and hence ω_{SFG} also).

6.2. Experimental

Measurements were set up as in section 5, with the only differences being the data presented here was run at 12 kHz rather than 60 kHz, and exchanging the second lens in the OKG assembly for one with an equal focal length but smaller diameter (Ø = 6 mm). The former was used to reduce sample degradation at longer experimental times and was found to give marginally better contrast between pump-on and pump-off transients. Replacement of the lens was made to reduce the amount of KM luminescence that was collected.

The experiment was run several times at different OPA wavelengths, however despite practical steps to make this easier, swapping between these was an intensive task. Whenever ω_1 was changed, several steps had to be carried out to ensure the surface was probed properly. After selecting a wavelength and optimising the OPA signal output, the spatial and temporal overlap of ω_1 and ω_2 had to be optimised. In the case of spatial overlap, this was caused by small changes in the divergence or pointing of the output at different wavelengths, whereas the temporal overlap typically varied within 1-2 ps in the range ω_1 = 620-800 nm. The surface SFG then had to be realigned to the PMT because of the Pellin-Broca prism used to disperse the light after the Kerr gate. Because it was mounted properly about its rotation axis, this was achieved simply by rotating the prism. For detection, different sets of filters were used based on the SFG wavelength to give a narrow admission window. Typical widths were 10-20 nm, and depending on the admission width and the proximity to the peak of the phenolate emission maximum, different levels of unwanted fluorescence were seen in the measurements. This was seen in both the steady-state offsets and the time-resolved fluorescence components and did not necessary vary linearly with the ω_1 selected. Finally, the OKG overlap also had to be recentred on the surface SFG pulse which moved by the same amount as the temporal overlap between ω_1 and ω_2. This was repeated for ω_1 wavelengths between 620 nm and 800 nm, with measurements repeated on different days to confirm reproducibility.

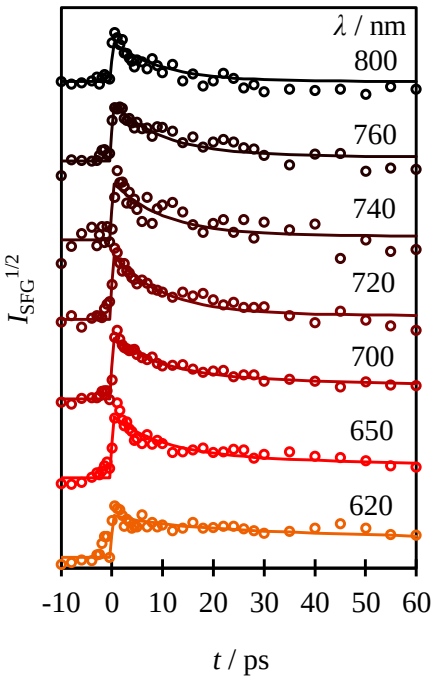

Figure 6.1: Kinetics of the interfacial hydrated electron generated from 257 nm excitation of phenolate at a range of ω_1 wavelengths, with ω_2 at 1026 nm.

6.3. Results

The results of TR-OKG-ESFG experiments are shown in Figure 6.1. It is clear that the dynamics of the SFG signal are not constant across the spectral profile, with longer wavelengths showing a decay to the baseline and shorter ones showing a clear offset at $t > 50$ ps. The cause for this would either be a large blue-shifting/spectral narrowing of the resonant transition, or multiple spectral features evolving independently. As a result, a new fitting model was investigated rather than independently fit each wavelength using the model in (5.6), as each would give differing fitting parameters that were not collectively meaningful. The data was to be described via a global fit, which required appropriate normalisation of the data sets with respect to one another.

In order to compare the SFG signals accurately to one another, the size of the resonant signal contribution was normalised to the nonresonant background signal present in each of the pump-off traces; a ratio of 1.5 means the pump-on or -off SFG signal was 0.5 times greater than the nonresonant SFG signal before zero. Experimentally, data taken on different days were prone to variations in stability or external conditions. This ranged from OPA instability to the efficiency of the OKG, which was realigned after every change of wavelength, to the responsivity of the PMT across the spectral range.

When comparing the pump-on to the pump-off channels, the only difference between the two was the presence of the excited species at the interface, which was affected by pump-probe overlap, sample concentration and pump power. The sample concentration was kept controlled between measurements, with an approximate maximum error of 5%. The pump energy also varied no more than 5% within, and between, datasets. The main source of uncertainty within the relative amplitudes of signal trace was the spatial pump-probe overlap, the error of which was difficult to quantify, as well as the resulting signal uncertainty it would introduce. This overlap was monitored using a microscope camera to track and minimise any changes between wavelengths.

Theoretically, the ratio of the pump-on to the pump-off signal, $I_{on}(\omega_{SFG})$ / $I_{off}(\omega_{SFG})$ is approximated by

$$\frac{I_{on}(\omega_{SFG})}{I_{off}(\omega_{SFG})} = \frac{\left|\chi^{*(2)}_{S'}(\omega_{SFG}: \omega_1, \omega_2)\right|^2}{\left|\chi^{(2)}_{S'}(\omega_{SFG}: \omega_1, \omega_2)\right|^2} \quad , \tag{6.1}$$

where $\chi^{*(2)}_{S'}$ is the effective surface susceptibility of the excited sample and $\chi^{(2)}_{S'}$ is the effective surface susceptibility of the unexcited sample. Equation (6.1) does assume that the surface refractive index is unchanged upon excitation, which is not strictly true, but with the low surface coverage of phenolate molecules and the low fraction of those that are actually excited, this is a reasonable approximation. Assuming the nonresonant contribution of $\chi^{(2)}_{S'}$ does not change upon excitation, the ratio in (6.1) is proportional to the square of the resonant contribution of $\chi^{*(2)}_{S'}$, and thus the square of the concentration of interfacial hydrated electrons. More importantly, the resonant part of $\chi^{*(2)}_{S'}$ is proportional to the TDM of the transition providing the resonance:[185]

$$\chi^{(2)}_{R} \propto \frac{\vec{M}_j \vec{A}_{ik}}{\Omega - \omega - i\Gamma} \quad . \tag{6.2}$$

In (6.2), $\vec{M}_j$ is the transition dipole moment of the s ← p transition of the electron, and $\vec{A}_{ik}$ is the Raman transition probability of the anti-Stokes process from the electron p state to the ground s state, showing that ESFG transitions must be both optically and Raman active.

Assuming the Raman transition probability is approximately constant across the transition, then proper comparison of the size of the resonant response at each wavelength will allow construction of the electronic 'absorption' spectrum of the hydrated electron at the aqueous/air interface.

After the individual comparison to the relative nonresonant backgrounds, the normalised SFG data is shown in Figure 6.2(a). Collectively, this signal, $S(t,\lambda)$, was described by a simple global fit of the form

$$S(t,\lambda) = \sum_i c_i(\lambda)\, e^{\left(\frac{-t}{\tau_i}\right)} , \tag{6.3}$$

for $i = 2$. This represents the separate monoexponential decays of two distinct species, i, with lifetimes τ_i with associated spectra c_i. The results of this fit are shown in Figure 6.2(b) and the fitted coefficients and their respective time constants are shown in Figure 6.3. The model used was deliberately simplistic and does not involve complex decays or allow for spectral changes of each species, given the limited size and quality of the data and the risk of over-fitting. The results are two species with very different time constants and peak maxima; component A peaks within the probed spectral range somewhere close to 700 nm, with a lifetime of 10 ± 2 ps, whereas the other rises towards the blue edge of the spectrum with a lifetime of over 150 ps. The lifetime of the second component, B, is much longer than the time range investigated, and has a large associated error.

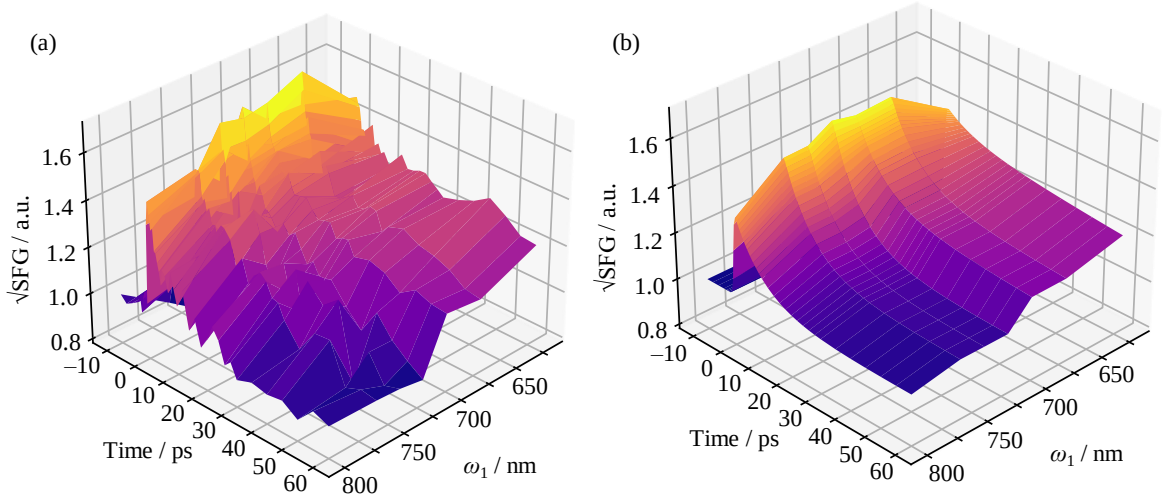

Figure 6.2: (a) 3D plot of normalised SFG data. (b) 3D plot of global fit in equation (6.3).

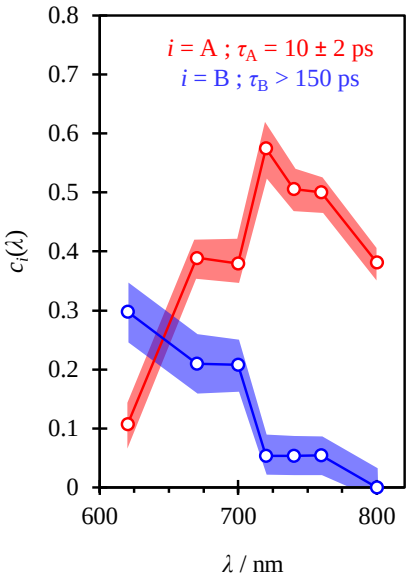

Figure 6.3: Spectral components c_i from fitting of model in equation (6.3) as a function of ω_1. Shaded regions indicate associated errors.

The residuals do show a systematic trend at longer times and longer wavelengths, which is almost certainly a product of the model being constrained to values of 1 or larger and the fluorescence subtraction before zero (as discussed in section 5.2.2 and illustrated in Figure 5.10) resulting in values slightly lower than 1 at the longer wavelength end, whereas the model is constrained to values ≥ 1.

6.4. Discussion

The peak maximum of the first component, A, is in moderate agreement with the bulk absorption spectrum of the hydrated electron, shown in Figure 6.4, within the experimental resolution. Hence, it is concluded that species A corresponds to $e^-_{(S)}$. This is also supported by the sharp rise of signal across the whole spectral range, believed to be resonance enhancement of the ω_2 field with the prehydrated electron. B's amplitude rises towards the low end of the spectral range and is not seen to a comparable magnitude in TA data. Species absorbing towards 600 nm may reflect the S_1 state of phenol or phenolate, or some kind of excimer formation as seen in phenol.[145,158] The hydrated electron also has absorption to higher excited states below 700 nm that extend further into the visible, however this can be most likely be ruled out on account of B's significantly different lifetime. Also included in Figure 6.4 is the absorption spectrum of the phenoxyl radical taken in an argon matrix,[157,186] along with the spectrum of interfacial species B, plotted as a function of the SFG wavelength.

The agreement shows that ω_{SFG} is probably resonant with the surface phenoxyl radical, leading to the resonance enhancement of the SFG signal, which remains at the interface for hundreds of picoseconds, as seen in a previous VSFG study.[149] The small red-shift of the feature in the data presented here may be on account of interfacial solvation, as has been seen in other surface spectra.[173] Alternatively, a recent study has proposed that excitation of phenolate at 257 nm can proceed via partial excitation into the S_2 state, which forms a phenoxyl radical in an excited state with a red-shifted spectrum at 427 nm in the ensuing contact pair.[146] If the 257 nm excitation does proceed via a mixed S_1 and S_2 pathway, B may represent a combination of the ground- and excited state phenoxyl radical. The absolute intensities of $c_i(\lambda)$ are not quantitatively comparable to the absorption spectra for $e^-_{(aq)}$ and the phenoxyl radical, and the latter two have been scaled in Figure 6.4 to aid comparison (the maximal molar extinction coefficients are $\varepsilon_{e(aq)} = 2.3 \times 10^4$ M^{-1} cm^{-1} and $\varepsilon_{PhO} = 3.0 \times 10^3$ M^{-1} cm^{-1}, respectively[187,188]).

The decay-associated SFG spectrum of $e^-_{(S)}$ resembles the absorption spectrum of $e^-_{(aq)}$, with the peak position being almost identical. This is expected for an electron residing at the interface but with most its electron density within the solvent, akin to the most stable water cluster anions[189–191] and in agreement with previous conclusions from certain second-order non-linear experiments[100] and from essentially all theoretically based predictions.[192,193] If the electron were to reside in an orbital that was protruding out of the liquid and into the vapour phase, then the overall orbital size is expected to be larger with a concomitantly smaller p ← s transition energy (i.e. red-shifted absorption maximum).[194]

Despite the limited spectral range, the overall width of the peak of A appears to be somewhat narrower than the bulk hydrated electron, especially on the blue side of the spectrum. This may be an artefact of the non-linear nature of the experiment where the non-resonant terms may affect how the SFG signals scale with concentration. Alternatively, a narrowing of the spectral line may be intuitively justifiable. The blue tail of the bulk hydrated electron absorption spectrum arises from excitation to higher-lying states beyond the first three p-states.[152] These states become much more diffuse and their orbital density extends well beyond the first solvation shell. For a hydrated electron at the interface, the solvation shell is no longer symmetric, and protrusion of the orbital density into the vapour phase will be unfavourable. On the other hand, this narrowing has not been noted in computational studies, and it is possible the spectrum may be skewed due to the pump or probe geometries used experimentally. In the case of the pump, the P polarisation used may impart some symmetry to the photoproducts as a result of selective excitation or directional detachment from the excited parent anion.

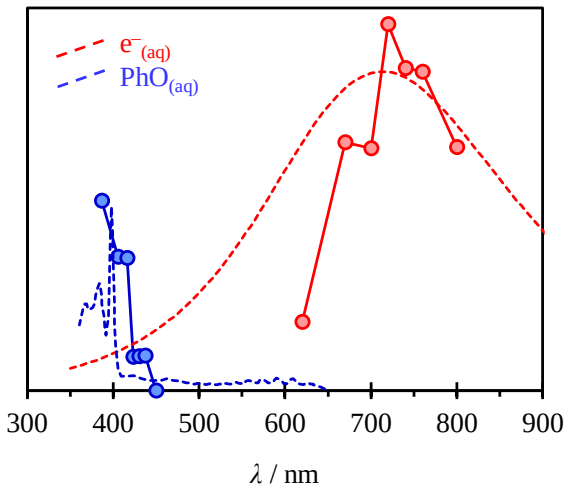

Figure 6.4: Spectral assignments at the aqueous/air interface.

Furthermore, the PPP configuration probes a mixture of the $\chi^{*(2)}_{S'}$ tensor elements in unequal proportions. As a result, the observed spectrum may have a distorted shape if the orientation of the dipole moment varies across its profile.

The possible effect of the phenoxyl radical that remains following photo-excitation on the spectrum of $e^-_{(S)}$ must also be considered. In the bulk, phenolate photo-oxidation leaves $e^-_{(aq)}$ in close proximity to the radical so both are formed as a contact pair. The absorption spectrum for the electron in such a contact pair is virtually identical to that of the free $e^-_{(aq)}$, as can be seen from the TA data in Figure 5.2. The same appears to be true at the water-air interface with the phenoxyl radical showing little effect on the $e^-_{(S)}$ peak position, however it is unclear what effect this will have on the blue tail of the spectrum.

While the spectroscopy and therefore structure of the local environment around the electron is very similar for $e^-_{(aq)}$ and $e^-_{(S)}$, the kinetics are not. In the bulk, photo-excitation of phenoxide leads to a contract pair of the phenoxyl radical and electron that is solvated. The loss of $e^-_{(aq)}$ signal in TA spectroscopy arises from geminate recombination to reform the phenolate anion, with a ~ 40% fraction also dissociating to form the free $e^-_{(aq)}$ after excitation at 257 nm. Critically, the loss of $e^-_{(aq)}$ signal is correlated with loss of phenoxyl radical.[145] In contrast, at the interface, the $e^-_{(S)}$ signal decays with a lifetime τ_A = 10 ± 2 ps, which is more than an order of magnitude faster than that of the phenoxyl radical, and from the global fit it is clear that the decay of $e^-_{(S)}$ is not correlated with the dynamics of the phenoxyl radical. Hence, geminate recombination can be excluded as a dominant loss mechanism at the water-air surface on the timescale observed here, highlighting the dramatic difference in the overall chemistry.

If the $e^-_{(S)}$ does not decay by geminate recombination, another loss mechanism must be provided to explain the disappearance of the SFG signal. As proposed in chapter 5, the electron can migrate into the bulk: $e^-_{(S)} \rightarrow e^-_{(aq)}$. In such a case, the SFG signal would disappear because $e^-_{(aq)}$ is then in a centrosymmetric environment beyond the probing depth of the SFG field. Computational work has suggested that such a transition takes place on a timescale of ~10 ps in remarkable agreement with $\tau_A = 10 \pm 2$ ps.[152,192] On the other hand, the phenoxyl radical remains at the interface for much longer times (>100 ps), which in turn suggests that the contact pair dissociates very rapidly, or is never formed in the first place. Thus, the surface mechanism presented in Figure 5.13 may be closer to that presented in Figure 6.5.

The picture of a hydrated electron buried in the water interface is consistent with most theoretical predictions. However, the findings here contrast with some experimental results. An early liquid microjet experiment suggested that the hydrated electron protruded into the vapour-phase based on the similarity of the measured vertical detachment energy to that obtained from extrapolation of the water clusters with externally bound electrons.[195] Conclusions drawn from heterodyne-detected vibrational SFG spectroscopy suggested a similar binding motif based on comparison of vibrational features seen in such clusters with that at the water-air interface.[150] Here, the electronic spectrum of the hydrated electron is shown to be similar to that in the bulk, suggesting that the electron is fully solvated with only minimal electron density exposed to the vapour phase.

The structure of $e^-_{(S)}$ is important because if it was more diffuse and protruding into vapour phase, then it would have different associated energetics and chemical reactivity. For example, it would imply an energy range commensurate with electron attachment to DNA leading to strand-breakages.[195–197] While energetics of $e^-_{(S)}$ and $e^-_{(aq)}$ are similar, their dynamics and reactivity are very distinguishable.

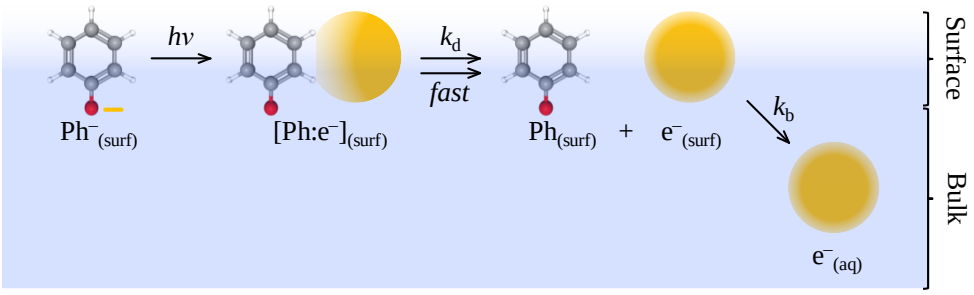

Figure 6.5: Schematic of kinetic model following photo-oxidation of phenolate at the aqueous/air interface.

The rapid loss of $e^-_{(S)}$ from an interface may suggest that photo-oxidation in other environments could be driven by rapid loss of the initially formed electron across a boundary. For example, in GFP, photo-oxidation from the chromophore leads to electron emission through the protein barrel.[198]

Despite the differences in dynamics observed following excitation of phenolate at the water-air interface, an SHG experiment following the dynamics of iodide showed that $e^-_{(S)}$ remained at the interface for >700 ps, contrasting the observation of the $e^-_{(S)} \rightarrow e^-_{(aq)}$ taking place on ~10 ps seen here.[100] There are two potential reasons for this. The iodide experiments were performed at much higher initial concentrations (~1 M compared to 150 mM), and as the sodium salt.

High concentrations of charged solutes can form double layer structures at the interface so that the SHG experiment probes a larger interfacial region and not just the surface.[199] Alternatively, counter ions may drive the electron to the surface so that the $e^-_{(S)}$ is more stable, which is well known to occur for other anions.[200] In the present case for phenoxide, the concentration of Na^+ is ~ 150 mM based on the sodium hydroxide added to each sample, and a higher concentration or divalent cations may reduce the free energy sufficiently to retain $e^-_{(S)}$ at the interface. Hence, the differences in surface electron internalisation could be driven by counter ions, which may account for the observed differences and those on iodide.

6.5. Conclusions

The findings in Chapter 5 have been expanded by observing the dynamics of the interfacial electron following the photo-oxidation of phenolate at the aqueous/air interface over a greater spectral range. It is found that some dynamics observed originate from additional interfacial chemical species other than the interfacial hydrated electron. Two species are observed, identified as the interfacial hydrated electron and the phenoxyl radical. Simple global fitting shows disappearance of the electron from the surface on a 10 ps timescale, whereas the phenoxyl radical signal decays with a lifetime greater than the experimental time frame probed. The electron lifetime is supported by theory, and differences in lifetimes rules out geminate recombination as a major decay pathway at the interface.

The decay-associated spectra generated from the fitting are believed to reflect the surface absorption spectra, and shows that the electron peak maximum does not shift significantly with respect to the bulk.

This represents the first measurement of the electronic spectrum of the hydrated electron at the aqueous/air interface. The work here illustrates how nuanced interfacial structure and dynamics can only be made possible by probing all of the products directly. Future studies may improve the study presented here by using broadband probes, altering the spectral probing region and observing dynamics at longer pump-probe time delays to observe the phenoxyl radical dynamics more closely.

In much the same way that TA spectroscopy has become the condensed-phase standard for observing ultrafast dynamics, broadband TR-ESFG spectroscopy has the potential to access additional insight into a wide range of interfacial systems.

Furthermore, coupled with phase-resolved techniques, broadband time-resolved methods could provide transient interfacial spectra rich with chemical information on structure, dynamics and orientation in a single measurement.

7. Future Studies

7.1. Chemical Systems of Interest

7.1.1. Hydrated Electrons at the Aqueous/Oil Interface

One of the signature strengths of SFG is its ability to probe buried interfaces, as has been done at the water/oil interface in a number of studies.[201–204] Theoretical work has proposed that transfer of a hydrated bulk electron to a water/cyclopentane interface may be associated with a negative change in its Gibbs free energy, i.e. the electron is more stably solvated at the interface. This behaviour is quite different to that seen for the electron at the aqueous/air interface, which appears to migrate away from the surface both in calculation and now experiment too.

Probing this behaviour is a straightforward extension of the methods here, requiring very little experimental change, other than to add a layer of hydrocarbon to the liquid surface. Provided the hydrocarbon layer is thin, the overlap of ω_1 and ω_2 will not be displaced much, so initial tests using a hydrocarbon monolayer may prove sufficient. Evaporation of the hydrocarbon may prove problematic, so higher molecular weight molecules could be trialled first to preserve experimental stability. Initial work using an aliphatic hydrocarbon monolayer, n-dodecane, above phenolate solution showed electron SFG signal. However, the immiscibility of the two solvents likely prevented a true monolayer forming to give proper surface coverage. Studies using decan-1-ol were planned in which the decanol was expected to orient favourably at the surface and form a complete monolayer. The effect an aliphatic versus a cyclic hydrocarbon would have on the propensity of an electron to solvate at the interface is unclear, and perhaps a cyclic alcohol would be a better analogue.

The improved interfacial solvation or migration to the interface should manifest in the SFG signal observed. Either a reduction in the decay rate of the SFG signal may be observed, or if there is substantial migration from hydrated electrons generated in the bulk, the long-term signal may even rise.

The effect that residual phenoxyl radical would have on the dynamics is unclear however, as well as unexcited phenolate anions, which may interfere with the anticipated behaviour. It may be that for these studies a 'cleaner' way of generating the electron is required, such as by two-photon ionisation of water, which may require greater pump powers than accessible here.

7.1.2. Orientation of the Electron:Radical Contact Pair

As explained previously, the ability for SFG to discern chemical orientation at an interface gives access to highly detailed information about an interfacial system. This has been used extensively for steady-state SFG measurements, and some time-resolved studies have used this information to observe orientational motion such as rotational relaxation after photoexcitation.[92] Understanding the structure of the hydrated electron at an interface, and comparing it accurately to theory, requires good knowledge on where the electron is located with respect to the interface. The exact depth at which the interfacial electron is located is still debated, however the parent anion or neutral's position is generally well known. As has been seen in a study on the photo-detachment of surface iodide, the orientation of the contact pair can be inferred via the polarisation configurations of the fundamental and SFG probe fields.[134] The interpretation is simplified considering the atomistic nature of iodide, however a similar analysis might be performed for the contact pair formed from phenolate. Furthermore, given the orientation of phenolate at the air/water interface, it might be interesting to see if the observed orientation or the ensuing contact pair is somehow dependent on the pump polarisation direction, which may indicate a directional ejection of the electron.

7.1.3. Observation of Excited States and Stimulated Emission Transitions

Most VSFG studies in the IR region are resonant with vibrations across all the molecules in a system, which can be difficult to disentangle if the probe region is not specific enough to distinguish each species. This is especially true for time-resolved studies in which the solvent changes may not directly represent the key photodynamics of a system. Therefore, it can be difficult to directly observe electronic excited states, and studies thus far have observed ground state bleaches rather than the appearance of new electronic transients.[205] Direct observation of electronic excited states at the aqueous/air interface could be achieved by selecting a molecule or system with either a large hyperpolarisability (ideally of its first excited state also), a strong excited state absorption, or both, to maximise the resonant signal obtained.

Preliminary investigation was carried out on the molecule 2-methyl-6-(4-dimethylaminostyryl)-4H-pyran (DCM), which is known to have a very large excited state absorption.[206,207] Observation of a ground state bleach was observed from the interface of a solution/air interface of DCM in a water/methanol solution (90:10 by volume, respectively). Probing in the region of 450 nm would be expected to be resonant with the $S_n \leftarrow S_1$ transition (in methanol solvent), revealing the transient excited state population (assuming a small spectral shift at the interface). Furthermore, it is possible to be resonant with an emission transition too, where DCM may be a promising system because of its Stokes shift. The choice of solvent allows tuning, as DCM exhibits a large solvatochromic shift,[206] which is indication that solvation of the excited state has large effects on the electronic structure; therefore, it will be interesting to see what effect interfacial solvation has. A system such as this would also help to benchmark what transitions are visible in typical ESFG setups, and could be combined with calculations in order to predict the size of resonances based on the associated transition dipoles and hyperpolarisabilities. The ability to obtain resonant ESFG signal from both absorptive and emissive transitions would be an interesting prospect, and would further progress SFG as the surface analogue of TA.

7.2. Experimental Advancements

7.2.1. Broadband Electronic Sum-Frequency Generation

An obvious goal from the work presented in chapter 6 is the extension to broadband TR-ESFG, using a broadband field as either ω_1 or ω_2 (and thus ω_{SFG} too), which can enable a vast array more information to be captured in the same experimental timeframe. In VSFG studies, typically ω_2 is the broadband field, generated from an OPA, which has the spectral range to span all the IR frequencies of interest. For electronic transitions, which are generally much broader in energy, this approach may not provide a suitable range in ω_{SFG} after mixing. The alternative is to use a broadband ω_1 that spans the transitions of interest or is wide enough so that the SFG probe is. High intensity pulses are key to efficient SFG, and broadband continua in the visible often have low peak intensity. However, high power supercontinua in the visible region can be generated via optical fibers, either using the Stokes or anti-Stokes broadened continua as possible sources. Furthermore, by pulse compression, such broadband sources can result in ultrashort pulses on the femtosecond timescale, which may permit a very narrow temporal resolution for time-resolved measurements.

The resultant spectral window of ω_{SFG} must be considered carefully, as for larger systems resonances become increasingly congested deeper into the UV. The larger the spectral ranges used, the more care must be taken to properly consider overlapping resonances, or risk difficulty in deconvoluting and interpreting data.

If the OKG system is maintained, some improvements may be welcome. The setup is, in general, broadband, however the lenses used are prone to chromatic aberration, so switching to parabolic mirrors may prove advantageous both for better broadband focussing, and to reduce group velocity dispersion after the sample (group velocity dispersion before the sample may be handled with chirp-correcting mirrors, for example). The dispersion before the Kerr gate is important to ensure maximum bandwidth when gating, or else leading- or trailing wavelengths will miss the gate duration if it is kept short. Switching to a collinear geometry (of the gate and probe) may enable retention of the high gating efficiency whilst lowering the necessary gate power needed to maintain this too, which would reduce the luminescence seen from the gate. A collinear geometry would require separation of the gate wavelength before detection, however this may not be a problem for a broadband detector such as a multi-channel PMT required to obtain broad spectral data.

Generation of the required fields would be benefitted substantially by a laser system outputting higher peak powers per pulse. The use of a 1026 nm seed gives access to convenient harmonic wavelengths, though for pump excitation this may be better served in future by an OPA configured to output in the visible/UV. This would open up the opportunity to pump molecules into different excited states, especially dyes in the visible, or carefully tune the excitation wavelength to see the effects on the resulting dynamics, like for bulk phenolate. Furthermore, higher pump powers may enable observation of the interfacial hydrated electron from two-photon ionisation of water, in which the dynamics of the electron would be unperturbed by the presence of the parent radical, and would make for a compelling study.

7.2.2. Phase Sensitivity

Finally, it would be remiss not to mention expansion to phase-resolved measurements. The work presented here has relied on detecting the SFG intensity and inferring the surface concentration or molecular orientation through a number of assumptions. These assumptions are generally good, especially for single on-resonance wavelengths at the aqueous/air interface. Directly recovering $\mathrm{Im}(\chi^{(2)})$ is undisputedly a more transparent approach, however.

Additionally, this would help to suppress the fluorescence background, and it is unclear if the OKG configuration would be necessary with phase-sensitive methods.

As mentioned in Chapter 4, it is believed the OKG is compatible with phase-delay-type heterodyne measurements, though multiplex methods may prove more difficult. The collinear setup of ω_1 and ω_2 would make a reference placed before the surface in a tandem configuration very straightforward, though switching to a configuration where the fundamental fields are not collinear may also be viable. This development may prove a significant undertaking, however the additional molecular information obtained would likely be highly valuable.

These represent only some of the potential studies and improvements proposed over the course of this project that were not explored in the time available. Indeed, the range of experiments and developments proposed above serve to highlight the depth of information available to explore via surface ESFG spectroscopy. It is hoped the work here will encourage more surface ESFG studies to complement the information accessed by VSFG, and to move towards ESFG as the interface-specific analogue of TA.

References

1. Ruiz-Lopez, M. F., Francisco, J. S., Martins-Costa, M. T. C. & Anglada, J. M. Molecular reactions at aqueous interfaces. *Nat. Rev. Chem.* **4**, 459–475 (2020).
2. Li, Y., Mehari, T. F., Wei, Z., Liu, Y. & Cooks, R. G. Reaction acceleration at air-solution interfaces: Anisotropic rate constants for Katritzky transamination. *J. Mass Spectrom.* **56**, e4585 (2021).
3. Bain, R. M., Pulliam, C. J., Thery, F. & Cooks, R. G. Accelerated Chemical Reactions and Organic Synthesis in Leidenfrost Droplets. *Angew. Chemie Int. Ed.* **55**, 10478–10482 (2016).
4. Remacle, F. & Levine, R. D. An electronic time scale in chemistry. *Proc. Natl. Acad. Sci. U. S. A.* **103**, 6793–6798 (2006).
5. Griffiths, D. J. *Introduction to Electrodynamics*. (Prentice Hall, 1999).
6. Atkins, P. & de Paula, J. *Atkins' Physical Chemistry*. (Oxford University Press, 2006).
7. Hollas, J. M. *Modern spectroscopy Fourth Edition*. *John Wiley & Sons Ltd* (2004).
8. Atkins, P. & Friedman, R. Molecular Quantum Mechanics Fourth Edition. *Oxford Univ. Press New York* (2005).
9. Griffiths, D. J. *Introduction to Quantum Mechanics*. (Prentice Hall, 1995).
10. Burland, D. M. & Robinson, G. W. Is the Breakdown of the Born-Oppenheimer Approximation Responsible for Internal Conversion in Large Molecules? *Proc. Natl. Acad. Sci.* **66**, 257–264 (1970).
11. Mayerhöfer, T. G., Mutschke, H. & Popp, J. Employing Theories Far beyond Their Limits—The Case of the (Boguer-) Beer–Lambert Law. *ChemPhysChem* **17**, 1948–1955 (2016).
12. Guo, J., Ohkita, H., Benten, H. & Ito, S. Near-IR femtosecond transient absorption spectroscopy of ultrafast polaron and triplet exciton formation in polythiophene films

with different regioregularities. *J. Am. Chem. Soc.* **131**, 16869–16880 (2009).

13. Warrick, E. R. *et al.* Attosecond transient absorption spectroscopy of molecular nitrogen: Vibrational coherences in the b′ 1Σ+u state. *Chem. Phys. Lett.* **683**, 408–415 (2017).

14. Beck, A. R., Neumark, D. M. & Leone, S. R. Probing ultrafast dynamics with attosecond transient absorption. *Chem. Phys. Lett.* **624**, 119–130 (2015).

15. Peng, P. *et al.* Coherent control of ultrafast extreme ultraviolet transient absorption. *Nat. Photonics* **16**, 45–51 (2022).

16. Fushitani, M. Applications of pump-probe spectroscopy. *Annu. Reports Prog. Chem. - Sect. C* **104**, 272–297 (2008).

17. Loring, R. F., Yan, Y. J. & Mukamel, S. Time-resolved fluorescence and hole-burning line shapes of solvated molecules: Longitudinal dielectric relaxation and vibrational dynamics. *J. Chem. Phys.* **87**, 5840–5857 (1987).

18. Kovalenko, S. A., Ruthmann, J. & Ernsting, N. P. Ultrafast stokes shift and excited-state transient absorption of coumarin 153 in solution. *Chem. Phys. Lett.* **271**, 40–50 (1997).

19. Debus, B. *et al.* Fusion of Ultraviolet-Visible and Infrared Transient Absorption Spectroscopy Data to Model Ultrafast Photoisomerization. *J. Phys. Chem. Lett.* **8**, 3530–3535 (2017).

20. Tahara, S. *et al.* Ultrafast Dynamics of Heliorhodopsins. *J. Phys. Chem. B* **123**, 2507–2512 (2019).

21. Bull, J. N. *et al.* Ultrafast photoisomerisation of an isolated retinoid. *Phys. Chem. Chem. Phys.* **21**, 10567–10579 (2019).

22. Jarzęba, W., Walker, G. C., Johnson, A. E., Kahlow, M. A. & Barbara, P. F. Femtosecond microscopic solvation dynamics of aqueous solutions. *J. Phys. Chem.* **92**, 7039–7041 (1988).

23. Jimenez, R., Fleming, G. R., Kumar, P. V. & Maroncelli, M. Femtosecond solvation dynamics of water. *Nature* **369**, 471–473 (1994).

24. Stähler, J., Bovensiepen, U., Meyer, M. & Wolf, M. A surface science approach to ultrafast electron transfer and solvation dynamics at interfaces. *Chem. Soc. Rev.* **37**, 2180–2190 (2008).

25. Yoneda, Y. *et al.* Vibrational coherence in ultrafast electron transfer reaction observed by broadband transient absorption spectroscopy. *EPJ Web Conf.* **205**, 09028 (2019).

26. Limpert, J., Röser, F., Schreiber, T. & Tünnermann, A. High-power ultrafast fiber laser systems. *IEEE J. Sel. Top. Quantum Electron.* **12**, 233–244 (2006).

27. Backus, S., Durfee, C. G., Murnane, M. M. & Kapteyn, H. C. High power ultrafast lasers. *Review of Scientific Instruments* vol. 69 1207–1223 (1998).

28. Boyd, R. W. *Nonlinear Optics*. *Nonlinear Optics* (Academic Press, 2008).

29. Brevet, P.-F. *Surface Second Harmonic Generation*. (Presses Polytechniques et Universitaires Romandes, 1997).

30. Buckingham, A. D. & Long, D. A. Polarizability and Hyperpolarizability. *Philos. Trans. R. Soc. London. Ser. A, Math. Phys. Sci.* **293**, 239–248 (1979).

31. Ibach, H. & Lüth, H. *Solid-State Physics: An Introduction to Principles of Materials Science*. (Springer Verlach, 2010).

32. Bain, C. D. Sum-frequency vibrational spectroscopy of the solid/liquid interface. *J. Chem. Soc. Faraday Trans.* **91**, 1281–1296 (1995).

33. Weiner, J. & HO, P. T. *Light-Matter Interaction*. (John Wiley & Sons, 2003).

34. Maiman, T. H. Stimulated optical radiation in Ruby. *Nature* **187**, 493–494 (1960).

35. Franken, P. A., Hill, A. E., Peters, C. W. & Weinreich, G. Generation of optical harmonics. *Phys. Rev. Lett.* **7**, 118–119 (1961).

36. Bass, M., Franken, P. A., Hill, A. E., Peters, C. W. & Weinreich, G. Optical mixing. *Phys. Rev. Lett.* **8**, 18 (1962).

37. Butcher, P. N. & Cotter, D. *The Elements of Nonlinear Optics*. (Cambridge University Press, 1990).

38. Bass, M., Franken, P. A., Ward, J. F. & Weinreich, G. Optical rectification. *Phys. Rev. Lett.* **9**, 446–448 (1962).

39. Dou, Q. *et al.* Study of the second harmonic generation and optical rectification in a cBN crystal. *Quantum Electron.* **37**, 158–161 (2007).

40. Bloembergen, N. Wave Propagation in Nonlinear Electromagnetic Media. *Proc. IEEE* **51**, 124–131 (1963).

41. Rasing, T., Shen, Y. R., Kim, M. W. & Grubb, S. Observation of molecular reorientation at a two-dimensional-liquid phase transition. *Phys. Rev. Lett.* **55**, 2903–2906 (1985).

42. Levine, B. F. & Bethea, C. G. Absolute signs of hyperpolarizabilities in the liquid state. *J. Chem. Phys.* **60**, 3856–3858 (1974).

43. Wang, H. F., Gan, W., Lu, R., Rao, Y. & Wu, B. H. Quantitative spectral and orientational analysis in surface sum frequency generation vibrational spectroscopy (SFG-VS). *International Reviews in Physical Chemistry* vol. 24 191–256 (2005).

44. Kleinman, D. A. Nonlinear dielectric polarization in optical media. *Phys. Rev.* **126**, 1977–1979 (1962).

45. Wagnière, G. Theoretical investigation of Kleinman symmetry in molecules. *Appl. Phys. B Photophysics Laser Chem.* **41**, 169–172 (1986).

46. Dailey, C. A., Burke, B. J. & Simpson, G. J. The general failure of Kleinman symmetry in practical nonlinear optical applications. *Chem. Phys. Lett.* **390**, 8–13 (2004).

47. Bloembergen, N., Chang, R. K., Jha, S. S. & Lee, C. H. Optical second-harmonic generation in reflection from media with inversion symmetry. *Phys. Rev.* **174**, 813–822 (1968).

48. Sipe, J. E., Moss, D. J. & Van Driel, H. M. Phenomenological theory of optical second- and third-harmonic generation from cubic centrosymmetric crystals. *Phys. Rev. B* **35**, 1129–1141 (1987).

49. Alejo-Molina, A., Hardhienata, H. & Hingerl, K. Simplified bond-hyperpolarizability model of second harmonic generation, group theory, and Neumann's principle. *J. Opt. Soc. Am. B* **31**, 526–533 (2014).

50. Guyot-Sionnest, P., Chen, W. & Shen, Y. R. General considerations on optical second-harmonic generation from surfaces and interfaces. *Phys. Rev. B* **33**, 8254–8263 (1986).

51. Bloembergen, N. & Pershan, P. S. Light waves at the boundary of nonlinear media. *Phys. Rev.* **128**, 606–622 (1962).

52. Feynman, R., Leighton, R. & Sands, M. *The Feynman lectures on Physics, Volume II: Mainly Electromagnetism and Matter*. (Basic Books, 2010).

53. Hecht, E. *Optics*. (Pearson, 2017).

54. Armstrong, J. A., Bloembergen, N., Ducuing, J. & Pershan, P. S. Interactions between

light waves in a nonlinear dielectric. *Phys. Rev.* **127**, 1918–1939 (1962).

55. Heinz, T. F. Nonlinear Optics of Surfaces and Adsorbates. (University of California, 1982).

56. Shen, Y. R. *Principles of Nonlinear Optics*. *Principles of Nonlinear Optics* (2002).

57. Shen, Y. Optical Second Harmonic Generation At Interfaces. *Annu. Rev. Phys. Chem.* **40**, 327–350 (1989).

58. Terhune, R. W., Maker, P. D. & Savage, C. M. Optical harmonic generation in calcite. *Phys. Rev. Lett.* **8**, 404–406 (1962).

59. Guyot-Sionnest, P. & Shen, Y. R. Bulk contribution in surface second-harmonic generation. *Phys. Rev. B* **28**, 7985–7989 (1988).

60. Tom, H. W. K., Heinz, T. F. & Shen, Y. R. Second-harmonic reflection from silicon surfaces and its relation to structural symmetry. *Phys. Rev. Lett.* **51**, 1983–1986 (1983).

61. Koos, D. A., Shannon, V. L. & Richmond, G. L. Surface-dipole and electric-quadrupole contributions to anisotropic second-harmonic generation from noble-metal surfaces. *Phys. Rev. B* **47**, 4730–4734 (1993).

62. Guyot-Sionnest, P. & Shen, Y. R. Local and nonlocal surface nonlinearities for surface optical second-harmonic generation. *Phys. Rev. B* **35**, 4420–4426 (1987).

63. Heinz, T. F., Chen, C. K., Ricard, D. & Shen, Y. R. Spectroscopy of molecular monolayers by resonant second-harmonic generation. *Phys. Rev. Lett.* **48**, 478–481 (1982).

64. Zhang, W. K. *et al.* Reconsideration of second-harmonic generation from isotropic liquid interface: Broken Kleinman symmetry of neat air/water interface from dipolar contribution. *J. Chem. Phys.* **123**, 224713 (2005).

65. Superfine, R., Huang, J. Y. & Shen, Y. R. Phase measurement for surface infrared–visible sum-frequency generation. *Opt. Lett.* **15**, 1276–1278 (1990).

66. Shen, Y. R. Phase-Sensitive Sum-Frequency Spectroscopy. *Annu. Rev. Phys. Chem.* **64**, 129–150 (2013).

67. Simon, H. J., Mitchell, D. E. & Watson, J. G. Optical Second-Harmonic Generation with Surface Plasmons in Silver Films. *Phys. Rev. Lett.* **33**, 1531–1534 (1974).

68. Fleischmann, M., Hendra, P. J. & McQuillan, A. J. Raman spectra of pyridine adsorbed at a silver electrode. *Chem. Phys. Lett.* **26**, 163–166 (1974).

69. Chen, C. K., De Castro, A. R. B. & Shen, Y. R. Surface-enhanced second-harmonic generation. *Phys. Rev. Lett.* **46**, 145–148 (1981).

70. Boyd, G. T., Rasing, T., Leite, J. R. R. & Shen, Y. R. Local-field enhancement on rough surfaces of metals, semimetals, and semiconductors with the use of optical second-harmonic generation. *Phys. Rev. B* **30**, 519–526 (1984).

71. Heinz, T. F., Loy, M. M. T. & Thompson, W. A. Study of Si(111) surfaces by optical second-harmonic generation: Reconstruction and surface phase transformation. *Phys. Rev. Lett.* **54**, 63–66 (1985).

72. Tom, H. W. K. *et al.* Surface studies by optical second-harmonic generation: The adsorption of O2, CO, and sodium on the Rh(111) surface. *Phys. Rev. Lett.* **52**, 348–351 (1984).

73. Boyd, G. T., Hänsch, T. W. & Shen, Y. R. Continuous-wave second-harmonic generation as a surface microprobe. *Opt. Lett.* **11**, 97–99 (1986).

74. Richmond, G. L., Robinson, J. M. & Shannon, V. L. Second harmonic generation studies of interfacial structure and dynamics. *Prog. Surf. Sci.* **28**, 1–70 (1988).

75. Chen, C. K., Heinz, T. F., Ricard, D. & Shen, Y. R. Detection of molecular monolayers by optical second-harmonic generation. *Phys. Rev. Lett.* **46**, 1010–1012 (1981).

76. Zhu, X. D., Suhr, H. & Shen, Y. R. Surface vibrational spectroscopy by infrared-visible sum frequency generation. *Phys. Rev. B* **35**, 3047–3050 (1987).

77. Messmer, M. C., Conboy, J. C. & Richmond, G. L. Observation of Molecular Ordering at the Liquid-Liquid Interface by Resonant Sum Frequency Generation. *J. Am. Chem. Soc.* **117**, 8039–8040 (1995).

78. Hunt, J. H., Guyot-Sionnest, P. & Shen, Y. R. Observation of C-H stretch vibrations of monolayers of molecules optical sum-frequency generation. *Chem. Phys. Lett.* **133**, 189–192 (1987).

79. Miranda, P. B. & Shen, Y. R. Liquid interfaces: A study by sum-frequency vibrational spectroscopy. *J. Phys. Chem. B* **103**, 3292–3307 (1999).

80. Du, Q., Superfine, R., Freysz, E. & Shen, Y. R. Vibrational spectroscopy of water at the

vapor/water interface. *Phys. Rev. Lett.* **70**, 2313–2316 (1993).

81. Superfine, R., Huang, J. Y. & Shen, Y. R. Nonlinear optical studies of the pure liquid/vapor interface: Vibrational spectra and polar ordering. *Phys. Rev. Lett.* **66**, 1066–1069 (1991).

82. Wei, X., Hong, S. C., Lvovsky, A. I., Held, H. & Shen, Y. R. Evaluation of surface vs bulk contributions in sum-frequency vibrational spectroscopy using reflection and transmission geometries. *J. Phys. Chem. B* **104**, 3349–3354 (2000).

83. Kemnitz, K. *et al.* The phase of second-harmonic light generated at an interface and its relation to absolute molecular orientation. *Chem. Phys. Lett.* **131**, 285–290 (1986).

84. Chang, R. K., Ducuing, J. & Bloembergen, N. Relative phase measurement between fundamental and second-harmonic light. *Phys. Rev. Lett.* **15**, 6–8 (1965).

85. Stolle, R., Marowsky, G., Schwarzberg, E. & Berkovic, G. Phase measurements in nonlinear optics. *Appl. Phys. B Lasers Opt.* **63**, 491–498 (1996).

86. Nihonyanagi, S. *et al.* Accurate determination of complex $\chi(2)$ spectrum of the air/water interface. *J. Chem. Phys.* **143**, 124707 (2015).

87. Ji, N., Ostroverkhov, V., Chen, C. Y. & Shen, Y. R. Phase-sensitive sum-frequency vibrational spectroscopy and its application to studies of interfacial alkyl chains. *J. Am. Chem. Soc.* **129**, 10056–10057 (2007).

88. Yamaguchi, S. & Tahara, T. Heterodyne-detected electronic sum frequency generation: 'Up' versus 'down' alignment of interfacial molecules. *J. Chem. Phys.* **129**, 101102 (2008).

89. Ostroverkhov, V., Waychunas, G. A. & Shen, Y. R. New information on water interfacial structure revealed by phase-sensitive surface spectroscopy. *Phys. Rev. Lett.* **94**, 046102 (2005).

90. Berkovic, G., Rasing, T. & Shen, Y. R. Study of monolayer polymerization using nonlinear optics. *J. Chem. Phys.* **85**, 7374 (1986).

91. Tom, H. W. K., Aumiller, G. D. & Brito-Cruz, C. H. Time-resolved study of laser-induced disorder of Si surfaces. *Phys. Rev. Lett.* **60**, 1438–1441 (1988).

92. Castro, A., Sitzmann, E. V., Zhang, D. & Eisenthal, K. B. Rotational relaxation at the air/water interface by time-resolved second harmonic generation. *J. Phys. Chem.* **95**,

6752–6753 (1991).

93. Antoine, R., Tamburello-Luca, A. A., Hébert, P., Brevet, P. F. & Girault, H. H. Picosecond dynamics of Eosin B at the air/water interface by time-resolved second harmonic generation: Orientational randomization and rotational relaxation. *Chem. Phys. Lett.* **288**, 138–146 (1998).

94. Shi, X., Borguet, E., Tarnovsky, A. N. & Eisenthal, K. B. Ultrafast dynamics and structure at aqueous interfaces by second harmonic generation. *Chem. Phys.* **205**, 167–178 (1996).

95. Zimdars, D., Dadap, J. I., Eisenthal, K. B. & Heinz, T. F. Femtosecond dynamics of solvation at the air/water interface. *Chem. Phys. Lett.* **301**, 112–120 (1999).

96. Nihonyanagi, S., Singh, P. C., Yamaguchi, S. & Tahara, T. Ultrafast vibrational dynamics of a charged aqueous interface by femtosecond time-resolved heterodyne-detected vibrational sum frequency generation. *Bull. Chem. Soc. Jpn.* **85**, 758–760 (2012).

97. Light Conversion. CARBIDE specifications datasheet.

98. Tyson, A. L. & Verlet, J. R. R. On the Mechanism of Phenolate Photo-Oxidation in Aqueous Solution. *J. Phys. Chem. B* **123**, 2373–2379 (2019).

99. Tyson, A. L. Making a MESS: A Multi-Experiment Spectral Suite to study hydrated electrons. (University of Durham, 2019).

100. Sagar, D. M., Bain, C. D. & Verlet, J. R. R. Hydrated electrons at the water/air interface. *J. Am. Chem. Soc.* **132**, 6917–6919 (2010).

101. Guillén-García, A. *et al.* Allophycocyanin A is a carbon dioxide receptor in the cyanobacterial phycobilisome. *Nat. Commun.* **13**, 1–10 (2022).

102. Dharmadhikari, A. K., Rajgara, F. A. & Mathur, D. Depolarization of white light generated by ultrashort laser pulses in optical media. *Opt. Lett.* **31**, 2184 (2006).

103. Lietard, A. *et al.* A Combined Spectrophotometer and Fluorometer to Demonstrate the Principles of Absorption Spectroscopy. *J. Chem. Educ.* **98**, 3871–3877 (2021).

104. Kovalenko, S. A., Ernsting, N. P. & Ruthmann, J. Femtosecond hole-burning spectroscopy of the dye DCM in solution: The transition from the locally excited to a charge-transfer state. *Chem. Phys. Lett.* **258**, 445–454 (1996).

105. Kovalenko, S. A., Dobryakov, A. L., Ruthmann, J. & Ernsting, N. P. Femtosecond spectroscopy of condensed phases with chirped supercontinuum probing. *Phys. Rev. A - At. Mol. Opt. Phys.* **59**, 2369–2384 (1999).

106. Jordan, C. J. C. & Verlet, J. R. R. Time-resolved electronic sum-frequency generation spectroscopy with fluorescence suppression using optical Kerr gating. *J. Chem. Phys.* **155**, 164202 (2021).

107. Kerr, J. XL. A new relation between electricity and light: Dielectrified media birefringent. *London, Edinburgh, Dublin Philos. Mag. J. Sci.* **50**, 337–348 (1875).

108. Qasymeh, M., Cada, M. & Ponomarenko, S. A. Quadratic electro-optic Kerr effect: Applications to photonic devices. *IEEE J. Quantum Electron.* **44**, 740–746 (2008).

109. Duguay, M. A. & Hansen, J. W. An ultrafast light gate. *Appl. Phys. Lett.* **15**, 192–194 (1969).

110. Tyson, D. G. & Jennings, B. R. Measurement of the 'optical' kerr effect induced by nanosecond laserpulses. *J. Phys. D. Appl. Phys.* **24**, 645–653 (1991).

111. Yu, Z., Gundlach, L. & Piotrowiak, P. Efficiency and temporal response of crystalline Kerr media in collinear optical Kerr gating. *Opt. Lett.* **36**, 2904 (2011).

112. Ho, P. P., Lu, P. Y. & Alfano, R. R. Observation of broadened and oscillatory optically induced Kerr kinetics in neat liquids. *Phys. Rev. A* **21**, 1730–1734 (1980).

113. Meyer, H. J., Sharonov, M. & Alfano, R. R. Ultra-high intensity temporally oscillatory optical Kerr effect in Carbon Disulfide arising from electronic and molecular distortions. *Opt. Commun.* **524**, 128806 (2022).

114. Ippen, E. P. & Shank, C. V. Picosecond response of a high-repetition-rate CS2 optical Kerr gate. *Appl. Phys. Lett.* **26**, 92–93 (1975).

115. Appavoo, K. & Sfeir, M. Y. Enhanced broadband ultrafast detection of ultraviolet emission using optical Kerr gating. *Rev. Sci. Instrum.* **85**, 055114 (2014).

116. Philip, J. & Rao, T. A. P. Kerr effect studies in acetonitrile-aromatic hydrocarbon systems. *J. Mol. Liq.* **50**, 115–124 (1991).

117. Aroney, M. J., Huang, H. H., Le Fèvre, R. J. W. & Ritchie, G. L. D. Molecular polarisability. The molar Kerr constants and anisotropic polarisabilities of certain aromatic nitro-compounds. *J. Chem. Soc. B Phys. Org.* **0**, 416–420 (1966).

118. Fita, P., Punzi, A. & Vauthey, E. Local viscosity of binary water+glycerol mixtures at liquid/liquid interfaces probed by time-resolved surface second harmonic generation. *J. Phys. Chem. C* **113**, 20705–20712 (2009).

119. Nowakowski, P. J., Woods, D. A., Bain, C. D. & Verlet, J. R. R. Time-resolved phase-sensitive second harmonic generation spectroscopy. *J. Chem. Phys.* **142**, 084201 (2015).

120. Tyson, A. L., Woods, D. A. & Verlet, J. R. R. Time-resolved second harmonic generation with single-shot phase sensitivity. *J. Chem. Phys.* **149**, 204201 (2018).

121. Qian, Y., Deng, G. H. & Rao, Y. In Situ Spectroscopic Probing of Polarity and Molecular Configuration at Aerosol Particle Surfaces. *J. Phys. Chem. Lett.* **11**, 6763–6771 (2020).

122. Punzi, A., Martin-Gassin, G., Grilj, J. & Vauthey, E. Effect of salt on the excited-state dynamics of malachite green in bulk aqueous solutions and at air/water interfaces: A femtosecond transient absorption and surface second harmonic generation study. *J. Phys. Chem. C* **113**, 11822–11829 (2009).

123. Sen, P., Yamaguchi, S. & Tahara, T. Ultrafast dynamics of malachite green at the air/water interface studied by femtosecond time-resolved electronic sum frequency generation (TR-ESFG): An indicator for local viscosity. *Faraday Discuss.* **145**, 411–428 (2010).

124. Kikteva, T., Star, D. & Leach, G. W. Optical Second Harmonic Generation Study of Malachite Green Orientation and Order at the Fused-Silica/Air Interface. *J. Phys. Chem. B* **104**, 2860–2867 (2000).

125. Lü, R., Gan, W. & Wang, H. Novel method for accurate determination of the orientational angle of interfacial chemical groups. *Chinese Sci. Bull.* **48**, 2183–2187 (2003).

126. Mitchell, S. A. Nonlinear susceptibility of a cyanobiphenyl derivative at the air/water interface: Improved measurement of molecular orientation by optical second harmonic generation. *J. Phys. Chem. B* **110**, 883–890 (2006).

127. Zhang, W. K., Wang, H. F. & Zheng, D. S. Quantitative measurement and interpretation of optical second harmonic generation from molecular interfaces. *Phys. Chem. Chem. Phys.* **8**, 4041–4052 (2006).

128. Heinz, T. F., Tom, H. W. K. & Shen, Y. R. Determination of molecular orientation of

monolayer adsorbates by optical second-harmonic generation. *Phys. Rev. A* **28**, 1883–1885 (1983).

129. Zhuang, X., Miranda, P. B., Kim, D. & Shen, Y. R. Mapping molecular orientation and conformation at interfaces by surface nonlinear optics. *Phys. Rev. B - Condens. Matter Mater. Phys.* **59**, 12632–12640 (1999).

130. Simpson, G. J. & Rowlen, K. L. An SHG magic angle: Dependence of second harmonic generation orientation measurements on the width of the orientation distribution. *J. Am. Chem. Soc.* **121**, 2635–2636 (1999).

131. Cannizzo, A. *et al.* Broadband femtosecond fluorescence spectroscopy of [Ru(bpy) 3]2+. *Angew. Chemie - Int. Ed.* **45**, 3174–3176 (2006).

132. Gerecke, M., Bierhance, G., Gutmann, M., Ernsting, N. P. & Rosspeintner, A. Femtosecond broadband fluorescence upconversion spectroscopy: Spectral coverage versus efficiency. *Rev. Sci. Instrum.* **87**, (2016).

133. Lietard, A. & Verlet, J. R. R. Selectivity in Electron Attachment to Water Clusters. *J. Phys. Chem. Lett* **10**, 27 (2019).

134. Nowakowski, P. J., Woods, D. A. & Verlet, J. R. R. Charge Transfer to Solvent Dynamics at the Ambient Water/Air Interface. *J. Phys. Chem. Lett.* **7**, 4079–4085 (2016).

135. Dobson, G. & Grossweiner, L. I. Flash photolysis of aqueous phenol and cresols. *Trans. Faraday Soc.* **61**, 708–714 (1965).

136. Grossweiner, L. I. & Joschek, H.-I. Optical Generation of Hydrated Electrons from Aromatic Compounds. in *Solvated Electron* (ed. Hart, E.) 279–288 (American Chemical Society, 1965).

137. Joschek, H. I. & Grossweiner, L. I. Organic and Biological Chemistry Optical Generation of Hydrated Electrons from Aromatic Compounds. II. *J. Am. Chem. Soc.* **88**, 3261–3268 (1966).

138. Matheson, M. S., Mulac, W. A. & Rabani, J. Formation of the Hydrated Electron in the Flash Photolysis of Aqueous Solutions 1. *J. Phys. Chem.* **67**, 2613–2617 (1963).

139. Shirom, M. & Stein, G. Excited state chemistry of the ferrocyanide ion in aqueous solution. I. Formation of the hydrated electron. *J. Chem. Phys.* **55**, 3459–3467 (1971).

140. Anstöter, C. S. & Verlet, J. R. R. A Hückel Model for the Excited-State Dynamics of a Protein Chromophore Developed Using Photoelectron Imaging. *Acc. Chem. Res.* **55**, 1205–1213 (2022).

141. Lincke, K. *et al.* On the absorption of the phenolate chromophore in the green fluorescent protein - Role of individual interactions. *Chem. Commun.* **46**, 734–736 (2010).

142. Tseng, C. M., Lee, Y. T., Ni, C. K. & Chang, J. L. Photodissociation dynamics of the chromophores of the amino acid tyrosine: P-methylphenol, p-ethylphenol, and p(2-aminoethyl)phenol. *J. Phys. Chem. A* **111**, 6674–6678 (2007).

143. Oliver, T. A. A., Zhang, Y., Roy, A., Ashfold, M. N. R. & Bradforth, S. E. Exploring Autoionization and Photoinduced Proton-Coupled Electron Transfer Pathways of Phenol in Aqueous Solution. *J. Phys. Chem. Lett.* **6**, 4159–4164 (2015).

144. Rayne, S., Forest, K. & Friesen, K. J. Mechanistic aspects regarding the direct aqueous environmental photochemistry of phenol and its simple halogenated derivatives. A review. *Environ. Int.* **35**, 425–437 (2009).

145. Chen, X., Larsen, D. S., Bradforth, S. E. & Van Stokkum, I. H. M. Broadband Spectral Probing Revealing Ultrafast Photochemical Branching after Ultraviolet Excitation of the Aqueous Phenolate Anion. *J. Phys. Chem. A* **115**, 3807–3819 (2011).

146. Robertson, K. *et al.* Wavelength dependent mechanism of phenolate photooxidation in aqueous solution. *Chem. Sci.* (2023) doi:10.1039/D3SC00016H.

147. Blandamer, M. J. & Fox, M. F. Theory and applications of charge-transfer-to-solvent spectra. *Chem. Rev.* **70**, 59–93 (1970).

148. Kloepfer, J. A., Vilchiz, V. H., Lenchenkov, V. A., Germaine, A. C. & Bradforth, S. E. The ejection distribution of solvated electrons generated by the one-photon photodetachment of aqueous I− and two-photon ionization of the solvent. *J. Chem. Phys.* **113**, 6288–6307 (2000).

149. Kusaka, R., Nihonyanagi, S. & Tahara, T. The photochemical reaction of phenol becomes ultrafast at the air–water interface. *Nat. Chem.* **13**, 306–311 (2021).

150. Matsuzaki, K. *et al.* Partially Hydrated Electrons at the Air/Water Interface Observed by UV-Excited Time-Resolved Heterodyne-Detected Vibrational Sum Frequency Generation Spectroscopy. *J. Am. Chem. Soc.* **138**, 7551–7557 (2016).

151. Wraight, C. A. Chance and design-Proton transfer in water, channels and bioenergetic proteins. *Biochim. Biophys. Acta - Bioenerg.* **1757**, 886–912 (2006).

152. Turi, L. & Rossky, P. J. Theoretical studies of spectroscopy and dynamics of hydrated electrons. *Chem. Rev.* **112**, 5641–5674 (2012).

153. Ishiyama, T., Tahara, T. & Morita, A. Why the Photochemical Reaction of Phenol Becomes Ultrafast at the Air-Water Interface: The Effect of Surface Hydration. *J. Am. Chem. Soc.* **144**, 6321–6325 (2022).

154. Jou, F. Y. & Freeman, G. R. Temperature and isotope effects on the shape of the optical absorption spectrum of solvated electrons in water. *J. Phys. Chem.* **83**, 2383–2387 (1979).

155. Jacobson, L. D. & Herbert, J. M. Polarization-bound quasi-continuum states are responsible for the 'blue tail' in the optical absorption spectrum of the aqueous electron. *J. Am. Chem. Soc.* **132**, 10000–10002 (2010).

156. Land, E. J. & Porter, G. Primary photochemical processes in aromatic molecules. Part 8. -Absorption spectra and acidity constants of anilino radicals. *Trans. Faraday Soc.* **59**, 2027–2037 (1963).

157. Radziszewski, J. G. *et al.* Electronic states of the phenoxyl radical. *J. Chem. Phys.* **115**, 9733–9738 (2001).

158. Zhang, Y., Oliver, T. A. A., Ashfold, M. N. R. & Bradforth, S. E. Contrasting the excited state reaction pathways of phenol and para-methylthiophenol in the gas and liquid phases. *Faraday Discuss.* **157**, 141–163 (2012).

159. Rao, Y., Subir, M., McArthur, E. A., Turro, N. J. & Eisenthal, K. B. Organic ions at the air/water interface. *Chem. Phys. Lett.* **477**, 241–244 (2009).

160. Savolainen, J., Uhlig, F., Ahmed, S., Hamm, P. & Jungwirth, P. Direct observation of the collapse of the delocalized excess electron in water. *Nat. Chem.* **6**, 697–701 (2014).

161. Staib, A. & Borgis, D. Reaction pathways in the photodetachment of an electron from aqueous chloride: A quantum molecular dynamics study. *J. Chem. Phys.* **104**, 9027–9039 (1996).

162. Borgis, D. & Staib, A. Quantum adiabatic umbrella sampling: The excited state free energy surface of an electron-atom pair in solution. *J. Chem. Phys.* **104**, 4776–4783

(1996).

163. Coutinho, K., Cabral, B. J. C. & Canuto, S. Can larger dipoles solvate less? solute-solvent hydrogen bond and the differential solvation of phenol and phenoxy. *Chem. Phys. Lett.* **399**, 534–538 (2004).

164. Hardt, S. L. Rates of diffusion controlled reactions in one, two and three dimensions. *Biophys. Chem.* **10**, 239–243 (1979).

165. Chen, W. *et al.* The static polarizability and first hyperpolarizability of the water trimer anion: Ab initio study. *J. Chem. Phys.* **121**, 10489–10494 (2004).

166. Madarász, Á., Rossky, P. J. & Turi, L. Excess electron relaxation dynamics at water/air interfaces. *J. Chem. Phys.* **126**, 234707 (2007).

167. Dixon, R. N., Oliver, T. A. A. & Ashfold, M. N. R. Tunnelling under a conical intersection: Application to the product vibrational state distributions in the UV photodissociation of phenols. *J. Chem. Phys.* **134**, 194303 (2011).

168. Tseng, C. M., Lee, Y. T. & Ni, C. K. H atom elimination from the πσ* state in the photodissociation of phenol. *J. Chem. Phys.* **121**, 2459–2461 (2004).

169. Sobolewski, A. L. & Domcke, W. Photoinduced electron and proton transfer in phenol and its clusters with water and ammonia. *J. Phys. Chem. A* **105**, 9275–9283 (2001).

170. Granucci, G., Hynes, J. T., Millié, P. & Tran-Thi, T. H. A theoretical investigation of excited-state acidity of phenol and cyanophenols. *J. Am. Chem. Soc.* **122**, 12243–12253 (2000).

171. Debnath, T., Mohd Yusof, M. S. Bin, Low, P. J. & Loh, Z. H. Ultrafast structural rearrangement dynamics induced by the photodetachment of phenoxide in aqueous solution. *Nat. Commun.* **10**, 1–8 (2019).

172. Getoff, N. A review of the relationship between Qe-aq and QF of excited compounds in aqueous solution. *Int. J. Radiat. Appl. Instrum.* **34**, 711–719 (1989).

173. Rizzuto, A. M., Irgen-Gioro, S., Eftekhari-Bafrooei, A. & Saykally, R. J. Broadband Deep UV Spectra of Interfacial Aqueous Iodide. *J. Phys. Chem. Lett.* **7**, 3882–3885 (2016).

174. Jordan, C. J. C., Lowe, E. A. & Verlet, J. R. R. Photooxidation of the Phenolate Anion is Accelerated at the Water/Air Interface. *J. Am. Chem. Soc.* **144**, 14012–14015 (2022).

175. Fee, R. S. & Maroncelli, M. Estimating the time-zero spectrum in time-resolved emmsion measurements of solvation dynamics. *Chem. Phys.* **183**, 235–247 (1994).

176. Maroncelli, M. The dynamics of solvation in polar liquids. *J. Mol. Liq.* **57**, 1–37 (1993).

177. Barbara, P. & Jarzeba, W. Ultrafast Photochemical Intramolecular Charge Transfer and Excited State Solvation. in *Advances in Photochemistry, Volume 15* (eds. Volman, D., Hammond, G. & Gollnick, K.) 1–68 (John Wiley & Sons, 2007).

178. Mathies, R. A., Brito Cruz, C. H., Pollard, W. T. & Shank, C. V. Direct observation of the femtosecond excited-state cis-trans isomerization in bacteriorhodopsin. *Science* **240**, 777–779 (1988).

179. Timmers, H. *et al.* Disentangling conical intersection and coherent molecular dynamics in methyl bromide with attosecond transient absorption spectroscopy. *Nat. Commun.* **10**, 1–8 (2019).

180. Zhang, T. *et al.* Spectral Phase Measurements of Heterodyne Detection in Interfacial Broadband Electronic Spectroscopy. *J. Phys. Chem. C* **126**, 2823–2832 (2022).

181. Deng, G. H., Qian, Y. & Rao, Y. Development of ultrafast broadband electronic sum frequency generation for charge dynamics at surfaces and interfaces. *J. Chem. Phys.* **150**, 24708 (2019).

182. Rey, N. G. & Dlott, D. D. Studies of electrochemical interfaces by broadband sum frequency generation. *J. Electroanal. Chem.* **800**, 114–125 (2017).

183. Adamu, A. I. *et al.* Deep-UV to Mid-IR Supercontinuum Generation driven by Mid-IR Ultrashort Pulses in a Gas-filled Hollow-core Fiber. *Sci. Rep.* **9**, (2019).

184. Dubietis, A., Tamošauskas, G., Šuminas, R., Jukna, V. & Couairon, A. Ultrafast supercontinuum generation in bulk condensed media. *Lith. J. Phys.* **57**, 113–157 (2017).

185. Richmond, G. L. Molecular bonding and interactions at aqueous surfaces as probed by vibrational sum frequency spectroscopy. *Chem. Rev.* **102**, 2693–2724 (2002).

186. Spanget-Larsen, J. *et al.* Vibrations of the Phenoxyl Radical. *J. Am. Chem. Soc.* **123**, 11253–11261 (2001).

187. Schuler, R. H. & Buzzard, G. K. Pulse radiolysis experiments: Synthesis and analysis of composite spectra. *Int. J. Radiat. Phys. Chem.* **8**, 563–574 (1976).

188. Hare, P. M., Price, E. A. & Bartels, D. M. Hydrated electron extinction coefficient

revisited. *J. Phys. Chem. A* **112**, 6800–6802 (2008).

189. Verlet, J. R. R., Bragg, A. E., Kammrath, A., Cheshnovsky, O. & Neumark, D. M. Observation of large water-cluster anions with surface-bound excess electrons. *Science* **307**, 93–96 (2005).

190. Kim, J., Becker, I., Cheshnovsky, O. & Johnson, M. A. Photoelectron spectroscopy of the 'missing' hydrated electron clusters (H2O)-n , n=3, 5, 8 and 9: Isomers and continuity with the dominant clusters n=6, 7 and ≥11. *Chem. Phys. Lett.* **297**, 90–96 (1998).

191. Williams, C. F. & Herbert, J. M. Influence of structure on electron correlation effects and electron-water dispersion interactions in anionic water clusters. *J. Phys. Chem. A* **112**, 6171–6178 (2008).

192. Coons, M. P., You, Z. Q. & Herbert, J. M. The Hydrated Electron at the Surface of Neat Liquid Water Appears to Be Indistinguishable from the Bulk Species. *J. Am. Chem. Soc.* **138**, 10879–10886 (2016).

193. Turi, L. Hydrated electrons in water clusters: Inside or outside, cavity or noncavity? *J. Chem. Theory Comput.* **11**, 1745–1755 (2015).

194. Casey, J. R., Schwartz, B. J. & Glover, W. J. Free Energies of Cavity and Noncavity Hydrated Electrons Near the Instantaneous Air/Water Interface. *J. Phys. Chem. Lett.* **7**, 3192–3198 (2016).

195. Wang, C. R., Nguyen, J. & Lu, Q. Bin. Bond breaks of nucleotides by dissociative electron transfer of nonequilibrium prehydrated electrons: A new molecular mechanism for reductive DNA damage. *J. Am. Chem. Soc.* **131**, 11320–11322 (2009).

196. Boudaïffa, B., Cloutier, P., Hunting, D., Huels, M. A. & Sanche, L. Resonant formation of DNA strand breaks by low-energy (3 to 20 eV) electrons. *Science* **287**, 1658–1660 (2000).

197. Barrios, R., Skurski, P. & Simons, J. Mechanism for damage to DNA by low-energy electrons. *J. Phys. Chem. B* **106**, 7991–7994 (2002).

198. Bogdanov, A. M. *et al.* Green fluorescent proteins are light-induced electron donors. *Nat. Chem. Biol.* **5**, 459–461 (2009).

199. Wen, Y. C. *et al.* Unveiling Microscopic Structures of Charged Water Interfaces by

Surface-Specific Vibrational Spectroscopy. *Phys. Rev. Lett.* **116**, (2016).

200. Jungwirth, P. & Tobias, D. J. Ions at the air/water interface. *J. Phys. Chem. B* **106**, 6361–6373 (2002).

201. Wu, W. *et al.* Understanding the Different Steps of Surfactant Adsorption at the Oil-Water Interface with Second Harmonic Generation. *J. Phys. Chem. C* **120**, 6515–6523 (2016).

202. Hosseinpour, S., Götz, V. & Peukert, W. Effect of Surfactants on the Molecular Structure of the Buried Oil/Water Interface. *Angew. Chemie - Int. Ed.* **60**, 25143–25150 (2021).

203. Zhang, C. *et al.* Corn Oil-Water Separation: Interactions of Proteins and Surfactants at Corn Oil/Water Interfaces. *Langmuir* **36**, 4044–4054 (2020).

204. Guo, W., Lu, T., Gandhi, Z. & Chen, Z. Probing Orientations and Conformations of Peptides and Proteins at Buried Interfaces. *J. Phys. Chem. Lett.* **12**, 10144–10155 (2021).

205. Rao, Y., Xu, M., Jockusch, S., Turro, N. J. & Eisenthal, K. B. Dynamics of excited state electron transfer at a liquid interface using time-resolved sum frequency generation. *Chem. Phys. Lett.* **544**, 1–6 (2012).

206. Meyer, M. & Mialocq, J. C. Ground state and singlet excited state of laser dye DCM: Dipole moments and solvent induced spectral shifts. *Opt. Commun.* **64**, 264–268 (1987).

207. Meyer, M., Mialocq, J. C. & Perly, B. Photoinduced intramolecular charge transfer and trans-cis isomerization of the DCM styrene dye. Picosecond and nanosecond laser spectroscopy, high-performance liquid chromatography, and nuclear magnetic resonance studies. *J. Phys. Chem.* **94**, 98–104 (1990).

208. Szyszkowski, B. von. Experimentelle Studien über kapillare Eigenschaften der wässerigen Lösungen von Fettsäuren. *Zeitschrift für Phys. Chemie* **64U**, 385–414 (1908).

209. Prosser, A. J. & Franses, E. I. Adsorption and surface tension of ionic surfactants at the air-water interface: Review and evaluation of equilibrium models. *Colloids Surfaces A Physicochem. Eng. Asp.* **178**, 1–40 (2001).

210. Wang, C. & Morgner, H. The dependence of surface tension on surface properties of ionic surfactant solution and the effects of counter-ions therein. *Phys. Chem. Chem.*

Phys. **16**, 23386–23393 (2014).

Appendix A: LabVIEW Code

Data acquisition was handled using LabVIEW 2017, which was used to interface with the TA or SFG detectors and control the pump-probe delay stage (TS1 in Figure 3.1 and Figure 3.8) during measurements and setup. Both experiments used similar code, which was structured as in Figure A.1.

The LabVIEW programs take input variables specifying the file paths for saving data, and the number of data point averages, N_1 to acquire data over. The number of laser shots per TA data point is specified by the camera image size, which is fixed at 4092 lines per image, whilst the number of laser shots per data point for the SFG is specified by a counting time, given in seconds. The SFG acquisition simply counts the number of photons received in that period for each of the pump-on and pump-off channels.

Both programs are specified the location of t_0 on the translation stage for that configuration as a distance with which to reference to. The time values are specified by a text file containing a list of the values in femtoseconds, which are converted to relative distances by a conversion constant. The LabVIEW runs the time files front-to back, and then back-to-front and averages the corresponding time points to reduce possible effects of sample degradation on the signals recorded. The TA also takes additional parameters in the form of the pixel index of the chopper flag and an associated intensity threshold, which allow the first line of an image to be assigned as pump-on or pump-off.

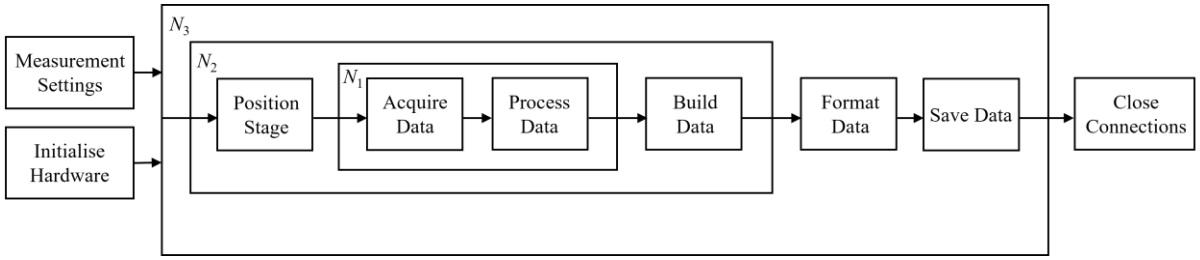

Figure A.1: Flow diagram representing LabVIEW code used to run TA or SFG measurements. N_1 is the data averaging parameter, N_2 is the timestep and N_3 is the scan number.

When an image is acquired, the program checks the intensity of the first line at the pixel index, and if it is greater than the threshold, the flag has arrived at the camera and the line is a pump-off spectrum, for example. All the other lines are therefore assigned as a result of the shot-to-shot chopping.

When run, the program first initialises the hardware to be used. Both initialise the translation stage in the same way, whilst the TA experiment connects to the camera or the SFG loads a stored task on the data acquisition box. After initialisation, the stage reads the first pump-probe time delay and moves the stage to the correct position relative to the t_0 value specified. The stage checks its position and repeats until it is 'on target' at the correct position. Typical errors in the final stage position correspond to ± 50 fs or less. Next, the data acquisition occurs by either grabbing a frame from the camera or starting the photon counting interval, waiting the assigned time, stopping the count and then reading the count number. The raw data is then processed in the case of TA to give a difference absorption spectrum. For SFG, the raw photon count is used. For the data collected, these processes are performed a total of N_1 times, and the averaged data for that time point is carried forward.

This process represents the data of one timestep, which is repeated for the number of timesteps in the range, N_2. Each averaged data point is compiled into a two-dimensional array with its timestep value appended to the beginning of each entry for post-processing analysis. The array of data is collectively formatted and saved to the path specified initially. The program repeats the above process N_3 times, saved separately as a new scan for each iteration. Finally, after the desired scan number has been reached, connections to the stage and acquisition devices are properly closed to prevent errors on their next call.

Appendix B: Derivation of Surface Kinetic Model

The equation (5.6) was derived using the mechanistic scheme for the surface processes presented in Figure 5.13, of the form:

$$\begin{array}{ccccc} A & \xrightarrow{k_d} & B & \xrightarrow{k_b} & D \\ \downarrow k_n & & & & \\ C & & & & \end{array} \qquad \text{(B.1)}$$

Where A is the electron:radical contact pair population, B is the free surface electron population, C is the phenolate anion population, and D is the hydrated bulk electron population. The rate constants are as described in chapter 5. The SFG signal should probe both the electron in the contact pair and after its dissociation, so the total surface SFG signal is

$$N_{e,S}(t) = A + B \, . \qquad \text{(B.2)}$$

The relevant differential equations are:

$$\frac{dA}{dt} = -(k_n + k_d)A \qquad \text{(B.3)}$$

and

$$\frac{dB}{dt} = k_d A - k_b B \, . \qquad \text{(B.4)}$$

Equation (B.3) is trivially solved to give first order rate kinetics:

$$A = e^{-(k_n + k_d)t} \, . \qquad \text{(B.5)}$$

Equation (B.4) can be solved by simple rearrangement followed by multiplication of the integrating factor $e^{k_b t}$:

$$\frac{dB}{dt} e^{k_b t} + k_b e^{k_b t} B = k_d A e^{k_b t} = k_d e^{[k_b - (k_n + k_d)]t} . \quad \text{(B.6)}$$

The left-hand pair of terms can be recognised as the differential of $Be^{k_b t}$ by the product rule, and the second equality is shown by substitution of (B.5). Both sides can be integrated between t and 0 to obtain

$$Be^{k_b t} = \frac{k_d}{k_b - (k_n + k_d)} \left[e^{[k_b - (k_n + k_d)]t} - 1 \right] . \quad \text{(B.7)}$$

Note the appearance of –1 in the right-hand term, which is obtained as the constant of integration by considering that at time $t = 0$, none of the contact pairs have dissociated, so the initial population of B must be zero. Finally, dividing by the integrating factor yields the time-dependent concentration of B:

$$B = \frac{k_d}{k_b - (k_n + k_d)} \left[e^{-(k_n + k_d)t} - e^{-k_b t} \right] . \quad \text{(B.8)}$$

The total SFG signal is thus

$$N_{e,S}(t) = \frac{k_d}{k_b - (k_d + k_n)} \left[e^{-(k_d + k_n)t} - e^{-k_b t} \right] + e^{-(k_d + k_n)t} , \quad \text{(B.9)}$$

which appears to fit the observed surface kinetics well.

Appendix C: Surface Tensiometry Analysis

Surface tension measurements of phenol and phenolate solutions were taken using a pendant drop-shape surface tensiometry setup, which used computer software to analyse images taken of hanging drops and calculate their associated surface tension values. The raw data yielded a curve of surface tension, γ, versus concentration, c. The pH was controlled by diluting a stock solution with sodium hydroxide solution of the appropriate pH, rather than water, in the case of phenolate. Initial measurements that diluted with water had caused the pH to tend towards 7 at low solute concentrations, causing the recorded data to match that of phenol.

The surface tension was described by the fitting the Szyskowski equation to the data:[208,209]

$$\gamma = \gamma_0 - nRT\Gamma_\infty \ln(1 + Kc) \,, \tag{C.1}$$

where γ_0 is the surface tension of the neat solvent, R is the universal gas constant, T is temperature, Γ_∞ is the maximal surface concentration and K is the surface-bulk equilibrium constant. The dissociation constant, n, is 2 for phenolate, which dissociated into two components in solution and acts as an ionic surfactant.

The surface excess is then found through the surface tension isotherm by[210]

$$\Gamma = \frac{-1}{nRT} \cdot \frac{d\gamma}{d \ln c} \,, \tag{C.2}$$

where Γ is the surface excess, and the derivative was determined numerically. The resulting graph of surface excess could be expressed as a percentage of Γ_∞ to obtain the relative surface coverage quoted in this thesis, and the absolute values obtained were in good agreement with previous studies.[159]